TAMPEREEN TEKNILLINEN YLIOPISTO
TAMPERE UNIVERSITY OF TECHNOLOGY

RIKU ISOAHO

SPECTRAL AND TEMPERATURE DYNAMICS OF HIGH-EFFICIENCY DILUTE NITRIDE MULTIJUNCTION SOLAR CELLS

Master of Science Thesis

Examiners: Prof. Mircea Guina and PhD Antti Tukiainen
The examiners and topic of the thesis were approved by the Council of the Faculty of Natural Sciences on 3rd February 2016

ABSTRACT

TAMPERE UNIVERSITY OF TECHNOLOGY
Master's Degree Programme in Science and Engineering
ISOAHO, RIKU: Spectral and temperature dynamics of high-efficiency dilute nitride multijunction solar cells
Master of Science Thesis, 92 pages
September 2016
Major: Advanced Engineering Physics
Examiners: Professor Mircea Guina and PhD Antti Tukiainen
Keywords: III–V semiconductors, molecular beam epitaxy, dilute nitride, multijunction solar cell, high-efficiency, temperature coefficient, solar spectrum

Multijunctional solar cell architecture, combined with novel materials, provides a pathway for reaching ultra-high conversion efficiencies in terrestrial and space applications of photovoltaics. The operating conditions significantly affect the performance of cells, and a deep understanding of the operation dynamics is essential when developing multijunction cells in pursuit of efficient energy production. In this study, the influence of illumination spectra and temperature on the operation of triple-junction III–V solar cells, which employ dilute nitride subcells and are grown by plasma-assisted molecular beam epitaxy, are presented. The main emphasis was on current-voltage characterization performed at various spectral and temperature conditions. For these experiments a new solar simulator system with multiple light sources was built, for which a temporal stability of ± 2 % was measured. The simulator proved to be an accurate and useful tool for solar cell characterization. Additional performance evaluation for the best multijunction cell was made based on external quantum efficiency measurements.

At 25℃ the best triple-junction cell demonstrated conversion efficiencies of 27 % and 28 % with extraterrestrial and terrestrial spectra, respectively. The dilute nitride subcells were determined to overgenerate current, and the cells were analyzed to be current-limited by the GaInP top junctions. The temperature behavior of the cells was studied by temperature dependent measurement. The current generation of the cells increased whereas the conversion efficiencies decreased with temperature. Temperature coefficients for the performance parameters were extracted from the measured data. The temperature coefficients were found to be in good agreement with coefficient values reported in literature.

TIIVISTELMÄ

TAMPEREEN TEKNILLINEN YLIOPISTO
Teknis-luonnontieteellinen koulutusohjelma
ISOAHO, RIKU: Laimeiden typpeä sisältävien korkean hyötysuhteen moniliitosaurinkokennojen spektri- ja lämpötiladynamiikka
Diplomityö, 92 sivua
Syyskuu 2016
Pääaine: Teknillinen fysiikka
Tarkastajat: Prof. Mircea Guina ja TkT Antti Tukiainen
Avainsanat: III–V-puolijohteet, molekyylisuihkuepitaksia, laimeat typpiyhdisteet, moniliitosaurinkokenno, korkea hyötysuhde, lämpötilavakio, Auringon spektri

Moniliitosaurinkokennojen ja uusien materiaaliratkaisujen avulla on mahdollista saavuttaa erittäin korkeita hyötysuhteita aurinkokennojen eri sovelluksissa. Käyttöolosuhteilla on merkittävä vaikutus kennojen toimintaan, minkä vuoksi kennojen toiminnan syvällinen ymmärtäminen on tärkeää kehitettäessä moniliitoskennoja, joilla pyritään entistä tehokkaampaan energiantuotantoon. Tässä työssä tutkittiin valaisun ja lämpötilan vaikutusta III–V-puolijohteista valmistettujen kolmiliitoskennojen toimintaan. Tutkitut kennot valmistettiin plasma-avusteisella molekyylisuihkuepitaksialla. Kennojen rakenteessa on käytetty osakennoja, jotka sisältävät pienen määrän typpeä. Kennot karakterisoitiin erilaisissa olosuhteissa virta-jännitemittauksin, joita varten rakennettiin kolmesta valonlähteestä koostuva aurinkosimulaattori. Simulaattori osoittautui tarkaksi ja hyödylliseksi työkaluksi kennojen karakterisoinnissa, ja sen tuottaman valotehon ajalliseksi stabiiliudeksi määritettiin ± 2 %. Virta-jännitemittausten lisäksi parhaan moniliitoskennon toimintaa tutkittiin ulkoisen kvanttihyötysuhteen avulla.

Huoneenlämmössä parhaan kolmiliitoskennon hyötysuhteeksi mitattiin 27 % AM0-spektrillä ja 28 % AM1.5-spektrillä. Typpeä sisältävät osakennot ylituottivat virtaa kaikissa kolmiliitoskennoissa, kun taas GaInP-liitoksen havaittiin rajoittavan kennojen virtaa. Kennojen toimintaa tutkittiin myös lämpötilariippuvilla mittauksilla. Kennojen virrantuotto kasvoi ja hyötysuhde laski lämpötilan noustessa. Lämpötilariippuvista mittauksista määritettiin myös lämpötilavakiot kennojen toimintaa kuvaaville suureille. Lämpötilavakioiden arvot ovat yhteneviä kirjallisuudessa esitettyjen vakioiden kanssa.

PREFACE

This thesis was carried out at the Optoelectronics Research Centre (ORC) of Tampere University of Technology with funding from the European Space Agency and the European Union. I would like to thank the director of ORC, Dr. Pekka Savolainen, for the chance to work at ORC for these past two years.

I would like to express my gratitude for the examiners of my thesis, Prof. Mircea Guina and Dr. Antti Tukiainen, for their support and guidance. A special thanks to Antti for giving me the initial chance with my BSc thesis, and for introducing me to the wonderful world of semiconductors.

A special thank you goes to the past and present members of the GEN20 team: Dr. Arto Aho, Dr. Ville-Markus Korpijärvi, and Pekka Malinen. I thank Arto for being the instructor for my thesis, for mentoring me with MBE and solar cells, and for the thrilling experiments with the GEN20. I thank Ville for teaching me the ropes of lasers and MBE. I thank Pekka for the tutoring when I started at ORC.

I would like to gratefully acknowledge also the members of the solar cell processing team: Dr. Ville Polojärvi, Marianna Raappana, Timo Aho, and Lauri Hytönen. It has truly been inspiring and fun to work with you. Thanks to Eero Koivusalo and my officemate Antti Aho for the important peer support. I would like to express my sincere gratitude for the entire staff of ORC for all the help over the past couple of years, and for making ORC such a pleasant place to work.

Finally, I am deep gratitude to my family and friends for their unlimited support over the years. A special thank you needs to go to Hanna for always being there for me, and for tolerating the long days (and sometimes nights) at the office.

Tampere, August 23rd, 2016

Riku Isoaho

CONTENTS

LIST OF ABBREVIATIONS AND SYMBOLS

AM	airmass
ARC	anti-reflection coating
BAC	band anti-crossing model
BEP	beam equivalent pressure
BSF	back surface field
CB	conduction band
CPV	concentrated photovoltaics
DBR	distributed Bragg reflector
EHP	electron–hole pair
EQE	external quantum efficiency
fcc	face-centered cubic
FF	fill factor
IQE	internal quantum efficiency
IR	infrared
IV	current-voltage
LIV	light biased current-voltage
LP	longpass
MBE	molecular beam epitaxy
MJSC	multijunction solar cell
MOCVD	metal-organic chemical vapor deposition
ORC	Optoelectronics Research Centre
PAMBE	plasma-assisted molecular beam epitaxy
PBN	pyrolytic boron nitride
PV	photovoltaics
RF	radio frequency
RHEED	reflection high-energy electron diffraction
SC	solar cell
SDL	semiconductor disk laser
SP	shortpass
SRO	short range ordering
SSMBE	solid source molecular beam epitaxy
TC	temperature coefficient
TJ	tunnel junction

UHV	ultra-high vacuum
UV	ultraviolet
XRD	x-ray diffraction
2J	dual-junction solar cell
3J	triple-junction solar cell

α	material dependent parameter used in Varshni relation
β	material dependent parameter used in Varshni relation
η	conversion efficiency
λ	photon wavelength
ν	photon frequency

a	lattice constant
a_f	lattice constant of epilayer
a_s	lattice constant of substrate
A_{sc}	area of solar cell
$A_{sc,active}$	active area of solar cell
c	speed of light in vacuum
C	bowing parameter for calculating band gap values
E	energy
E_C	energy of conduction band
E_F	energy of Fermi level
E_g	band gap energy
$E_{g,0}$	band gap energy at 0 K
E_M	energy of host material
E_N	energy level created by nitrogen
E_{ph}	photon energy
E_V	energy of valence band
$E_\pm$	conduction subbands created by nitrogen
F	spectral irradiance
h	Planck constant
i	subcell index
I	current
I_L	photocurrent
I_{MJ}	current of multijunction solar cell
I_{mp}	current at maximum power point

I_{sc}	short-circuit current
J_{sc}	short-circuit current density
I_0	dark saturation current
$\mathbf{k}$	wave vector
k_B	Boltzmann constant
n	ideality factor
N_e	number of generated electrons
$N_{ph,inc}$	number of incident photons
P	power
P_{mp}	power at maximum power point
q	elementary charge
R	reflectance
R_s	series resistance
R_{sh}	shunt resistance
S	spectral responsivity
S_{ref}	spectral responsivity of reference detector
T	temperature, or transmittivity
T_g	growth temperature
U	voltage signal of solar cell
U_{ref}	voltage signal of reference detector
V	hybridization energy of nitrogen and conduction band, or voltage
V_{MJ}	voltage of multijunction solar cell
V_{mp}	voltage at maximum power point
V_{oc}	open-circuit voltage
X	concentration factor

1. INTRODUCTION

People throughout the ages have been fascinated by the Sun and have dreamed of harnessing it's immense power. The first steps towards harvesting power from sunlight were taken in 1839 when a French physicist, Edmond Becquerel, first demonstrated the photoelectric effect [14, 39]. After the demonstration of the first practical silicon solar cell (SC) with 6 % conversion efficiency in 1954 [19], the photovoltaics (PV) have been considered as a promising candidate for production of sustainable energy. In 2015, the globally installed PV capacity was 177 GW which covered 1 % of the energy generation of the whole world [51]. In 2014 over 90 % of the built PV capacity was based on silicon technologies [34]. But as the worlds energy consumption keeps growing when countries develop [108], and the need for renewable energy is greater than ever, researchers are trying to make photovoltaics economically more viable by increasing the conversion efficiencies and lowering the material costs of solar cells. Over the years several competing PV technologies have emerged, including multijunction, thin-film, organic, and perovskite SCs [40] (see figure 1.1).

Multijunction solar cells (MJSC) are widely considered as the most promising PV technology since they possess potential for reaching ultra-high conversion efficiencies, i.e. more than 50 %. In multijunction approach the solar spectrum is split between multiple subcells that each convert different parts of the solar spectrum into electricity according to the material properties and cell design. Besides offering a possibility to employ materials covering a broader spectral range, the spectral splitting reduces thermalization losses, which results in a higher overall conversion efficiency.

III–V semiconductor compounds are an attractive choice for MJSC applications since they offer a wide range of band gap energies can be obtained while remaining lattice-matched to gallium arsenide (GaAs) and germanium (Ge). Still, the spectral region corresponding to 1 eV energies has been problematic as lattice matching cannot

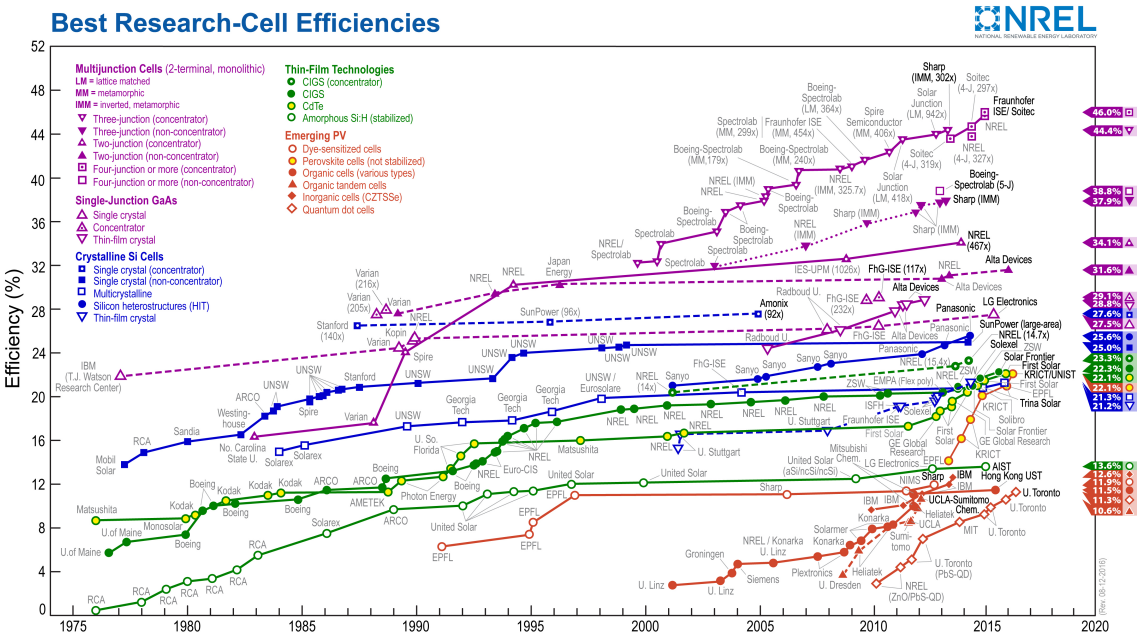

Figure 1.1. *Best research solar cell efficiencies [77].*

be fulfilled using standard GaAs-based materials, i.e. InGaAs. Recently, novel III–V compounds containing dilute concentrations of nitrogen (N) and antimony (Sb), such as GaInNAs and GaInNAsSb, have become of great interest since band gap energies under 1 eV that can be reached with these materials [53]. These dilute nitride compounds are proposed as a replacement to Ge-junction or as an intermediate subcell between GaAs and Ge in the current state-of-the-art MJSC devices [3]. Several demonstrations of MJSC employing dilute nitride subcells have already been made [5, 90].

The III–V MJSCs are an excellent choice for terrestrial use in concentrated photovoltaics (CPV) systems and for space applications. In CPV technology the sunlight is concentrated from large area to a small cell. And since smaller solar cells are needed, the CPV approach can significantly reduce the material costs. In addition, the conversion efficiencies of III–V cells can be significantly increased up to concentration levels of several hundreds of suns. This further increases the feasibility of III–V CPV systems, which possess real potential in reaching ultra-high conversion efficiencies. In fact, the current world record in conversion efficiency, 46 %, was demonstrated with a III–V MJSC under concentration [33, 40]. The good radiation hardness and high power-to-mass-ratio make III–V cells ideal

for space applications where these attributes are of great value [13]. Currently, III–V-based triple-junction solar cells are widely used to power up satellites [31].

When designing and fabricating MJSC devices, one needs take into account the operating conditions. Firstly, the solar spectrum is not constant as it is affected by the atmosphere. In space, at the top of the atmosphere, the solar intensity is higher than on the surface of the Earth. The attenuation of the solar intensity is caused by the atmospheric gases, which scatter and absorb certain parts of solar spectrum very effectively. This creates challenges in designing MJSC devices since the spectrum needs to be split appropriately between the subcells. Ideally, for highest possible efficiencies, the junctions of the MJSC should be tailored according to the atmospheric conditions of the planned geographical location. Other major issue that needs to be taken in account in SC design is the effect of temperature. In space applications, the SCs can experience extreme temperature variations. In the geosynchronous orbit cell temperature can vary between -160℃ and 100℃ [67], and in terrestrial concentrator applications the cell temperatures can rise significantly above ambient temperatures [95, 114]. The temperature influences the solar cell performance and, therefore, it's vital to know the temperature behavior of the cells. The temperature coefficients for band gaps and current–voltage-properties of conventional materials like GaInP, GaAs and Ge are well known [1, 35, 66, 97] but for the dilute nitride materials the published studies are sparse.

In this thesis, the influence of temperature and spectrum on the performance of triple-junction (3J) GaInP/GaAs/GaInNAsSb SCs, grown with plasma-assisted molecular beam epitaxy (PAMBE), are studied. The performance of the cells is evaluated under AM0 and AM1.5D spectra which are standards for space and CPV applications, respectively. For the characterization a three-band solar simulator setup was built. The built setup offers variable operating temperatures, and enables better testing of current-matching between subcells of MJSCs. In addition to characterization of the SCs, the heteroepitaxy of SC structures with PAMBE is discussed.

This thesis consists of seven chapters. In chapter 2, the properties of III–V semiconductor materials are reviewed, with a focus on the properties of dilute nitride compounds. Chapter 3 focuses on the physical operation principles and structures of semiconductor solar cells. The fabrication of III–V SC structures is

addressed in chapter 4. After this, in chapter 5, the multijunction solar cell samples used for this thesis are introduced along with the methods used for the characterization of the samples. In chapter 6, the results are presented and the observations are analyzed. The thesis is concluded in chapter 7, where the results of the thesis are summarized.

2. III–V SEMICONDUCTORS

Semiconductor materials form the basis to our modern day information society, as components made out of semiconductors are used in almost all electronic devices. Semiconductors conduct electricity better than insulators, like glass, but have lower conductivity than conductors, like metals, but what truly makes them ideal for electronics is that their conductivity can be altered. Semiconductors, especially direct band gap semiconductors, interact strongly with light, absorbing and emitting photons. The combination of the optical and electrical properties makes semiconductors attractive for optoelectronic applications.

Semiconducting materials are divided into elemental, compound, and organic semiconductors. The typical elemental semiconductors, silicon and germanium, are found in main group–IV of the periodic table. Si is the most widely used semiconductor material, and modern integrated circuits are almost entirely based on silicon technology [119]. Some organic molecules also demonstrate semiconducting behavior, and they are gaining popularity in display technologies [57] and flexible solar cells [54]. Compound semiconductors, on the other hand, are composed of two or more elements, and they are categorized according to their constituent atoms. The most common types of compound semiconductors are III–V, II–VI, and IV–IV materials [103].

In this thesis the main focus is on III–V semiconductors that are formed between group–III and group–V atoms. The simplest III–V compounds are binaries, like gallium arsenide (GaAs) and indium phosphide (InP), which comprise equal amounts of atoms from both groups. By increasing the number of elements, more complex compounds can be formed. The main advantage of compound semiconductors is their versatility as their properties can be modified with their atomic compositions. In addition, by layering different semiconductors materials heterostructures can be fabricated that can be used for manipulating the optical and electrical properties of semiconductor components.

This chapter discusses the properties of III–V semiconductors and heterostructures. In the first section, the properties of conventional III–V compounds are introduced. In the second section a novel material system, called dilute nitrides, is reviewed. The last section discusses heterostructures made from III–V compounds.

2.1 Properties of conventional III–V materials

III–V semiconductors are generally periodic crystalline solids. The periodic structure gives rise to the energy band structure that is dependent on the material composition. The characteristic band structure, on the other hand, largely dictates the optical and electrical properties the material. In this section the physical properties of conventional III–V compounds are introduced.

2.1.1 Crystal structure

Solid materials can be classified into groups of crystalline, polycrystalline, and amorphous solids according to their atomic arrangements. In crystalline solids a periodic atomic structure is ideally repeated throughout the entire solid. Each ordered crystalline structure can be represented with a lattice and a basis. Lattice is an ordered collection of identical points in space and basis is the simplest arrangement of atoms related to every lattice point. Typically, the III–V semiconductors crystallize in a cubic zincblende structure. Zincblende is formed in a face-centered cubic (fcc) lattice with a basis comprising atoms of two or more elements. Atoms from group–III form bonds with four neighboring group–V atoms (and vice versa). The cubic nature of the zincblende structure allows it to be characterized with single lattice constant, a [113]. The zincblende crystal structure is illutrated in figure 2.1.

Some of the III–V materials, like many nitrides, usually crystallize in a hexagonal wurtzite structure but under the right conditions metastable zincblende can also be observed [88]. Like in zincblende lattice, the group–III atoms surrounded by four neighboring group–V atoms in wurtzite structure. The hexagonal wurtzite unit cell is characterized by two lattice constants. [113]

The bond lengths between the atoms are dependent on the constituent atoms in the structure which causes the lattice constants to be material and composition

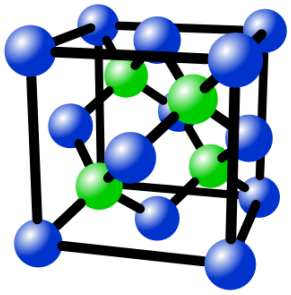

Figure 2.1. *Unit cell of a zincblende crystal structure.*

dependent. The bonds are also affected by temperature as the bond lengths dilate with increasing temperature which results in expansion of the lattice constant. [73] One of the great properties of III–V semiconductors is the ability to tune the lattice constant in a wide range by altering the material compositions. The lattice constants of simple III–V binaries can be used for approximating lattice constants of more complex III–V compounds by using empirical Vegard's law [110]. According to the Vegard's law, the lattice constant of alloys can be approximated with composition-weighted average of the lattice constants of the constituent binaries. For example, the lattice constant of ternary GaInAs can be estimated from

$$a_{Ga_{1-x}In_xAs} = (1-x)a_{GaAs} + xa_{InAs}, \tag{2.1}$$

where x corresponds to the fraction of In from group–III atoms, and a_{GaAs} and a_{InAs} are the lattice constants of GaAs and InAs, respectively [110]. Expressions for other alloys can be constructed in similar manner [42].

2.1.2 Band structure and band gap

Electrons in isolated atoms occupy atomic orbitals which forms discrete energy states, but as a large number of atoms is brought together to form a solid, the atomic orbitals of individual atoms combine to form molecular orbitals. In a solid, the energy states formed by the atomic orbitals are so close to each other that, instead of discrete energy levels, the energies can be considered to form continuous energy bands. Electrons tend to occupy the energy levels from the lowest energies towards higher energies. The highest occupied levels at 0 K form the, so-called,

valence band (VB), while the lowest unoccupied levels at 0 K form the conduction band (CB). The highest energy of the VB, and the lowest energy of the CB are denoted with E_V and E_C, respectively. Some energy ranges may not be covered by the energy bands, therefore, a forbidden range of energies, called the band gap, is formed between the bands. The energy of the band gap is denoted with E_g, and it corresponds to the energy difference between VB and CB. [103]

The band structure is characteristic for every solid material, and many electrical and optical properties can be explained through it. The band structure of materials is, essentially, a graph showing the allowed and forbidden electron energies (E) at each electron wave vector ($\mathbf{k}$). The band structure of a material can be obtained by solving the Schrödinger equation for electrons in the periodic potential of the crystal [41]. Exemplary band diagrams of Si and GaAs are depicted in figure 2.2.

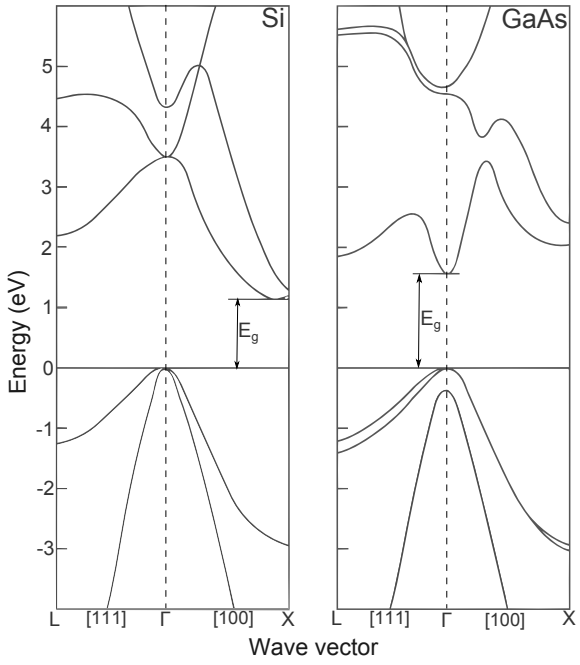

Figure 2.2. *Band structures of Si and GaAs [103, modified]. In the band diagrams E_V is chosen to correspond to zero energy.*

In both band diagrams illustrated in figure 2.2, the VB maximum is located at $\mathbf{k}$=0. From the 2.2 we can also notice that for GaAs, the CB minimum E_C occurs also at $\mathbf{k}$=0, therefore, it is said to have a direct band gap. Several III–V semiconductors are direct band gap materials [113]. In the case of Si we notice that E_V and E_C occur with different values of $\mathbf{k}$, and materials like Si are said to have an indirect

band gap. Also, additional bands that are formed besides the main valence and conduction bands can be observed. For GaAs we can see three separate VBs with minima at **k**=0, close to the band gap. These energy bands, from highest energy towards lowest, are termed heavy-hole, light-hole and spin-orbit split-off bands [41]. We also note that the curvatures of the bands are nonidentical, but near **k**=0, the VB and CB can be approximated with parabolic functions [73].

From the engineering-point-of-view the band gap is probably the most important property of the semiconductor materials, as many electrical and optical properties are linked to it. The band structures and, thereby the band gaps, of compound semiconductors can be modified by altering the material composition, inducing strain, adding impurities, applying electric fields, or changing the temperature. Beside the wide tunability of lattice constants, the III–V semiconductors also offer a broad range of band gap tunability. The working space of III–V compounds, in terms of band gap energies and lattice constants, is illustrated in figure 2.3.

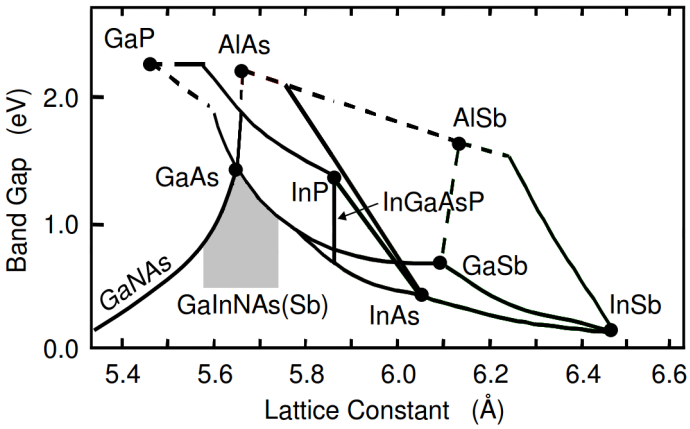

Figure 2.3. *Band gap energies and lattice constants for many III–V compounds [69, modified]. The grey region illustrates the working space of GaInNAs(Sb) on GaAs.*

The band gap energies of III–V semiconductors can be approximated with an interpolation scheme, similarly as the lattice constants were approximated with equation 2.1. Unlike with the lattice constants, the linear approximation is insufficient for the E_g, as they do not vary linearly with material composition. For this an additional parameter, called the bowing factor, is needed. For example, the E_g of GaInAs can be evaluated from equation

$$E_{g,Ga_{1-x}In_xAs} = (1-x)E_{g,GaAs} + xE_{g,InAs} - x(1-x)C_{GaInAs}, \tag{2.2}$$

where C is the bowing parameter of the ternary alloy in question. Expressions for other compounds can be constructed in similarly. It should be noted that for some ternaries (eg. AlGaAs and AlGaSb) the bowing parameters are composition dependent and, therefore, the interpolation scheme should be used with care. [113] More sophisticated models are required for approximating the band gap energies of more complex materials, for example dilute nitrides (see section 2.2).

The E_g has also a temperature dependence. The thermal expansion of the crystal lattice induces changes in the band structure, decreasing the E_g. The temperature dependence of E_g is often expressed with so called Varshni relation

$$E_g(T) = E_{g,0} - \frac{\alpha T^2}{T+\beta}, \tag{2.3}$$

where $E_{g,0}$ is the band gap energy at 0 K, T is the temperature, and α and β are material dependent parameters [109]. However, the theoretical basis of the Varshni relation is rather weak, since the parameter β is supposed to be related to Debye temperature, but in some cases it can have negative values [78]. Despite the empirical nature of the Varshni relation, it is commonly used in literature, and constants α and β are widely reported [1, 113].

Electrical properties

The electrical conductivity of materials is closely related to the magnitude of the band gap. In metals, the VB and CB overlap, meaning that no band gap is observed which, on the other hand, translates into high electrical conductivity for metals. Contrary to metals, insulators possess very large band gaps (4–12 eV), while semiconductors have E_g values ranging between conductors and insulators (0–4 eV). [104] The electrical current in semiconductors is carried by two charge carriers, electrons and holes. In the VB and CB the current is intermediated by

electrons and holes, respectively. The holes are empty energy states in the VB that are left by excited electrons. It is mathematically convenient to represent the holes as positive charges moving in opposite direction compared to the electrons. Both carriers move to seek the most energetically favorable positions in their corresponding bands. Electrons tend to fall to the lower energies, but the holes instead rise to the highest energy states in the VB.

In thermal equilibrium, the charge carriers obey Fermi–Dirac distribution which, essentially, tells the probability of an electron to occupy a state with an energy E at given temperature. The Fermi energy, E_F, describes the energy level, where the probability of finding an electron (or a hole) is exactly half, if all energy ranges were allowed. The E_F is independent of temperature. In pure, intrinsic, semiconductors at E_F is situated in the middle of the band gap. At 0 K all available energy levels are filled up to Fermi-level, but as temperature increases, the average thermal energy of electrons rises causing a fraction of the electrons to have enough energy to occupy higher energy levels above E_F.

The electrical properties of semiconductors can be modified by introducing impurity atoms (dopants) to the crystal, thus, making the material extrinsic. The dopants effectively introduce allowed energy states in the band gap, near the energy band corresponding to the type of dopant. Donors create occupied energy states near the CB, while acceptors form unoccupied energy states near the edge of VB. Donors have an extra electron that is loosely bound that is easily excited to CB by thermal energy. The excited electrons then participate to the conduction process and, therefore, donor impurities are called n-type dopants. Accordingly, acceptors create an electron deficit in the lattice, and electrons are easily excited from the VB to the impurity state, thus, leaving behind a hole in the VB. The holes in the VB also contribute to the conduction, thus, the acceptors are called p-type dopants. The energy differences between the main bands and the impurity states are usually so small that even in room temperature practically every impurity atom is thermally ionized. The effective carrier concentrations are modified by altering the amount of dopant atoms in the crystal. The introduction of dopants also shifts the Fermi-level of the material; the Fermi-level is shifted approximately to the middle between the main band and the impurity state.

The doping of III–V crystals depends on the lattice site of the dopant atoms in the crystal. Elements with two outer electrons, like Be, act as p-type dopants when

occupying group–III lattice sites, and elements with six outer electrons, like Te, in group–V lattice sites act as n-type dopants. Group–IV elements (e.g. Si and Ge), on the other hand, are amphoteric dopants and they can act as either acceptors or donors depending on the lattice site they occupy [103]. Different dopants are used in different technologies depending on the materials and desired applications. In MBE, the most common dopants are Si (n-type) and Be (p-type) [16].

Optical absorption and emission properties

The band gap of semiconductor also largely dictates it's optical properties. Photons that possess greater or equal energy as the E_g of the material can absorbed by the semiconductor. When a photon is absorbed by the semiconductor, an electron is excited from the VB to the CB, and a hole is left behind in the VB, thus, an electron–hole-pair (EHP) is created. If the incident photons have greater energy than the E_g of the material, the generated carriers are excited into higher energy states in their corresponding bands from where the carriers then rapidly relax to the energy states near the band gap. The excess energy is released as lattice vibrations, phonons. The relaxed EHPs can then recombine through three distinct processes: spontaneous emission, stimulated emission, and non-radiative recombination. In spontaneous emission the carriers recombine, and a photon corresponding to energy E_g is emitted in a random direction. In stimulated emission, an existing photon (with suitable energy) stimulates an EHP, causing the EHP to recombine. In the process, an identical photon as the stimulating photon is emitted in the same direction as the original photon. When the EHPs recombine non-radiatively, no photons are emitted, instead, the energy is usually released as phonons. The non-radiative recombination usually happens via trapping energy states in the band gap (Shockley–Read–Hall recombination), which can be caused by defects or impurities [91,94]. Other type of non-radiative recombination is Auger recombination where the energy of the EHP is not released as phonons, instead, the released energy excites another carrier into higher energy state [105].

Direct band gap materials, including many of the III–V compounds, absorb and emit light more efficiently than materials with indirect band gaps as the emission and absorption processes don't require change in the momentum (i.e. no change in the **k**-vector). Photon absorption and emission in indirect band gap materials requires presence of an appropriate phonon which decreases the probability of the

processes. Thus, compared to direct transitions, the absorption coefficients of indirect transitions are small [38]. As a result, light absorbing structures made out of indirect band gap materials (e.g. silicon solar cells) need to be made relatively thick.

2.2 Dilute nitrides

In a novel GaAs-based III–V material group, referred as dilute nitrides, small concentrations of nitrogen are being incorporated to the crystal [58]. Antimony is often used as an incorporating surfactant in dilute nitride material growths for improving the material quality [123]. Both, N and Sb, have siginificant effects on the material properties, but the fundamental reason for incorporating N and Sb can be found in the reduction of E_g related to these elements. GaInNAs and GaInNAsSb are the main III–V compounds that can reach band gap energies below 1 eV, while remaining lattice-matched to GaAs and Ge (as seen in figure 2.3). The pioneering work on dilute nitrides was done in the 1990's [58, 115] and, nowadays, dilute nitrides are being demonstrated in telecommunication lasers (i.e. emitting at 1300 nm and 1550 nm) [28, 61] and high-efficiency MJSCs [5, 90]. The research on these material remains very active, as the growth of these materials is further refined and novel devices employing dilute nitrides are developed. In this section, properties of dilute nitride compounds are reviewed.

Compared to other group–V elements, N has a small atomic radius and high electronegativity. When N is incorporated into III–V alloy, local distortions are induced to the crystal lattice which modifies the band structure of the material. Most notably, the nitrogen drastically decreases the E_g of the host material. Additionally, N decreases the lattice constant of the host material. Although, there are benefits to be gained from adding nitrogen, N can also drastically degrade the material quality.

Incorporated nitrogen gives rise to discrete energy levels near the CB of the host material [68]. These impurity levels then interact with the CB, modifying the overall band structure. The interaction between localized N energy levels and the CB of host material have successfully been modeled with a so-called band anti-crossing model (BAC). According to the BAC-model, the localized N states hybridize with the CB, resulting in the splitting the CB into two subbands denoted with $E_{\pm}$. The E_{+} and E_{-} bands form above and under the edge of the host CB, respectively, and the

separation between the subbands and E_g gets wider with increasing N concentration. The dispersion relations of the N induced subbands can be written as

$$E_{\pm}(\mathbf{k}) = \frac{1}{2}[(E_M(\mathbf{k}) + E_N) \pm \sqrt{(E_M(\mathbf{k}) - E_N)^2 + 4V^2 y}], \tag{2.4}$$

where $E_M(\mathbf{k})$ is the dispersion of the host material (e.g. GaInAs) CB, E_N is the N band energy, V is the hybridization strength between the N states and the conduction band, and y is the fraction of N in the crystal. [93] The parameters E_N and V should be obtained by fitting the model to experimental data, but for $Ga_{1-x}In_xAs$ relations for linking these parameters to the material composition have been suggested in literature [93]. Unlike to common III–V compounds, the dispersion relations of the new subbands can not be approximated with parabolic functions around $\mathbf{k}$=0.

As the E_- band is formed under the CB of the host material, the electronic transitions with the lowest energy shift to occur between E_C and E_- resulting in reduction of the fundamental E_g. The E_g is reduced very rapidly with increasing N composition. Additionally, the bowing parameter of dilute nitrides is dependent on the nitrogen composition and can not be expressed with single a parameter. For this reason, the interpolation scheme, used for approximating the band gap energies of traditional III–V compounds, works poorly on dilute nitrides. Alternatively, the band gaps of dilute nitrides can be evaluated from equation 2.4 by substituting $E_M(\mathbf{k})$ with the E_g value of the host crystal, and parameters E_N and V with values corresponding to the composition of the dilute nitride alloy [60]. The effect of temperature on E_g in dilute nitrides is not well known, but the temperature dependent properties of dilute nitrides has been investigated by quantum efficiency measurements in our earlier work [52].

As mentioned, N is smaller than other group–V atoms, which causes N to decrease the lattice constant of the host material. This makes the dilute nitride material more tensively strained compared to the host material. Nitrogen incorporation can therefore be used to compensate compressive strain in some material systems (e.g. GaInAs on GaAs). $Ga_{1-x}In_xN_yAs_{1-y}$ can be lattice-matched to GaAs with $x \approx 2.8y$ [60]. In figure 2.4 band gap and lattice parameters of $Ga_{1-x}In_xN_yAs_{1-y}$ are illustrated.

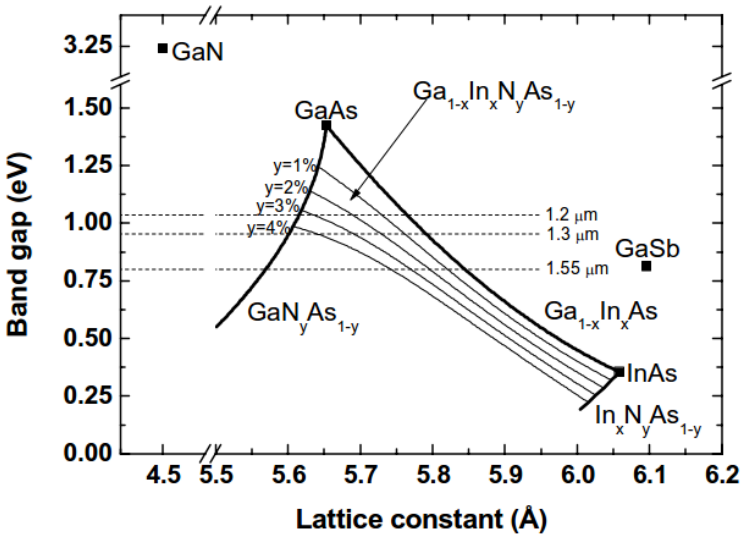

Figure 2.4. *Band gaps and lattice constants of $Ga_{1-x}In_xN_yAs_{1-y}$. Reprinted with permission from reference [62].*

The desirable properties of nitrogen are accompanied with some detrimental effects on the material quality challenges in the crystal synthesis. Firstly, dilute nitrides are metastable and have a large miscibility gap [45] which makes these compounds susceptible to clustering and phase separation effects. These effects become more severe with higher N concentrations and can deteriorate the material properties dramatically. Secondly, the incorporation of nitrogen is challenging since the solubility of N in thermal equilibrium is very limited [45]. For decent N concentrations, dilute nitrides have to be grown far from equilibrium conditions. In practice, this requires lowering the growth temperature significantly from GaAs growth temperature. At low growth temperatures point defect density is increased due to the lack of thermal energy which deteriorates the optical and electrical properties of the material. On the other hand, at higher growth temperatures, the phase separation becomes more probable. Practically, the growth temperature of dilute nitride compounds is a compromise between the point defects and phase separation. [7, 60] Thirdly, the short minority carrier diffusion lengths and relatively high background doping levels hinder the use of dilute nitrides [53].

Some of these N induced detriments can be relieved with thermal annealing. In thermal annealing the material is heated to high temperatures which enables short range ordering (SRO) of atoms in the crystal. SRO decreases the defect density and

relieves phase separation. This translates into better optical properties but also to blueshift of the emission wavelength [50].

One approach in increasing the material quality of dilute nitrides is to add antimony to the dilute nitride growth front [122]. Antimony is a group–V element that mainly acts as an surfactant, altering the growth kinetics and improving the quality of dilute nitride material. Antimony broadens the growth window of dilute nitrides; especially the growth temperature can be increased as Sb alleviates the phase separation effects. In addition to acting as an surfactant, some fraction of the Sb atoms is incorporated to the crystal. Like nitrogen, Sb decreases the E_g of the material, but unlike N, antimony affects the VB. [46] Models describing the band gap properties of GaInNAsSb has been developed, however, the composition analysis of quinary compounds is far from trivial, which has complicated the development and accuracy of band gap models for GaInNAsSb [2].

2.3 III–V heterostructures

Modern day epitaxial crystal growth methods have enabled the fabrication of complex layer structures consisting of different materials while maintaining the single crystal structure. The process of epitaxially layering materials with different properties is called heteroepitaxy. The properties of these heterostructures are determined by the constituent materials, layer thicknesses, and order of the layers. The III–V materials are very suitable for heteroepitaxy as the properties of the III–V materials can be adjusted by changing the material composition.

In epitaxy the crystal structure is grown on top of a single crystal substrate, and the overgrowing layer, epilayer, adopts the crystal structure of the substrate. In homoepitaxy the substrate and the epilayer materials are identical and, therefore, the single crystal structure is automatically preserved, assuming correct growth conditions. In heteroepitaxy the overgrowing materials are non-identical to the substrate material. If the lattice constant of the epitaxial film, a_f, deviates from the substrate lattice constant, a_s, the unit cell of the epitaxial film is deformed in order stay lattice-matched inducing strain to the epitaxial layer. This type of growth is called pseudomorphic growth. If $a_f > a_s$, the unit cell of the epilayer needs to compress in-plane, creating compressive strain. Similarly, if $a_f < a_s$, the unit cell needs to stretch in-plane, resulting in tensile strain. Strain induces changes to the band structure of materials causing the bands to shift relative to

each other, thus, altering the E_g. Monocrystalline structure is only preserved throughout thick heterostructures if the lattice constants of materials are nearly equal. Lattice-matching is generally favored in growth of solar cells. It is also possible to grow thin layers of mismatched materials, but if the epilayer thickness exceeds a critical thickness, it becomes energetically more favorable for the crystal to produce misfit dislocations in the interface, which relaxes some of the strain [71]. The misfit dislocations drastically deteriorate the properties of the structure.

When layers with different properties are stacked, local changes in the energy bands occur throughout the structure. In equilibrium the Fermi-level needs be constant throughout the structure, which requires shifting of the energy bands relative to each other, resulting in band bending [103]. The band properties of a heterostructure can be adjusted with material choices and doping levels. Different III–V compounds also possess non-identical refractive indices, and by stacking layers with different indices of refraction structures used for manipulating optical fields can be fabricated. For example, by alternating layers with unequal refractive indices, distributed Bragg reflector (DBR), can be fabricated. DBRs made from III–Vs are widely used in semiconductor disk lasers (SDL) [61] but DBRs are also useful in SCs as back reflectors [106].

3. SEMICONDUCTOR SOLAR CELLS

All types of solar cells convert the energy of photons directly into electricity, but the operation mechanisms differ between different SC technologies. In this chapter the operation principles and structures of semiconductor solar cells are discussed. First, the solar spectrum and fundamental operation principles of semiconductor SCs are introduced. Then the structure and operation of single- and multijunction SCs are reviewed.

3.1 Solar spectrum

The Sun produces energy by nuclear fusion, and the produced energy is mostly emitted as electromagnetic radiation into the surrounding space. The spectrum of the Sun closely follows the spectrum of an ideal blackbody radiator with effective temperature of 5772 K [116]. The intensity of solar radiation at the mean distance between the Sun and the Earth is about 1361 W/m^2 [59]; this value is also known as the solar constant. The Earth's atmosphere attenuates the intensity of solar irradiation, and at the surface of the Earth the intensity is 1120 W/m^2 (sun at zenith) [75].

As the sunlight passes through the atmosphere, atmospheric chemical compounds absorb and scatter the incident light. The compounds affecting the sunlight the most are water vapor, ozone, and carbon dioxide [75]. The effect of atmosphere on the spectrum is dependent on the optical distance the light travels in the atmosphere. For solar cell applications it's common to use airmass (AM) to take into account the atmospheric effects. The AM coefficient is defined as the ratio between the path length of light in atmosphere and the path length of light when the Sun is in the zenith. The air mass is commonly denoted with AM followed by the airmass coefficient in question.

For PV characterization different standard spectra have been defined; commonly used standards are ASTM E490–00 and ASTM G173–03. The ASTM E490–00 defines the solar spectrum outside the atmosphere (AM0) in wavelength range of 200 nm to 10 µm and the integrated intensity of the standard spectrum is 1366.1 W/m^2 [11]. The ASTM E490–00 spectrum is used for space applications of SCs. The ASTM G173–03 defines AM1.5G and AM1.5D spectra. AM1.5G is the global spectrum that includes the direct and diffuse components of radiation. The AM1.5G spectrum is commonly used for terrestrial flat panel SCs. AM1.5D, on the other hand, is the direct spectrum that includes direct sunlight and a circumsolar component in a 2.5° disk around the sun [12]. The AM1.5D spectrum is commonly used for concentrator applications. The integrated intensities of of AM1.5G and AM1.5D are 1000 W/m^2 and 900 W/m^2, respectively [86]. In figure 3.1 the standard AM0, AM1.5G, and AM1.5D spectra are illustrated.

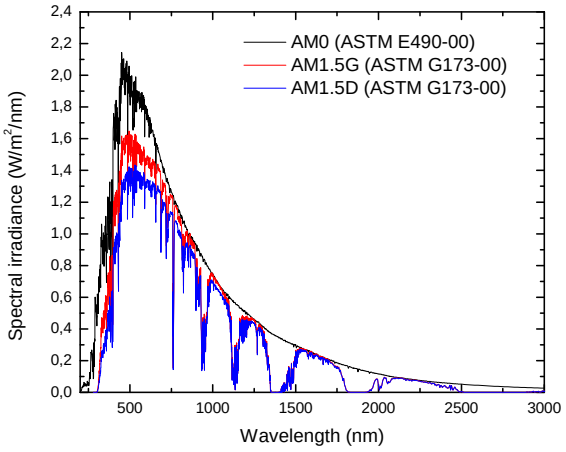

Figure 3.1. *Spectral irradiances according to ASTM E490–00 AM0, ASTM G173–03 AM1.5G, and ASTM G173–03 AM1.5D standards [86, modified]*

From the figure 3.1 the dips in the AM1.5 spectra caused by the atmospheric absorption are clearly visible. In addition, we notice the significantly higher ultraviolet (UV) content of AM0 spectrum compared to the AM1.5 spectra.

3.2 Basic operation principles of solar cells

In this section the operation principles of single junction SCs is considered. First the pn- and pin-junctions are discussed; without these, extracting of power from the

sunlight would be virtually impossible. The operation of the junctions is discussed mainly with pn-junction in mind, but the same principles are also mostly applicable for pin-junctions. After that the structure and operation of single-junction cells is discussed.

Pn- and pin-junctions

Even though extrinsic semiconductors are able to absorb EM radiation, and create EHPs, they act extremely poorly as SCs because charge carriers are not separated, and the recombination rate is high. The simplest case of a functioning SC is a structure called the pn-junction. The pn-junction spatially separates the charge carriers which reduces recombination of the photogenerated EHPs. A pn-junction is formed when p-type and n-type semiconductors are brought together. A charge carrier gradient forms at the material boundary, and the electrons diffuse from the n-layer to the p-type layer (vice versa for the holes) resulting in a diffusion current. Because the ionized impurity atoms are fixed to the crystal lattice, an imbalance is created in the net charges of the layers. A positive space charge is created near the junction boundary in the n-type layer, and a negative space charge is created in the p-type side of the junction. The space charges form an electric field at the pn-interface that points from the n-type towards the p-type layer. The electric field tends to keep the majority carriers in their respective sides but also sweeps minority carriers to the other sides of the junction, where they become majority carriers. The electric field causes the space charge region to be empty from any carriers which is why it often is called the depletion region. The width of the depletion region is determined by the doping levels and doping profiles of the constituent layers, and it extends further into the layer with lower doping level [103].

The charge separating nature of the electric field creates a drift current component that opposes the diffusion current. In thermal equilibrium, without external circuit, the net current and the voltage over the junction are zero. The potential caused by the electric field in thermal equilibrium is called the built-in potential. In thermal equilibrium the Fermi-levels of the p- and n-type regions are aligned, and the energy bands are bent at the interface. The potential energy separation of corresponding bands on the different sides of the interface is equal to the energy difference between the Fermi-levels of the doped layers. [103] The formation of a pn-junction is illustrated in figure 3.2.

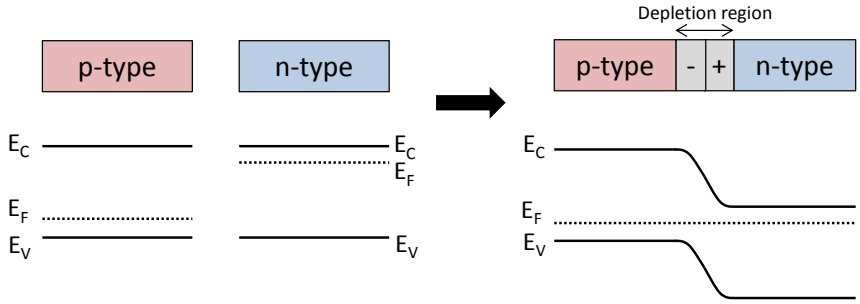

Figure 3.2. *Formation of a pn-junction and the energy bands in thermal equilibrium.*

Pin-structure is a modification of the pn-junction where an additional intrinsic (i.e. undoped) layer is inserted between the p- and n-type layers. Again, the Fermi-levels align which causes the built-in potential to be formed, but now the electric field is ideally extended across the i-layer. The electric field in the i-layer varies linearly between the values determined by the doped layers which results in elongation of the depletion region. In many cases the pin-junction is fabricated as a heterojunction, meaning that the p- and n-type layers are made of different materials than the i-layer. [103]

Biased junction under dark conditions

By applying an external voltage across the junction, the thermal equilibrium can be broken causing changes in the internal dynamics of the junction. When a positive bias is applied, the electric field inside the junction is reduced. This configuration is called forward biasing. The reduction in the internal field decreases the diffusion barrier, which increases the diffusion of carriers across the depletion region, causing a positive net current. When a negative bias is applied, the junction becomes reverse biased. When reverse bias is introduced, the electric field inside the junction is amplified which reduces the diffusion current. Because the drift current is limited by the number of minority carriers on each side, the net current in reverse bias mode is virtually non-existent. Still, thermal excitation creates carriers on both sides of the junction, and some of the thermally generated minority carriers reach the depletion region where they are swept across to the other side causing a small negative current. With small reverse bias voltages, the positive current increases but then saturates as the bias voltage is further increased. This current is called a dark saturation

current. The dark saturation current increases with temperature and decreases with improving material quality. [103] If the reverse bias voltage is increased sufficiently, a reverse breakdown takes place which causes the reverse current to rise rapidly. Without illumination the current through the diode as a function of voltage (without taking the breakdown effects into account) can be expressed with a diode equation:

$$I = I_0(e^{\frac{qV}{nk_BT}} - 1), \tag{3.1}$$

where I_0 is the dark saturation current, q is the elementary charge, V is the voltage across the junction and n is the ideality factor [103]. The curve obtained with 3.1 is commonly called an IV curve. The current through a diode under dark conditions is illustrated in figure 3.3.

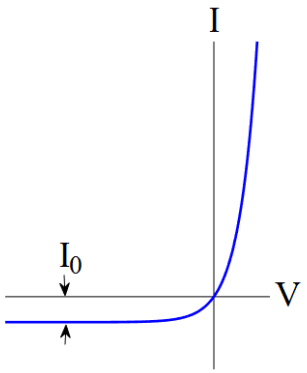

Figure 3.3. *Diode current without illumination as function of voltage.*

The ideality factor, n, can have values ranging between one and two. Recombination in the structure causes n to have values larger than unity, therefore, n is dependent on the material and temperature. [70]

Biased junction under illumination

When pn-junction is exposed to light, the junction absorbs photons with energies higher or equal to the E_g of the material. The absorption process creates an EHP in the semiconductor material. If $E_{ph} > E_g$, the excess energy is converted into phonons (i.e. heat) in the crystal. If a photon is absorbed in the depletion layer, the generated carriers are separated by the electric field to the opposite sides of the

junction. The drift of carriers weakens the internal field, biasing the junction in the forward direction. The apparent forward biasing under illumination is known as the photovoltaic effect [103]. If the p- and n-sides are connected by an external load, the carriers flow through the load creating a negative current. If the photon is absorbed in the regions outside the depletion region, the photogenerated minority carriers within the average diffusion length are likely to diffuse to depletion region and contribute to the photocurrent. The photocurrent is added to the dark current of the diode which causes the dark-IV curve of the diode to be shifted as the junction starts to generate power. Essentially, the diode's light biased current–voltage curve (LIV) is a superposition of the dark-IV curve, and the magnitude of shift is relative to the photocurrent that on the other hand, is proportional to the intensity of incident light. Because the junction is producing current under illumination, convention is to invert the current axis of the LIV (i.e. the signs are changed in 3.2). The current through the pn-junction can now be expressed as

$$I = I_L - I_0(e^{\frac{qV}{nk_BT}} - 1), \tag{3.2}$$

where I_L is the photocurrent. The LIV and dark-IV curves of a diode are illustrated in figure 3.4 with inverted current axis.

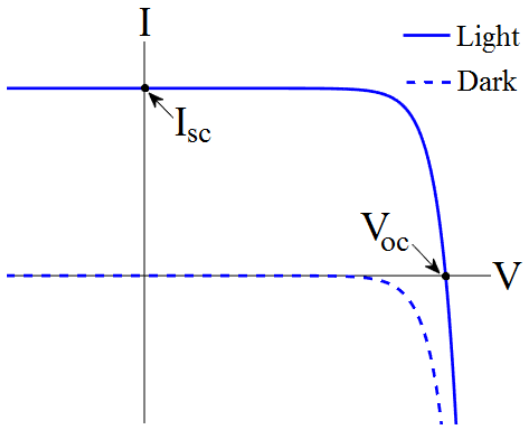

Figure 3.4. *Diode current with and without illumination as function of voltage. The current axis has been inverted according to the conventions.*

From the 3.4 we can see that the LIV curve intersects with both axes, and these points are important when describing the quality and performance of SCs. The

current corresponding to the point where $V = 0$ is called the short-circuit current, I_{sc}. In short-circuit condition all the created carriers recombine through the external circuit and no reduction in the internal field is observed. I_{sc} is directly proportional to the intensity of incoming light and, in practice, $I_L \approx I_{sc}$ if the series resistance is low [18]. Therefore, I_L can usually be replaced with I_{sc} in equation 3.2. The I_{sc} can be interpreted as the maximum current that can be extracted from a SC under certain illumination. Another point of interest is the point where $I = 0$. The value of voltage at this point is called the open-circuit voltage, V_{oc}. At open-circuit condition no current flows through the external circuit causing the internal field to be reduced to a point where it cannot separate EHPs anymore. V_{oc} corresponds to the maximum voltage available from the junction. Other way of interpreting the V_{oc} is that it's the amount of forward biasing caused by the photogeneration. V_{oc} of junction can be approximated with

$$V_{OC} \approx \frac{k_B T}{q} ln(\frac{I_{sc}}{I_0}), \tag{3.3}$$

when $I_{SC} >> I_0$. The approximation is valid for good quality SCs under sufficient illumination.

Single-junction solar cells

Single-junction SCs have a single pn- or pin-junction in their structure. The junctions can, in principle, function as SCs by themselves, but in order to have a well functioning single-junction device, the junction needs to be properly designed and additional layers and structures are required. In this section the structure of actual semiconductor single-junction SCs is considered.

In the previous section we discussed only the principles of pn- and pin-junctions without taking into consideration the actual design of the junctions. First we have to take into account the absorption of photons in the pn-junction. Previously, we assumed that the photons can be absorbed in any part of the junction. In reality, majority of the suitable photons are absorbed near the front surface of the junction. The light intensity attenuates exponentially in the semiconductor according to the Beer–Lambert law. This means that if we have a thick pn-junction, only a fraction

of the incident photons are absorbed in the depletion region where the collection probability is high. Instead, the minority carriers created near the surface need to diffuse to the depletion region in order to be collected. As mentioned, only minority carriers created at average diffusion lengths away from the depletion region can be effectively collected. Therefore it's beneficial to make the front side of the junction very thin and more heavily doped, so that a larger fraction of photons would be absorbed in the depletion region. Because the diffusion lengths for holes are shorter than for electrons, it's beneficial to make the n-side, where holes are the minority carriers, the thin side of the junction. The heavily doped side and the lightly doped side are conventionally called the emitter and the base, respectively. As the emitter is made very thin, most of the photons are now being absorbed by the base, the base is also sometimes referred as the absorber. [38]

In pin-SCs the doped outside layers are made very thin so that the photons are mostly being absorbed by the intrinsic layer, thus, the i-layer is referred as the absorber layer in the pin-configuration. Because the electric field spans over the i-layer the collection probability is increased. The pin-configuration is preferrable especially with materials with short minority carrier diffusion lengths, such as dilute nitrides; for these materials low background doping levels are essential in the pin-structure [85].

For efficient extraction of carriers, ohmic contacts need to be fabricated on both sides of the junction. Ohmic contacts ensure low resistive losses and linear IV behavior of the metal–semiconductor interface [30]. When metal–semiconductor contact is formed, the Fermi-levels are again aligned. For ohmic contacts the work potential (the potential difference between Fermi-level and vacuum level) of the metal needs to be appropriate. In n-type material the work potential of the metal needs to be lower than the semiconductor's (vice versa for p-type semiconductors) [103]. This creates constraints on the metals that can be used for the contacts. Other practical way for obtaining ohmic contacts is to heavily dope the contact regions. In this method, if a barrier is formed at the metal–semiconductor interface, the barrier region becomes so narrow that carriers can tunnel through it. [103] Because light needs to reach the semiconductor material, the front contact cannot cover the whole front surface which is why patterned front contact is essential for SC operation. The back contact, on the other hand, can cover the whole back surface.

The power generated by the SC under illumination can be expressed with the product of voltage and current at each point of the LIV curve. The maximum power, P_{mp}, is produced at the point where $V = V_{mp}$ and $I = I_{mp}$. In real SCs $V_{mp} < V_{oc}$ and $I_{mp} < I_{sc}$, and the P_{mp} is usually found around the "knee-point" of the LIV curve. With the P_{mp}, the V_{oc}, and the I_{sc} a parameter called the fill factor, FF, can be defined. The FF is defined by equation

$$FF = \frac{V_{mp}I_{mp}}{V_{oc}I_{sc}} = \frac{P_{mp}}{V_{oc}I_{sc}}. \tag{3.4}$$

The FF essentially is a measure of the "squareness" of the LIV curve and, therefore, effectively describes the quality of the SC. Another important value describing the performance and quality of a SC is the conversion efficiency. The conversion efficiency under certain illumination conditions is the ratio between the maximum power extracted from the SC and the incident power of illumination on the SC. The total conversion efficiency of a SC can be written as

$$\eta = \frac{P_{mp}}{P_{in}} = \frac{FFV_{oc}I_{sc}}{P_{in}} = \frac{FFV_{oc}I_{sc}}{P_{in}} = \frac{FFV_{oc}I_{sc}}{I_{light}A_{SC}}, \tag{3.5}$$

where P_{in} is the power of incident illumination, I_{light} is the intensity of incident light, and A_{SC} is the area of the SC. By substituting $\mathrm{A_{SC}}$ in equation 3.5 with the active area of the SC, $A_{SC,active}$, the active area efficiency η_{active} can be obtained. By analyzing the equation 3.5 we may notice that for obtaining highest possible efficiency the product of FF, V_{oc} and I_{sc} needs to be maximized.

The I_{sc} is proportional to internal collection efficiency and the photogenerated current. Internal collection efficiency, on the other hand, depends inversely on the recombination losses inside the cell. The recombination losses can be reduced by (i) increasing the material quality and (ii) by minimizing the recombination losses at the front and back surfaces. Defects in the crystal can act as recombination centers, thus, as the material quality is improved, and the defect densities drop, recombination is reduced. For reducing the surface recombination losses, heavily doped window and back surface field (BSF) layers can be introduced to the front and back surfaces of the junction, respectively. The window and BSF layers are

typically made of materials with higher E_g than the junction. These additional layers create barriers in the band structure for the minority carriers that prevent the generated minority carriers from diffusing to the contacts which increases the collection probability. [79]

To maximize the I_{sc} the contact shadowing and reflective losses need to be minimized. In addition, the cell needs to be made sufficiently thick so that enough photons are being absorbed. The contact shadowing can be reduced with front contact grid design. The reflection losses at the air-semiconductor interface can be significantly lowered with an anti-reflection coating (ARC). ARC is an optical structure that uses interference effects to reduce the reflectivity. Typically, the ARC can be realized by depositing dielectric layers on top of the SC. The reflective properties of ARC can be tailored by choosing materials with suitable refractive indices, and by tailoring the thicknesses of constituent ARC layers. Double layer coatings, such as TiO_2–SiO_2 [4, 121] and SiN_x–SiO_x [120], are widely used in SCs s they offer minimum reflection in broader wavelength range compared to single layer coatings. A novel approach on ARCs is bio-mimicking nanopatterning. The sub-wavelength nanopatterns effectively cause light to feel a continuous refractive index gradient which reduces the reflectivity. The patterns can be fabricated either into a separate dielectric layer [65], or directly into the window layer of the SC [8].

The V_{oc} could be approximated with equation 3.3 from which we could see the logarithmic proportionality to the ratio between I_{sc} and I_0. The value of the logarithm is maximized when I_{sc} is maximized and I_0, on the other hand, is minimized. The methods for increasing the I_{sc} were introduced above, but the I_0 can reduced with high minority carrier lifetimes and low surface recombination velocities [38]. In other words, the V_{oc} is increased when recombination of carriers is minimized throughout the SC. The value of V_{oc} is also dependent on the E_g of the cell. This is because the I_0 is proportional to the square of intrinsic carrier concentration in the material, and the intrinsic carrier concentration, on the other hand, is exponentially increased with decreasing E_g [79]. In other words, the minimum dark saturation current is higher for cells made of materials with low E_g. Even though the I_{sc} increases with lower E_g values, the V_{oc} decreases due to the exponential increase in I_0 with lower E_g.

Schematic representations of a typical single-junction solar cells with pn- and pin-configurations with a picture of real SC are presented in figure 3.5.

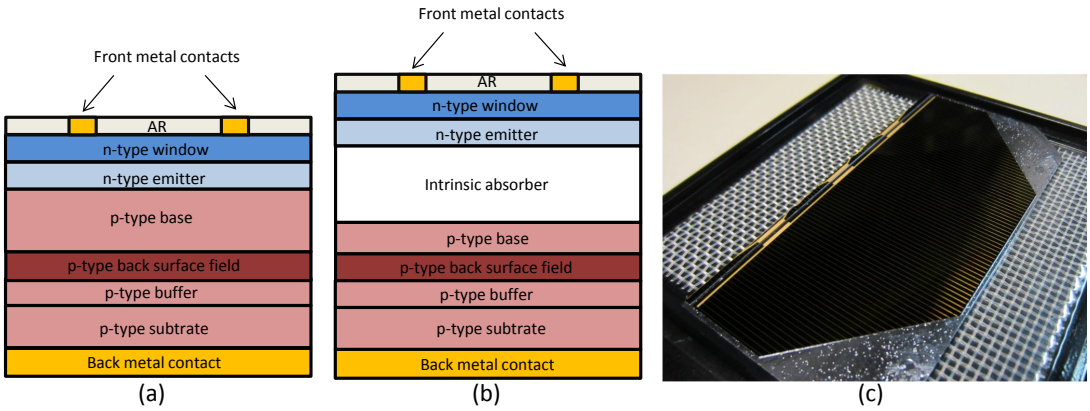

Figure 3.5. *Schematic illustrations of typical structures of (a) a pn-SC and (b) a pin-SC with n-on-p configuration, and (c) a space solar cell fabricated at ORC.*

In addition, parasitic resistances, that were not taken into account in 3.1 and 3.2, are present in actual solar cells. In the presence of parasitic resistances the diode equation can be written as

$$I = I_L - I_0(e^{\frac{q(V+IR_s)}{nk_BT}} - 1) - \frac{V + IR_s}{R_{sh}}, \tag{3.6}$$

where R_s is the series resistance and R_{sh} is the shunt resistance. The parasitic resistances mainly affect the FF but can also affect the values of I_{sc} and V_{oc} with extreme values. Series resistance, R_s, is a resistance component that is in series with the diode that is caused by current traversing through the materials, contact resistance between the metal and the semiconductor, and the resistance of the metal contacts. The resistive losses caused by series resistance are directly proportional to the value of R_s, thus, the FF can be increased by reducing the R_s. R_s has no effect on the V_{oc} but very large values of R_s cause decrease in the I_{sc}. Shunt resistance, R_{sh}, is a parallel resistance component that is typically caused by manufacturing defects that offer an alternate path with low resistance for the current. The losses caused by shunt resistance are inversely proportional to the value of R_{sh}, and the value of R_{sh} can be increased by minimizing defects in the SC and by optimization of the SC processing. If R_s is very small the effect of R_{sh} on the I_{sc} is negligible but, on the other hand, very small values of R_{sh} lower the V_{oc}. [38]

3.3 Multijunction solar cells

In multijunction architecture the solar spectrum is split between multiple subcells. This way the solar energy can be harvested more efficiently as losses are reduced with increasing number of junctions [49,112]. There are several options for the realization of MJSCs [5] but one common way is to connect the subcells electrically and optically in series. The stacking of the subcells can be done with several techniques such as monolithic growth [9] or wafer bonding [27]. The stacked configuration also creates a need for special structures in the SC. In this section we explore the design and operation of monolithic MJSCs.

MJSCs incorporate two or more junctions in their structure. Each subcell absorbs photons with energies $E_{ph} \geq E_{g,i}$ with $E_{g,i}$ being the band gap energy of ith subcell. For successful spectral splitting the subcells need to be arranged such that the light is first incident on the cell with highest E_g. The photons with insufficient energy are not absorbed by the overlaying subcell, instead, they are transmitted to the underlying subcells to be collected. The principle of spectral splitting in 3J SC is illustrated in figure 3.6.

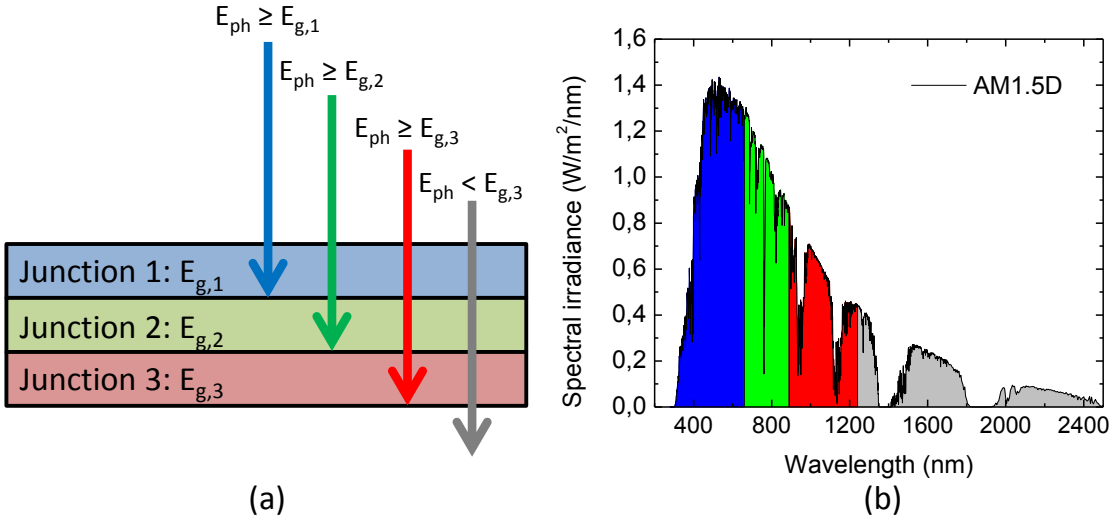

Figure 3.6. *The principle of spectral splitting (a) inside an optically stacked 3J, and (b) from the spectral point-of-view. The depicted spectrum is an ASTM G173–03 AM1.5D spectrum [86].*

The figure 3.6 depicts a situation where all of the suitable photons are absorbed by the overlaying subcells. This holds true only for sufficiently thick subcells as the light intensity decays exponentially inside the material. In reality, it's common

that some fraction of the suitable photons are passed through the top cells to the underlying subcells. This can also be used as an advantage when designing multijunction structures.

Beside being optically in series, in monolithic approach the subcells are also electrically in series. The subcells cannot be brought directly in contact as a pn-interface in the opposite direction would be formed at the subcell interface. Instead, the electrical connection is realized with tunnel junctions (TJ). TJs are thin, extremely highly or degenerately doped pn-junctions with inverted polarity between the subcells. TJ also creates a pn-junction in the opposite direction but the high doping levels of the TJ layers cause the depletion region to be very narrow. If the doping levels are sufficient, the barrier between the bands becomes so narrow that the probability of electron tunneling becomes significant. Proper tunneling ensures a low resistance contact between the subcells. The tunneling properties of the TJ are highly dependent on the doping levels and E_g of the TJ material. [79] In figure 3.7 the band diagram and operation of a TJ is illustrated.

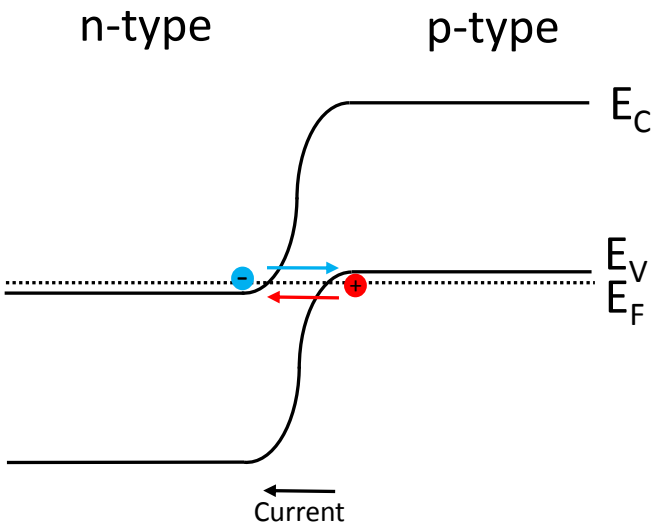

Figure 3.7. *Band diagram and operation of a tunnel junction between subcells. The tunneling directions of electrons and holes are depicted with blue and red arrows, respectively. The black arrow illustrates the direction of current flow.*

Beside having good electrical properties, the TJ should also be highly transparent to the incident light. If the TJ region absorbs too much of the incoming light can affects the current generation of the underlying cell. For this reason, the E_g of TJ should be greater than the E_g of the SC below or, alternatively, the TJ needs to be made very thin.

The individual subcells of a MJ device essentially follow the same current–voltage equations introduced earlier, but the electrical connection between the subcells needs to be taken into account. First, the total current through MJ device is limited by the smallest current of the subcells, given that the tunneling current through the TJs is sufficient. In an ideal situation all the subcells would generate the same current, i.e. the junctions would be current-matched. In reality, perfect current-matching is rarely achieved, and one of the subcells limits the cell current. Secondly, due to the serial connection of the subcells, the voltage of a MJSC is the roughly the sum of voltages of the individual subcells. The overall shape of an LIV curve of a MJSC is determined by the LIV characteristics of the subcells. The LIV curve of a MJSC can be approximated with following equations:

$$I_{MJ} = min(I_i), \quad i = 1, 2, 3, ...m, \tag{3.7}$$

$$V_i = \frac{nk_BT}{q} ln(1 + \frac{I_{L,i} - I_{MJ}}{I_{0,i}}) - I_{MJ}R_{s,i}, \quad i = 1, 2, 3, ...m \tag{3.8}$$

$$V_{MJ} \approx \sum_i V_i, \quad i = 1, 2, 3, ...m, \tag{3.9}$$

where I_{MJ} is the current through the MJSC, I_i is the current of ith subcell, m is the number of subcells in the configuration, $I_{L,i}$ is the light generated current of ith subcell, $I_{0,i}$ is the dark saturation current of ith subcell, $R_{s,i}$ is the series resistance of ith subcell, and V_{MJ} is the total voltage over the MJSC. For simplicity R_{sh} is neglected in equation 3.8, which is a valid approximation for good quality SCs [3].

The same basic rules for obtaining high efficiencies with single-junction SC can be applied also to MJ devices. In MJSCs high V_{oc} is obtained when the open-circuit voltages of the individual subcells are high and TJs work properly. For high I_{sc} the current generation in all the subcells needs to be high but sufficient current-matching is required. For good current-matching the band gaps and optical thicknesses of the subcells need to be properly chosen. The overall FF in MJSCs is highly dependent on the current-matching as the FF of a MJSC is mainly determined by the current-limiting subcell [79]. A high overall FF can be obtained by employing subcells with high FFs.

3.4 Effect of temperature on cell performance

The performance of a SC is greatly affected by ambient temperature, and depending on the application the temperatures can vary largely. As mentioned in chapter 2, the E_g of semiconductor narrows with increasing temperature which, in turn, results in absorption of photons with lower energies. In single-junction SCs this directly translates into higher photocurrent, which can be observed as increased I_{sc}. In principle, this is also the case with MJSCs but because the temperature coefficients of band gap energies are unequal between materials, a situation can occur where the current balance between subcells is shifted. This can cause one subcell to be the current-limiting cell at certain temperature but in different conditions another junction may become the current-limiting cell. The incident spectrum also has a significant effect on the current balance of MJSC as the photon distribution in the spectrum is not constant. Especially, the terrestrial spectrum, due to the absorption dips, may cause shifts in the current balance when cell temperature is changed (see figure 3.1).

From equation 3.3 we could easily assume that the V_{oc} would be directly proportional to the temperature, but actually the logarithmic ratio between I_{sc} and I_0 dominates the temperature dependence of V_{oc}. The $\mathrm{I_{sc}}$ was found to increase with temperature which would be seen as increase in V_{oc}, but also the I_0 increases with temperature since more carriers are thermally created in the vicinity of the depletion region. The increase in I_0 is exponential due to Fermi–Dirac statistics, and overpowers the increase of $\mathrm{I_{sc}}$ causing the value of the logarithm in equation 3.3 to diminish with temperature. Consequently, a negative temperature dependence of V_{oc} is typically observed. Because the voltages in MJSC are additive, the temperature dependence of V_{oc} in MJSC is also the sum of temperature dependencies of the individual subcells [24].

In single-junction solar cells the temperature dependence of FF is negative, and the magnitude of $\frac{\mathrm{dFF}}{\mathrm{dT}}$ is decreased as V_{oc} is increased. In some rare cases the $\frac{\mathrm{dFF}}{\mathrm{dT}}$ can become positive. [15] In serially connected MJSCs the $\frac{\mathrm{dFF}}{\mathrm{dT}}$ change with the degree of current mismatch, and can not be expressed analytically [15]. In addition, the series resistance is found to affect the temperature behavior of FF; $\frac{\mathrm{dFF}}{\mathrm{dT}}$ is observed to increase with R_s [35].

Because the conversion efficiency is proportional to the product of FF, V_{oc} and I_{sc} the $\frac{\mathrm{d}\eta}{\mathrm{dT}}$ is defined by the individual temperature dependencies of these parameters.

Typically, the conversion efficiency is decreased with temperature because the positive change in I_{sc} is smaller than the negative change in the product of FF and V_{oc}. Studies of temperature dependencies in III–V MJSCs have been previously published [55, 96], but for cells employing dilute nitride subcells the number of studies is limited [6].

3.5 Concentrated photovoltaics

In concentrated photovoltaics (CPV) the incident light is focused from a large area to a small SC with lenses or mirrors. When the light is focused to the cell, the intensity of the incident light is increased. The ratio between concentrated and one-sun light intensity is called a concentration factor, X. The concentration factors depend on the application and type of cell, but for III–V concentrator applications X usually ranges from 300 to 1000 [5]. The concentration of light has two major benefits: (i) under concentrated light the cell area can be drastically reduced and (ii) the conversion efficiencies can significantly improve under concentration. The cell efficiencies may improve up to 10 percentage points under CPV conditions [5]. The smaller cell size directly translates to lower production costs as less material is required, and higher efficiencies reduce the payback times of CPV systems as more energy can be produced. Drawbacks of the CPV technology lie in the system level as concentrator optics and an active solar tracking are required.

The concentration of light influences the LIV characteristics of the SC. First, the I_{sc} grows with concentration. The increase of I_{sc} in MJSCs is typically linear [55] but luminescent coupling can cause deviations from linearity [26, 37, 102]. Secondly, the V_{oc} is increased with concentration because the I_{sc} grows but the I_0 does not change substantially (see equation 3.3) [38]. These effects mainly account for the increase in efficiency with concentration, but also the ideality factor and FF are dependent on the concentration. Typically, n remains nearly constant up to high concentration levels if the temperature of the SC is kept constant, but the value of FF usually starts to drop at concentration levels of around 400-1000 [5].

The light concentration also causes the SC to heat up more compared to the one sun illumination and, consequently, operating temperatures up to 60℃ above the ambient temperatures [95] can be realistically expected. The temperature effects are similar to the one-sun operation but are not as radical as the impact of changing I_0 is relatively small with CPV operation.

4. FABRICATION OF III–V SOLAR CELLS

Compound semiconductor structures can be fabricated with several techniques. Currently, the majority of III–V SCs are being made with metal-organic chemical vapor deposition (MOCVD). However, MOCVD has failed to produce dilute nitride materials with adequate quality for solar cell applications [44]. At the same time, molecular beam epitaxy (MBE) has become a viable candidate for the production of high-efficiency SCs [53]. In this chapter the operation principles of plasma-assisted molecular beam epitaxy and the fabrication of III–V solar cells are discussed.

4.1 Plasma-assisted molecular beam epitaxy

Molecular beam epitaxy is a versatile technology for epitaxial growth of materials that was invented in the late 1960s [21]. In MBE, atomic or molecular beams of elements are directed onto a heated single-crystal substrate under ultra high-vacuum (UHV) conditions where the epilayer crystallizes on the substrate surface. Mechanical shutters are used for modulating the material beams which offers high control over the growth and enables abrupt modulation of composition and doping profiles [32]. The UHV conditions of MBE have two major benefits; first, it makes possible to grown materials far from thermodynamical equilibrium [48] which translates into reduced concentration of thermodynamical defects [32] and, secondly, it makes possible to use in situ diagnostic methods, e.g. reflection high-energy electron diffraction (RHEED) and pyrometry [48]. Many material classes have been fabricated with MBE technology but most of the development has been done on III–V compounds [32]. From this point forward the discussion is only on molecular beam epitaxy of III–V compounds.

Multiple variants of MBE technology exist with solid source MBE (SSMBE) being the most widely used. In SSMBE the material beams are produced by heating ultra-pure elemental source materials, such as Ga and As, until they transform to

gaseous phase either by evaporation or by sublimation. The source materials in SSMBE are initially loaded in their solid phase, hence the naming. A sub-variant of SSMBE is the plasma-assisted molecular beam epitaxy (PAMBE) where one or more (usually nitrogen, hydrogen or oxygen) materials are introduced to the growth via their plasma-phase.

Structure and equipment of MBE system

Modern MBE systems are modular, and the assembly of an MBE system depends on the material system and application. Different modules have their own functionalities, and they are isolated from each other by gate valves. The loading wafers is done through the fast-entry lock, and it is also used for the initial evacuation of the system. Fast-entry locks incorporate heating systems for thermal desorption of physisorbed gases introduced to the system during loading. Preparation module is a chamber under UHV conditions in which the substrates are prepared before the epitaxy. The preparation mainly means heat treatment for the substrates, but other steps can also be performed depending on the system [48]. The growth module is the main module of a MBE system where the crystal growth is performed. Generally, the ggrowth module comprises the material sources, shutters, UHV pumping, liquid-nitrogen cryopanel, a manipulator with heating and rotation, ionization gauges for pressure monitoring and flux measurement, RHEED system, and a mass spectrometer for residual gas analysis. In many MBE systems an additional cryopanel is located around the material sources to minimize cross-contamination of materials. [48] A schematic illustration of an MBE reactor is depicted in figure 4.1.

The pumping of a MBE reactor can be arranged in many different ways. Typically, it's done with a diffusion pump, an ion pump, a turbomolecular pump, a titan ion sublimation pump or a cryopump, or as a combination of these techniques [63]. The cryopanel is used for capturing atoms from beam fluxes that are not incorporated to the crystal into the panel walls, thereby also offering additional pumping for the reactor.

In MBE the group–III elements and the dopants are typically introduced via Knudsen-type effusion cells (K-cells) where pure source materials, placed in crucibles in their solid or liquid phase, are heated to obtain a fluxes of evaporated

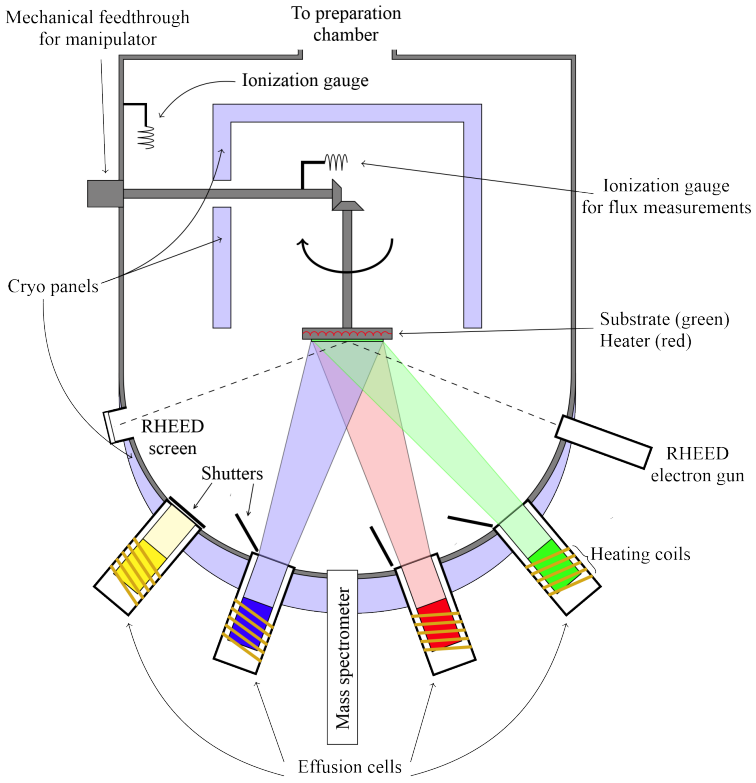

Figure 4.1. *Schematic of an MBE reactor [80, modified].*

materials. The material fluxes are controlled by the cell temperatures. The crucibles are typically made of pyrolytic boron nitride (PBN) as it can withstand temperatures up to 1400℃ [48]. Dual-filament sources that incorporate a second heating element near the crucible orifice have become popular in Ga and In sources. The additional filament is used to minimize material condensation, but it also allows more precise control over fluxes. [117] The group–III materials, Ga, In and Al, are loaded initially in solid form but are subsequently liquified. Common dopants (e.g. Si and Be), on the other hand, remain solid during use.

Due to the high vapor pressures of P, As, and Sb, the group–V elements are commonly introduced by using cracker cells that thermally dissociate tetramers into dimers (e.g. As_4 into As_2) [92]. In the cracker cells the bulk material is sublimated from the solid phase in temperatures < 500℃; in these temperatures the dominant species generated are tetramers (e.g. As_4) [92]. The sublimated material is then thermally dissociated into dimers (e.g. As_2) in a high-temperature cracking stage (800-1000℃) [117]. The use of dimers instead of tetramers has two main advantages: (i) the growth kinetics are more preferable [32] and (ii) the

material consumption is decreased due to higher sticking coefficients of dimers [92]. Modern cracker cells usually incorporate a needle valve between the bulk and cracking stages which is used for fast control over the material flux [89].

Nitrogen in it's standard form, N_2, is a very inert molecule and for crystal growth more reactive species of N need to be generated [25]. The dissociation energy of N_2 is so high that thermal cracking is not possible and alternative methodd for producing reactive atoms needs to be considered. Several different types of N-sources have been used but the most widely used type is the radio-frequency (RF) source [25]. In RF sources pure nitrogen is fed into the source bulb (usually made of PBN) surrounded by RF coils. The coils provide adjustable RF power that is coupled to the gas which ignites and maintains the plasma. The plasma contains many species of nitrogen: neutral molecules (N_2), excited molecules (N_2^*), ionized molecules (N_2^+), atomic (N) and ionized atoms (N^+) [118]. (N_2^*) and N are the main incorporating species [17] whereas ionized forms cause damage to the crystal [45]. The active species are directed to the sample through an aperture containing small holes which ensures a uniform distribution of material on the crystal, as well as, increases the pressure inside the plasma bulb decreasing the ion concentration as the collision probability is increased. Another way for reducing the number of ions is to use ion deflectors in front of the aperture. The main reasons for the popularity of RF sources are the relatively low ion count and the high dissociation yield provided by the method [56].

Crystal growth with MBE

The crystal growth takes place on a heated substrate crystal inside the growth module. In a simplified growth process, the constituent atoms thermally migrate on the substrate surface until they find vacant lattice sites where they incorporate into the solid phase. The atoms from group–III and group–V are distributed randomly to their respective sublattices. [32]. In reality, the growth process isn't that simple, and there are four main processes happening on the growth front: (i) adsorption of impinging atoms or molecules on the substrate surface, (ii) surface migration and dissociation of adatoms, (iii) incorporation of adatoms to the crystal lattice, and (iv) desorption of unincorporated adatoms. The rates of these processes are determined by the growth conditions, but due to the non-equilibrium growth conditions, the growth is said to be kinetically limited by the substrate temperature. [48] The crystal can grow with different growth modes that are dependent upon the lattice misfit

between materials, material fluxes, the growth temperature, and the adhesion energy [47] In many of the epitaxial applications (e.g. growth of SCs) planar Frank-van der Merve (FM) growth mode is desired as it produces smooth surfaces with good quality interfaces.

The growth conditions play a major role in the crystal growth as they modify the growth kinetics and, thus, suitable parameters need to be chosen for all the materials. The growth kinetics are largely dictated by interplay the growth temperature (T_g) and the flux ratios. Beside these factors, the surface orientation of the substrate and the growth rates have an additional effect on the growth. Growth temperatures for different compounds can be found within a certain temperature window, set by processes limiting the crystal quality at the window boundaries. At the low temperatures the crystal quality is limited by the thermal energy as the atoms have insufficient energy to migrate to proper nucleation sites. The lack of thermal energy leads to formation of point defects and rough surfaces. At high substrate temperatures the re-evaporation of adsorbed species becomes significant which can lead to changes in material composition and growth rates [82]. A practical upper limit for the T_g is the congruent sublimation temperature where equal amounts of constituent atoms of a binary are desorbed from the surface. For more complex compounds the temperature can be estimated from the congruent sublimation temperatures of constituent binaries by the Vegard's law [20]. The T_g's typically range from 500℃ to 650℃ for traditional compounds [60]. Lower growth temperatures are often used for achieving very high dopant concentrations [72]. Dilute nitrides, on the other hand, need to be grown in significantly lower temperatures than GaAs, due to the limited solubility of N [7, 45].

The group–III elements have a near unity sticking coefficients and the MBE growth of III–V compounds is typically carried out under excess group–V flux to maintain the stoichiometry, and the growth rates are essentially limited by the group–III fluxes. The excess group–V atoms are evaporated from the substrate with the thermal energy gained from the substrate. The V/III beam equivalent pressure ratios of 2–10 are typically used for GaAs-based compounds. [82] The V/III ratio has a similar effect to the growth as the growth temperature; too high and too low V/III ratio values effectively correspond to growths at too low and too high temperatures, respectively. The V/III ratio can be used to compensate group–III desorption as it effectively shifts the desorption temperatures. [10] As

the growth rate is typically limited by the group–III fluxes, the maximum growth rates in MBE are limited by the operation temperatures of the cells. The typical growth rates are usually in the range of 1 µm/h. Higher growth rates can be obtained by using multiple sources for the same material. The growth rates also affect the surface reconstructions [84] and defect densities [64]. The control over the group–III composition is relatively easy as it can be controlled by changing the relative fluxes. Due to the excess group–V flux the group–V composition is much harder to control as the elements compete for the lattice sites.

MBE system used for this thesis

The SC structures studied in this thesis were grown with a Veeco GEN20 reactor (figure 4.2). The system supports wafers up to 4 inch diameter.

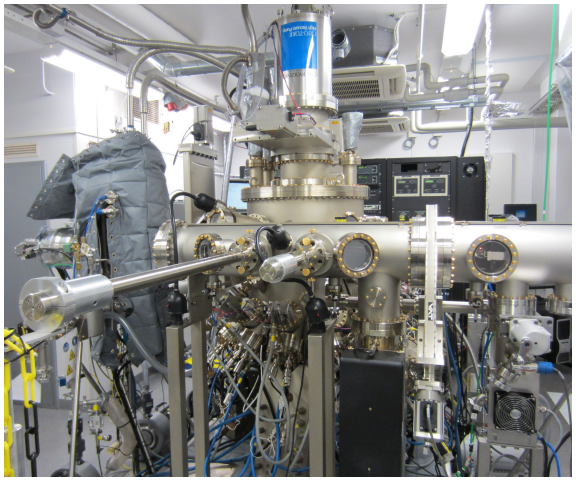

Figure 4.2. *Veeco GEN20 MBE reactor.*

The GEN20 reactor accommodates 14 ports for material sources. Veeco's SUMO cells are used for the group–III materials, Al, Ga, and In; two of each. The dual cell configuration enables higher control over material compositions but also higher growth rates. The GEN20 has four group–V sources: arsenic, phosphorus, antimony, and nitrogen. As, P, and Sb are introduced via Veeco's valved cracker sources. The nitrogen is introduced by Veeco's UNI-Bulb RF plasma source equipped with an automatic impedance matching unit. Si and Be sources are used for material doping. The growth chamber is pumped with three main pumps: a cryo pump and two turbomolecular pumps. Accurate temperature monitoring of the wafers is

performed by pyrometer and band-edge thermometer. For in-situ diagnostics the GEN20 system incorporates a mass spectrometer and a RHEED system.

4.2 Growth of multijunction III–V solar cells with MBE

The epitaxial growth of multijunction cells can be very challenging as the MJSC layer structures become increasingly complex when the number of junctions is increased. For obtaining good quality and high-efficiency MJSCs each layer needs to be grown at right conditions, and they need to have proper thicknesses, compositions and doping levels. At the same time, the material interfaces need to be sharp and surface roughness needs to be kept low [5]. For these requirements to be met, thorough optimization of growth parameters of different materials is essential. Fortunately, the versatility of the MBE technology allows testing of individual sub-components before integration to the multijunction architecture.

The growth process with MBE is highly automatized; the multijunction structures are grown according to recipes created by the operator. Typically, the growth process starts with a desorption of native oxides in high temperature after which a buffer layer is usually grown. The buffer layer ensures a smooth growth surface for the growth of following layers. Then the subcells and TJs are grown in sequence according to the recipe. Lastly, a contact layer with high doping level is grown. General guidelines for the growth parameters of GaAs-based materials were introduced earlier in this chapter.

MBE also offers some advantages over the rivaling MOCVD in the growth of MJSCs, especially MJSCs employing dilute nitrides. Firstly, low background doping concentrations in dilute nitrides, order of $10^{15}\,1/\mathrm{cm}^3$, can be achieved with PAMBE, making wide depletion regions plausible in dilute nitride cells [5]. In dilute nitrides grown with the MOCVD the background doping levels are often higher than $10^{16}\,1/\mathrm{cm}^3$, which yield to a maximum depletion widths of ~0.5 µm [85]. Secondly, with MBE superior TJs can be fabricated as it is more suited for abrupt material interfaces and doping profiles [81]. On the other hand, MOCVD offers higher growth rates which enables higher throughput of materials [32]. A novel technique for fabrication of MJSCs has been demonstrated in which the PAMBE and MOCVD processes are combined. In this technique the dilute nitride bottom cell is grown with PAMBE, after which the top junctions are

grown on top with MOCVD, thus, the best features of both methods are combined [107].

4.3 Processing of solar cells

After the epitaxial growth the SC structures need to be processed into devices. The main process steps typically include separating individual SCs from the wafer, the fabrication of metal contacts, and fabrication of the ARC. The processing consists of many smaller process steps that are done in sequence. The SC processing is typically done in clean room environment where the ambient conditions are highly controlled.

Solar cells can be processed by photolitographic process in which the front metal grid and a mesa-structure are defined with photolitographic steps. With the photolitographic process well defined metallization and device areas are obtained with good electrical isolation of the terminals. The photolitography process involves tens of processing steps, and is very time consuming. Detailed descriptions of the processes can be found elsewhere [83, 87].

For rapid testing of solar cell materials, a so called test process is commonly utilized at ORC. In the test process the contact metallization is done by electron beam evaporation, and the front contact grid is defined with a simple shadow mask. After metallization the contact layers not covered by the metals are typically removed with wet-etching. Lastly, the ARC coating can be deposited on the surface. Typically, a $TiO_2 - SiO_2$ ARC is employed which provides a 5 % average reflectivity in 400–1600 nm range [8]. The drawbacks of the test process are that the front grid definition is less sharp than with the photolitographic process [83], and the electrical isolation of the terminals inferior to the photolitographic process. Still, the test process has been found to be reliable, reproducible, and a fast way to obtain information about the solar cells [83].

5. MATERIALS AND METHODS

In this thesis 3J solar cell employing dilute nitride subcells were studied; for this thesis three samples were selected. The temperature dependent performance of the MJSCs was evaluated with IV measurements under simulated AM0 and AM1.5D illumination. A three band solar simulator was constructed for better simulation of the solar spectrum for MJSCs. The system was calibrated with single-junction cells calibrated by external quantum efficiency (EQE) measurements. In this chapter the 3J SC samples and characterization methods used for this thesis are introduced.

5.1 Triple-junction solar cell samples

The performances of three 3J solar cells comprising GaInP, GaAs and GaInNAsSb subcells were examined. The selected SC structures were nearly identical to allow comparison between the samples, but the GaInP subcell thicknesses and band gaps of GaInNAsSb subcells were different between the samples.

Samples S1 and S2 were grown on 625 µm thick 4" p-GaAs(100) substrates, and sample S3 was grown on a 350 µm thick 2" p-GaAs(100) substrate with PAMBE. The thicknesses of the GaInP top cells were different between the samples; the GaInP thickness increases with increasing sample number. The band gaps of the subcells, determined from the photoluminescence peak wavelengths [3], were 1.88 eV–1.89 eV, 1.42 eV–1.43 eV, and 0.97 eV–0.99 eV for GaInP, GaAs, and GaInNAsSb, respectively. The cells were processed with the test process into cells with total areas of 0.36 cm^2 and 0.16 cm^2, and the cells were coated with $TiO_2 - SiO_2$ ARCs. In table 5.1 some of the parameters of the studied 3J cell samples are presented.

The subcell materials were closely lattice matched to GaAs to allow the monolithic growth of the 3J structure. For the close lattice-matching an In concentration of ~2.7 times the N concentration was used in the GaInNAsSb subcells [3].

Table 5.1. *Properties of the 3J samples.*

Sample	Normalized thickness of GaInP subcell	$E_{g,GaInP}$ (eV)	$E_{g,GaAs}$ (eV)	$E_{g,GaInNAsSb}$ (eV)	Active area (cm^2)
S1	1.00	1.88	1.42	0.97	0.25
S2	1.45	1.89	1.42	0.97	0.25
S3	2.35	1.89	1.43	0.99	0.1175

5.2 Characterization methods

The SC samples were studied by using different methods. The main focus was on investigating the temperature and spectral dynamics of the 3J cells with LIV measurements. For these measurements an adjustable three band solar simulator setup was constructed. The results obtained with the three band simulator were compared to data recorded with an Oriel Xenon-simulator. The multiband spectrum calibration was compared to spectrum calibration of a new OAI TriSol simulator. Additional information about the SCs was obtained by external quantum efficiency (EQE) measurements. EQE measurements were also conducted for single-junction cells used for calibrating the multiband solar simulator. The characterization methods are introduced in this section.

5.2.1 Quantum efficiency measurements

The quantum efficiency describes the ability of a SC to generate and collect charge carriers when illuminated with photons at a particular wavelength. Quantum efficiency measurements are widely used for SC characterization as they offer valuable information about the current production of SCs as well as depth profiles of the cell when combined with computer simulations.

The quantum efficiency values can be divided to two types: external quantum efficiency (EQE) and internal quantum efficiency (IQE). EQE is defined as the ratio between charge carriers delivered to the terminals of the SC and the number of photons incident on the cell, and can be expressed as

$$EQE(\lambda) = \frac{N_e(\lambda)}{N_{ph,inc}(\lambda)} = \frac{\frac{I(\lambda)}{e}}{\frac{P(\lambda)}{E_{ph}(\lambda)}} = \frac{hcI(\lambda)}{\lambda eP(\lambda)}, \tag{5.1}$$

where N_e is the number generated electrons with wavelength λ , $N_{ph,inc}(\lambda)$ is the number of incident photons with wavelength λ, I is the cell current, e is the elementary charge, $P(\lambda)$ is the incident optical power of photons with wavelength λ and $E_{ph}(\lambda)$ is the energy of one photon with wavelength λ. The IQE is determined from the EQE and can be expressed as

$$IQE(\lambda) = \frac{N_e(\lambda)}{N_{ph,abs}(\lambda)} = \frac{EQE(\lambda)}{1 - R(\lambda) - T(\lambda)}, \tag{5.2}$$

where $N_{ph,abs}(\lambda)$ is the number of absorbed photons with wavelength λ, $R(\lambda)$ and $T(\lambda)$ are the wavelength dependent reflectance and transmission, respectively. The EQE value is dependent on the photon absorption and reflection as well as the internal collection efficiency of carriers. The IQE, on the other hand, effectively measures the internal collection efficiency.

The J_{sc} of the SC under certain illumination can be evaluated from the EQE information spectral irradiance data with expression

$$J_{sc} = e \int_{\lambda_1}^{\lambda_2} \lambda EQE(\lambda) F(\lambda) d\lambda, \tag{5.3}$$

where $F(\lambda)$ is the spectral irradiance at wavelength λ.

The EQE is determined from the spectral responsivity of the cell. The spectral responsivity (S) is a similar physical quantity as EQE but is instead measured in units of current produced per unit optical power [29]. The spectral responsivity can be converted to EQE through expression [29]:

$$EQE(\lambda) = \frac{hc}{e\lambda} S(\lambda). \tag{5.4}$$

The EQEs in this thesis were calculated from the spectral responsivities of the cells that were measured with an in-house built monochromator based measurement

setup. A schematic of the spectral responsivity measurement setup is illustrated in figure 5.1.

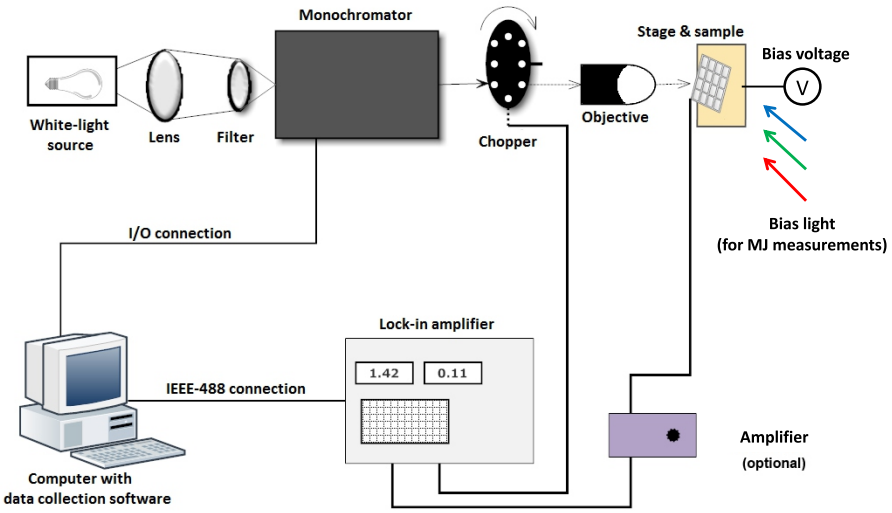

Figure 5.1. *Setup for measuring spectral responsivity.*

In the EQE setup broad-band light is produced with an Oriel 250 W Quartz Tungsten Halogen lamp, and the light is collimated with a lens to the input slit of a Digikrom DK240 grating monochromator. Between the lens and the input of the monochromator appropriate shortpass and longpass filters are used. The monochromator outputs a monochromatic beam which is transmitted through a chopper and collimating objective to the sample. The system is fitted with additional light sources for light biasing and with a voltage biasing unit. The cell response under the monochromatic illumination is measured with a Stanford Research Systems SR830 lock-in amplifier. The chopper provides the reference signal for the lock-in amplifier. Between the sample and the lock-in amplifier a Gigahertz Optik P-9202-4 current–voltage converter for amplifying the signal can be used. The system control and the recording of the spectral response is done with a computer. The response of the system is calibrated by NIST-calibrated Si and Ge reference detectors suitable for wavelength ranges of 350–1000 nm and 800–1600 nm, respectively.

The spectral response measurements are slightly different between single-junction and multijunction cells. The procedure for single-junction cells is more straightforward as light biasing is not required. For the single-junction cells the spectral responsivity measurement is started by measuring the response curves of the reference detectors in the desired wavelength ranges. The reference detectors are aligned in front of the beam so that the signal is maximized to ensure that the entire beam is incident on the detector. Then the reference responses are measured with same filter configurations that will be used for the SC measurements. After the reference measurement, the response of the SC is measured. Again the signal maximized so that the beam is incident on the active area of the cell. The spectral responsivity is typically measured under short-circuit conditions [29]. The operation point of the cell can be altered by applying bias voltage to the sample. After the SC measurements the responses of the reference detectors are typically measured again to confirm that the illumination has not changed during the measurements. With this type of setup, the temporal stability of the light source needs to be very good. In more sophisticated measurement setups, the reference detector is measured simultaneously with the cell. The spectral response of the samples can now be calculated from the response curves with

$$S(\lambda) = \frac{U(\lambda)}{U_{ref}(\lambda)} S_{ref}(\lambda), \tag{5.5}$$

where $U(\lambda)$ is the wavelength dependent voltage signal of the SC, $U_{ref}(\lambda)$ is the wavelength dependent voltage signal of the reference detector, and $\mathrm{S_{ref}}(\lambda)$ is the known spectral response of the reference detector at wavelength λ. The obtained spectral responsivities can be then substituted into equation 5.4 to obtain the EQE of the cells. In figure 5.2 exemplary EQE curves of GaInP and GaInNAs single-junction cells obtained with above method are presented.

The performance of the EQE measurements in the UV region are limited with this setup because the UV spectra produced by the halogen-lamp is insufficient for accurate measurements. Also, the NIST-calibrated Si detector is calibrated only to 350 nm which restricts the EQE measurements. This causes the short-circuit current densities of the cells to be inaccurate in the short wavelengths.

Measuring the spectral responsivities from the subcells of multijunction devices is not as simple as the measurements from single-junction devices. When measuring

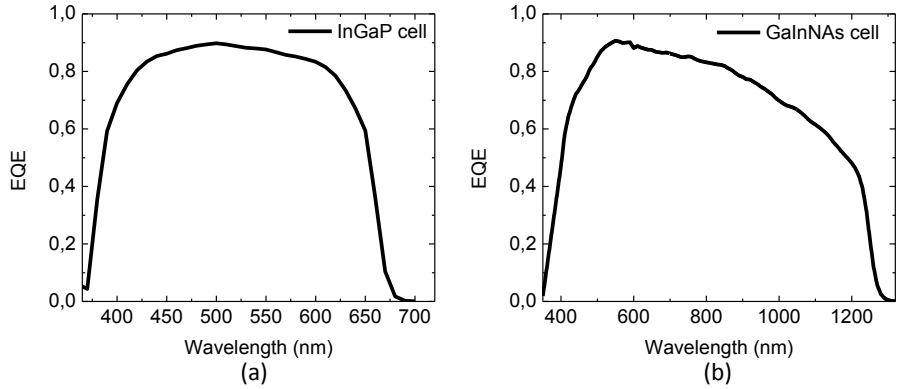

Figure 5.2. *EQEs of (a) GaInP and (b) GaInNAs single-junction solar cells.*

the EQE from a subcell of a MJSC, the subcell under measurement needs to be made the current limiting cell. This is done by illuminating the other subcells with relatively narrow-band light that is not absorbed by the subcell being measured. The light biasing is typically realized by light-emitting diodes or lasers. The junction that is being measured should be kept under short-circuit conditions which requires also adjusting the voltage bias. In practice, the successful voltage biasing is an iterative process because the the SC parameters are not typically well known prior to the measurement. [29] The EQEs from each subcell need to be measured individually. The reference detector responses are measured and the EQEs of the subcells are calculated in the same fashion as with the single-junction cells. The EQE measurements from MJSCs are not trivial and especially determination of EQE from the GaAs middle cell has been challenging.

5.2.2 Current-voltage measurements

The LIV measurements are used to define the performance of the SCs, and important parameters including maximum power P_{mp} can be determined from the IV behavior. In LIV measurements the cell is placed under illumination and the IV curve of the cell is recorded with a data acquisition system. For the illumination either simulated or natural light can be used. A typical four-point IV measurement setup is illustrated in figure 5.3.

The LIV measurements are made with respect to a reference spectral irradiance or the prevailing solar spectral irradiance. The irradiance is typically measured with a pyranometer for natural lighting (i.e. outdoor measurements) and with reference

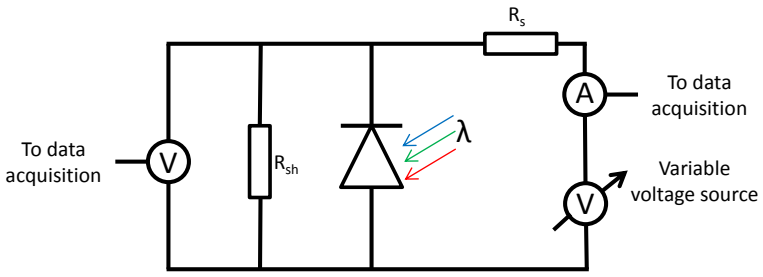

Figure 5.3. *Schematic of a typical IV measurement setup.*

cells for simulator-based measurements. [29] The LIV measurements for this thesis were conducted under simulated illumination and, therefore, natural lighting is not further discussed. In simulator-based measurements, the the simulator is typically adjusted so that the short-circuit current of the reference cell is equal to the short-circuit current calibrated with a reference spectrum. The reference cell is typically made of the same material as the device under testing.

When testing the LIV characteristics of a MJSC the simulator should be set such that each junction operates at the proper photocurrent. [29] Adjusting the typical single source solar simulators to satisfy this condition can be problematic as the source spectra varies from the reference spectrum. For this purpose, simulator systems consisting of multiple illumination sources can be used. The light from each source can be filtered and adjusted individually so that best possible spectral match is obtained.

Single source solar simulator

Previously, the simulator-based LIV characterization of SCs at ORC has been solely performed with a commercial Oriel Instruments 1000 W Xenon-simulator. The illumination from the simulator can be filtered with AM0 and AM1.5G air mass filters to simulate these spectral conditions. For the irradiance calibration a calibrated GaInP/GaAs tandem SC was typically used. The measurement setup with this system is similar to system illustrated in figure 5.3. In figure 5.4 the normalized irradiance spectra of the simulator with different air mass filters are illustrated alongside with reference spectra.

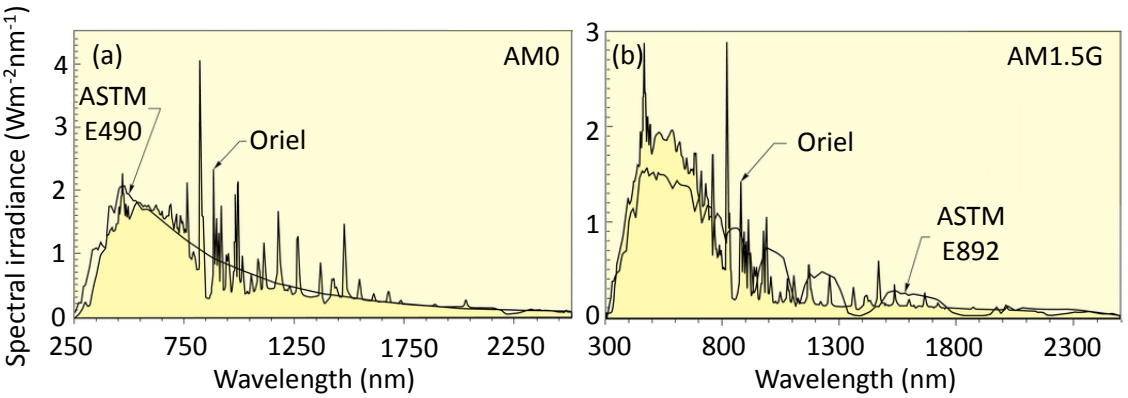

Figure 5.4. *Normalized spectral irradiances of (a) Oriel solar simulator with AM0 filter with ASTM E490 AM0 reference spectrum and (b) Oriel solar simulator with AM1.5G filter with ASTM E892 AM1.5G reference spectrum. [74, modified] The ASTM E892 reference spectrum is now replaced with ASTM G173 standard.*

From figure 5.4, we see the intense peaks produced by the Xenon lamp that cannot be sensibly filtered. We can also see that the simulator spectrum with AM0 filter relatively closely matches the ASTM E490 reference spectrum. In figure 5.4(b) the spectrum of Oriel simulator equipped with AM1.5G filter is compared to ASTM E892 AM1.5G standard spectra. The ASTM E892 AM1.5G standard spectra is nowadays replaced with ASTM G173 standard but it closely matches the spectrum defined in ASTM G173 standard; for the ASTM G173 AM1.5G spectrum the resolution was increased and minor modifications in the absorption modeling were made [43]. Nevertheless, from the figure 5.4(b) we can see that the simulator over produces illumination in the below 800 nm region and, conversely, above 800 nm under produces radiation compared to the reference spectrum. For multijunction solar cells this mismatch can cause large deviations in the currents of the junctions compared to currents produced under reference spectrum and, therefore, the simulated terrestrial measurements can be severely distorted.

Multisource solar simulator

To improve the LIV characterization of MJSCs a multisource solar simulator was built. The new system was built around the existing Oriel-simulator setup by adding two additional light sources to the system. With these light sources and filters, the spectrum was divided into three separate wavelength bands that could be individually adjusted. The main disadvantage of this setup is that the

additional light sources are not collinear with the simulator light and, therefore, are not incident to the sample in a normal angle. In this kind of setup, the substence angle of the supplemental beams should be less than 30° [23, 29]. With such angles a less than 2 % increase in the optical path length of photons can be expected. The stage was also modified so that the temperature of the stage could be altered. Resistive heating element for high temperature measurements and a water cooling block for low temperature measurements were installed under the stage. For the water cooling a Hailea HC-130A was used. The stage temperature was monitored with an AD590 temperature transducer. The multisource measurement setup is depicted in figure 5.5.

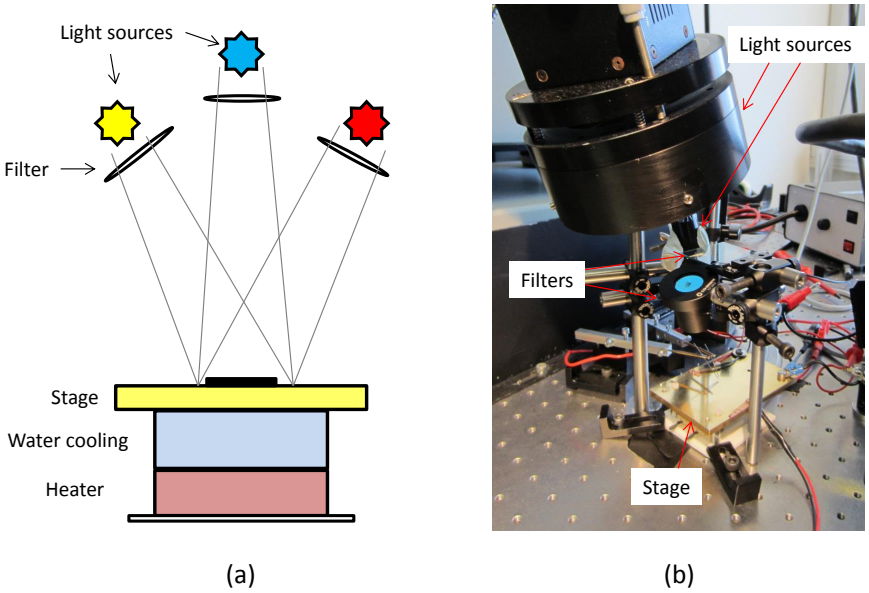

Figure 5.5. *(a) The schematic illustration and (b) a picture of the multisource solar simulator setup.*

The water cooling element was installed between the stage and the heating element so that the contact area between the cooling block and the stage was maximized. The better contact allowed the stage to be cooled more efficiently and, therefore, temperatures as low as 4℃ could be achieved. During the high temperature measurements, the water cooling was disabled to allow more efficient heat transfer between the heating element and the stage.

The short-wavelength illumination for the GaInP subcell was produced with the Oriel-simulator. For the GaAs and GaInNAsSb subcells halogen light sources were used. The beam diameter of the halogen used for illuminating the bottom cell is only

about 2 cm, which restricts the cell size to $1 \times 1\,\mathrm{cm}^2$ for accurate measurements. The light sources were positioned so that the sufficiently small substence angles were realized (see table 5.2). For the light filtering Oriel Instruments airmass filters, Thorlabs dielectric shortpass (SP) and longpass filters (LP) and Thorlabs glass filters were used. Different filter combinations were used for the AM0 and AM1.5D spectral conditions. In table 5.2 the different simulator configurations are presented.

Table 5.2. *Simulator light source configurations for AM0 and AM1.5D spectral conditions. Airmass, dielectric and glass filters are denoted with AM, DE and G, respectively.*

	Source type	Beam angle	AM0 filters	AM1.5D filters
Source 1	Xenon	0°	AM0 (AM)	AM1.5G (AM)
			FGB37S (G)	650 nm SP (DE)
			FGS900S (G)	FGS900S (G)
Source 2	Halogen	20°	600 nm LP (DE)	650 nm LP (DE)
			900 nm SP (DE)	900 nm SP (DE)
Source 3	Halogen	26°	900 nm LP (DE)	900 nm LP (DE)

The combined filter transmissions (without airmass filters) of the different bands in the AM0 and AM1.5D configurations are illustrated in figure 5.6 with reference solar spectra.

Ideally the spectral bands should fulfill three requirements: (i) the band edges of the spectral bands should be close to the absorption edges of the subcells, which allows the intensity of spectral bands to be adjusted independently for each subcell; (ii) the spectral bands should be sharply defined to mimic the sharp absorption edges of the subcells and to minimize the overlapping between the spectral bands; and (iii) the spectral bands should cover the entire absorption bands of the subcells to take into account the variations in the EQEs of the subcells at different wavelengths but, also, to allow temperature dependent characterization of MJSCs. But due to the limited selection and the non-ideal performances of the filters, compromises from these requirements could not be avoided.

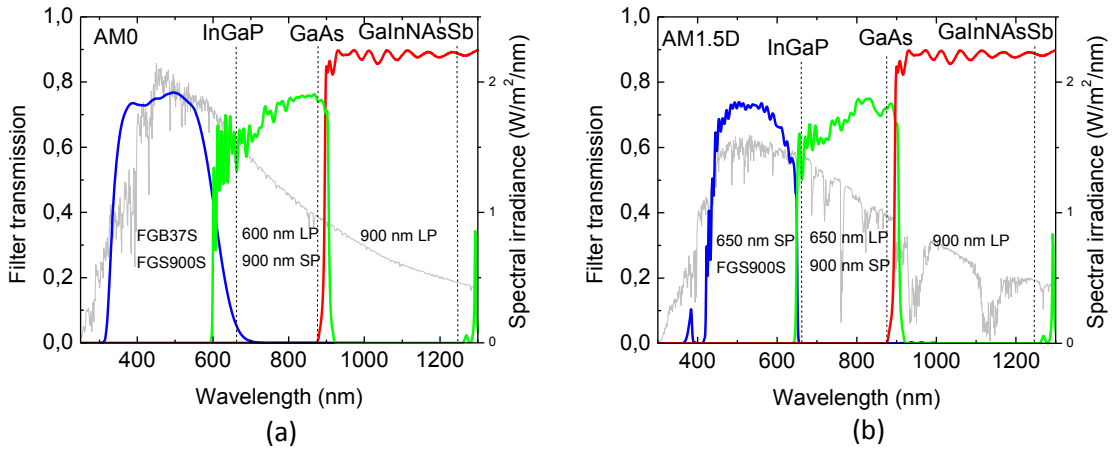

Figure 5.6. *The (a) filter transmissions of AM0 configuration with the ASTM E490 AM0 reference spectrum and (b) filter transmissions of AM1.5D configuration with the ASTM G173 AM1.5D reference spectrum (normalized to 1000 W/m^2). The absorption edges of subcells are indicated with dashed lines.*

The transition between the middle and long spectral bands was realized with 900 nm SP and LP filters in both filter configurations. From the figure 5.6 we see that with this filter combination an almost step-wise band transition is achieved near the absorption edge of GaAs with only minimal band overlapping. The 900 nm LP filter has also some transmission around 1300 nm, as seen from figure 5.6; these transmitted wavelengths are above the absorption edges of the dilute nitride subcells, and don't have an effect on the cell operation.

The band definition between the short and middle spectral bands, on the other hand, was not as simple. When selecting the filters for this transition we had to weigh between the sharpness of the spectral band definition and the UV content of the band. The AM0 reference spectrum has more UV content than the AM1.5D reference spectrum and, therefore, in the AM0 configuration we wanted to include more of the UV region produced by the Xenon-simulator. The dielectric SP filters in our selection effectively cut off wavelengths below 400 nm, which is why the short band filtering in AM0 configuration was decided to be realized with a combination of glass filters. From the figure 5.6(a) we may see that the cut-off wavelength of this filter combination is around 300 nm which allows more UV light to be passed to the top junction, but with these filters the sharp band definition between the short and middle spectral bands was lost. Because the transmission of the glass filters gradually decreases in the range of 550–700 nm, the short-wavelength filter of the middle band had to be selected so that no significant dip would occur in the

simulated spectrum and, therefore, a 600 nm SP filter was chosen. The 600 nm SP filter causes the short and middle spectral bands to be coupled, which can be seen from the figure 5.6(a). The band coupling is the disadvantage of this configuration. Due to the lower UV content of the AM1.5D spectrum the sharp band definition was preferred in the AM1.5D configuration, and the short and middle spectral bands were separated with 650 nm filters. These filters produce a sharp transition between the bands very close to the absorption edge of GaInP, as seen from figure 5.6(b). The sharply defined spectral bands, with edges near the absorption edges of the subcells, allow a relatively easy adjustment of the intensities of the bands in this configuration. This can also be used for evaluating the currents of individual subcells. It should be noted that the absorption dips of the AM1.5D spectrum cannot be reasonably simulated with filters resulting in a spectral mismatch between the simulator and reference spectra.

Multisource simulator calibration

The multisource simulator was calibrated using EQE-calibrated single-junction GaInP, GaAs, and GaInNAsSb SCs. The EQEs of the calibration cells were measured with the in-house built measurement setup described in the section 5.2.1. The EQE spectra measured from the calibration cells are presented in figure 5.7.

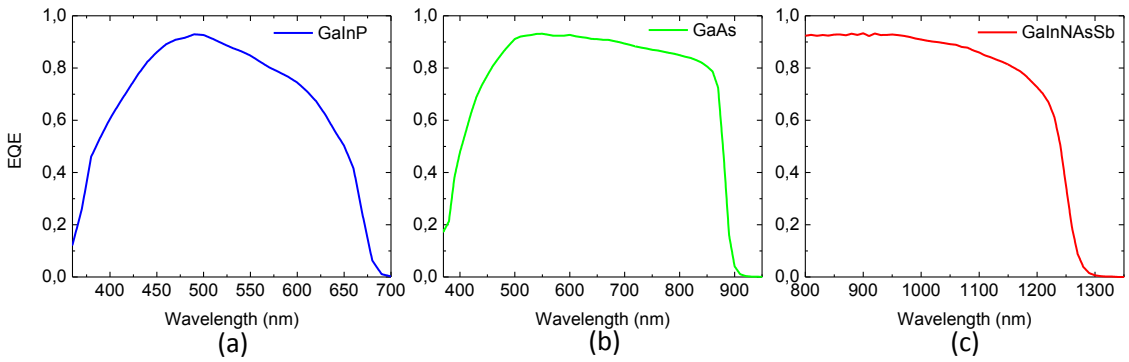

Figure 5.7. *The EQE spectra of (a) GaInP, (b) GaAs, and (c) GaInNAsSb calibration cells.*

The short-circuit current densities generated by the calibration cells under reference spectra were calculated from equation 5.3. The integration limits were chosen to correspond to the spectral bands of the multisource simulator. For the calculation of calibration currents from J_{sc} values, the active areas of the

calibration cells were determined. For this the calibration cells were photographed by an optical microscope. Due to the limitations of the microscope, multiple separate pictures were taken that were later merged into one. The dimensions of the cells were measured by a Sony measuring tool connected to the optical stage of the microscope. The active areas were then obtained from the merged pictures by using ImageJ image processing software. The measured cell dimensions were used to set the scale in the software. To increase the accuracy of calibration, the shading caused by the probes of the LIV measurement system was taken into account. This was done by measuring the pin diameters and angles, which were then used to evaluate the pin shading on each of the cells. The calibration currents were then calculated by multiplying the calculated J_{sc} values with the measured active areas. The active areas, integrated short-circuit current densities and calibration current for the calibration cells are presented in table 5.3.

Table 5.3. *Properties and calibration data of the single-junction calibration cells. The integration limits used for the calculations are listed below the J_{sc} values.*

Cell	Active area* (cm^2)	$J_{sc,AM0}$ (mA/cm^2)	$J_{sc,AM1.5D^{**}}$ (mA/cm^2)	$I_{sc,AM0}$ (mA)	$I_{sc,AM1.5D^{**}}$ (mA)
GaInP	0.2466	16.64 (300–700 nm)	12.10 (300–650 nm)	4.10	2.98
GaAs	0.2732	18.93 (600–900 nm)	13.90 (650–900 nm)	5.17	3.80
GaInNAsSb	0.2725	16.64 (900–1300 nm)	13.40 (900–1300 nm)	4.53	3.65

*Probe pin shading taken into account.
**AM1.5D spectrum normalized to 1000 W/m^2.

The spectral bands of the simulator were calibrated by individually measuring the short-circuit currents of the cells, and by adjusting the light sources so that the measured values would concur with the calculated values presented in the table 5.3. The short-circuit conditions were realized by setting the bias voltage so that the measured sample voltage was 0 V. The stage temperature was always set to 25℃ during the system calibration. The calibration procedures for AM0 and AM1.5D conditions were slightly different due to the different filter setups of the configurations. In the AM0 configuration the following procedure was used. First,

the halogen for the middle spectral band was adjusted with the GaAs calibration cell. Next, the short-wavelength band was calibrated with the GaInP cell. Due to the overlapping of the short and middle spectral bands, a large part of the middle band illumination is absorbed by the GaInP top cell (see figure 5.6) also resulting in underbiasing of the GaAs subcell. The underbiasing is not a severe problem for MJSCs that are not close to being current-limited by the GaAs subcell. Because of the band overlap, the GaInP calibration cell was simultaneously illuminated with the Xenon and the middle band halogen when the Xenon intensity was adjusted. The short-wavelength band also extends to the middle band thus increasing the intensity in the 600–700 nm range, but only a fraction of this light is transmitted to GaAs in a 3J. The transmission of light from the top cell to the middle cell becomes more significant when the top cell thickness is reduced. If we assume that the calibration of the middle band is correct in the absorption range of GaAs in a 3J, the increase in the middle cell currents for the studied 3J cells is estimated to be less than 1 %. Additionally, the illumination transmitted by the top cell from the short-wavelength band compensates at least for some of the underbias of the middle subcell caused by the band overlapping. Finally, the halogen for the long-wavelength band illumination was calibrated with the GaInNAsSb cell.

In the AM1.5D configuration the bands could be adjusted separately as the band overlapping was very minimal. The AM1.5D calibration was typically performed in sequence: (i) middle band calibration with the GaAs cell, (ii) short band calibration with the GaInP cell, and (iii) long band with the GaInNAsSb cell. At each step of the AM1.5D calibration procedure the calibration cell was only illuminated with the light source that was being adjusted.

One important parameter of simulator performance is the temporal stability of the illumination. With the multisource simulator the temporal stability was determined to be at good level. When the calibration cells were remeasured after several hours of cell measurements, the calibration currents were determined to be within 2 % from the target values reported in table 5.3.

The multisource simulator had already been used extensively for SC characterizations when a new OAI TriSol simulator arrived at ORC. During the commissioning of the new TriSol simulator some verification for the multisource calibration of the AM1.5D configuration was obtained. A set of single-junction GaInNAsSb cells, with different junction thicknesses, were earlier measured with

the multisource simulator under AM1.5D illumination normalized to 900 W/m^2. The same samples were measured with the OAI simulator as part of the initial testing of the system. The OAI simulator was set to AM1.5D normalized to 1000 W/m^2. The spectral match between the OAI simulator spectrum and reference spectrum is calculated to be 98 % at AM1.5D in the spectral range of 300–1300 nm. The calibration of the OAI simulator was tested with a dual-junction (2J) SC calibrated at Fraunhofer ISE. The measured I_{sc} of the 2J cell deviated from the value reported by Fraunhofer by less than 2 %. The J_{sc} values obtained with the multisource simulator were normalized to correspond to AM1.5D illumination with irradiance of 1000 W/m^2, and then compared to the J_{sc} values measured with the OAI simulator. The J_{sc} were found to be in extremely good agreement as less than 1 % deviations between the measured currents were observed.

There are many sources of uncertainty for the calibration of the multisource system that accumulate and affect the total calibration accuracy of the system. But based on the comparison between the multisource simulator and the OAI TriSol simulator, the accuracy of spectral calibration of the multisource system can realistically be estimated be ± 5 % at AM1.5D.

6. RESULTS AND DISCUSSION

In this chapter the results for the 3J SC characterization are compiled and the analyzed. The emphasis of the cell characterization was on the LIV measurements of the selected 3J samples, from which the effects of illumination spectra and temperature on the LIV characteristics were studied. Majority of the LIV characterization was done with the multisource solar simulator but additional characterization was done with the Xenon-simulator. The LIV characterization of the cells is covered in the first section of this chapter. In the second section, the EQE properties of the best performing 3J cell are considered.

6.1 Current-voltage analysis

Extensive LIV characterizations were carried out for the 3J cells introduced in the previous chapter. In this section the LIV characterization of the cells is discussed. First, the room temperature LIV characteristics of the cells are reviewed, and the cell performances at AM0 and AM1.5D conditions are compared. The main focus is in the multisource simulator measurements, but the results are compared with the Xenon-simulator LIV data. Secondly, the current balancing between the 3J subcells is investigated at AM1.5D. Thirdly, the temperature dynamics of the 3J cells under AM0 and AM1.5D spectra are considered, and the temperature coefficients for the performance parameters are evaluated from the temperature dependent results.

Room temperature characterization

The SC performance is typically reported at standard temperature of 25℃ [29], which is why the characterization of the 3J cells was started by measuring their LIV curves with the multisource simulator at 25℃. The measurements were performed with AM0 (1366.1 W/m^2) and AM1.5D (normalized to 1000 W/m^2) spectra. The results from the multisource LIV measurements were compared with the results from

the Xenon-simulator measurements at AM0 and AM1.5G. The LIV curves of the cells are plotted in figure 6.1. In table 6.1, the multisource LIV characteristics of the cells at 25℃ and the measured differences in J_{sc} and η_{active} values between the multisource and Oriel simulators, are summarized.

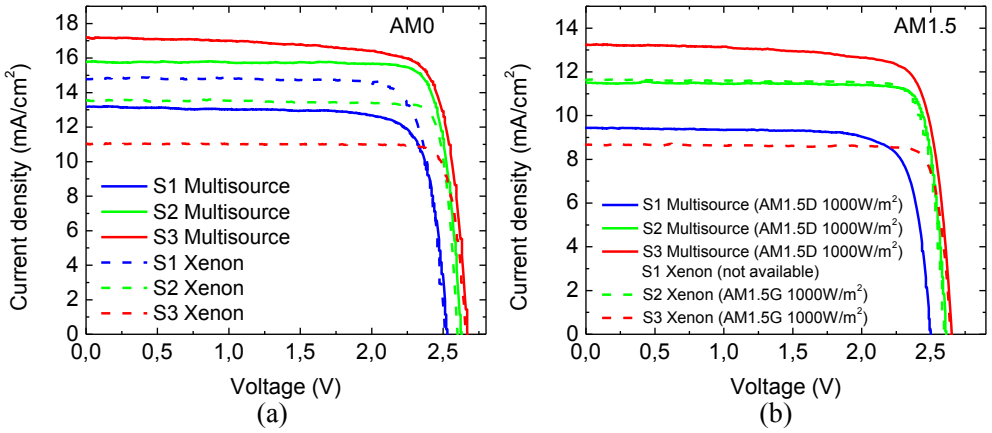

Figure 6.1. *The LIV curves of the 3J cells at (a) AM0 and (b) AM1.5 illumination. The solid and dashed lines represent the curves measured with illumination from the multisource simulator and the Xenon-simulator, respectively.*

Table 6.1. *LIV characteristics of the 3J cells under AM0 and AM1.5D (1000 W/m^2) illumination at 25℃ with the multisource simulator. In addition, measurement error in J_{sc} and η_{active} with Oriel simulator are presented.*

Cell	Spectrum	J_{sc} (mA/cm^2)	V_{oc} (V)	FF	P_{mp} (mW)	η_{active} (%)	ΔJ^*_{sc} (mA/cm^2)	$\Delta\eta^*_{active}$ (%)
S1	AM0	13.2	2.53	0.804	6.70	19.6	+1.6	+2.8
	AM1.5D	9.44	2.49	0.795	4.69	18.8	n.a.	n.a.
S2	AM0	15.8	2.63	0.854	8.84	25.9	-2.2	-3.1
	AM1.5D	11.5	2.61	0.867	6.51	26.1	+0.1	-0.1
S3	AM0	17.2	2.67	0.797	4.29	26.7	-6.1	-7.8
	AM1.5D	13.2	2.65	0.802	3.30	28.1	-4.6	-8.0

*Value measured with Oriel simulator compared to value measured with multisource simulator.

From the figure 6.1 and the table 6.1 we can see that the J_{sc} values measured with the multisource simulator increase when the GaInP subcell thickness is increased.

For J_{sc} values measured with the Xenon-simulator an opposite trend can be observed. In figure 6.2 the J_{sc} values of the cells are plotted against the relative GaInP subcell thicknesses; the multisource data is also fitted with exponential curves.

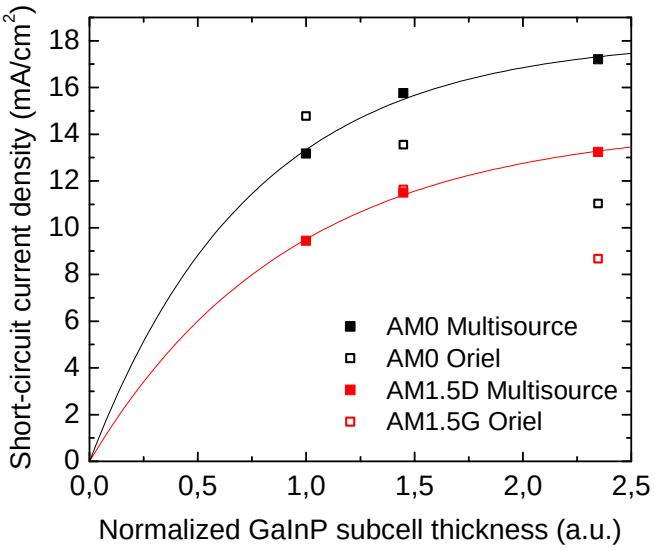

Figure 6.2. *The J_{sc} values of the 3J cells at AM0 and AM1.5D as function of the relative thicknesses of the GaInP subcells. The data points are fitted with exponential curves.*

The increase in the multisource J_{sc} values is a consequence of the increased light absorption and collection of carriers by the GaInP subcells. The light absorption in material follows the exponential Beer–Lambert law and, thus, when the GaInP subcell is made thicker, less light is transmitted through the top cell, and the more current is generated by the GaInP junction. The highest short-circuit current densities were observed for the cell S3; the cell generated 17.2 mA/cm^2 and 13.2 mA/cm^2 at AM0 and AM1.5D, respectively. Because the current of the MJSC is limited by the smallest current of the subcells, the good exponential fits imply that the GaInP limits the current in all the 3J cells at 25℃.

From the figure 6.2 we may clearly notice the discrepancies between the LIV-curves measured with the multisource simulator and the Oriel Xenon-simulator. The most significant difference is observed in the measured values of J_{sc} which, consequently, causes also deviations in the conversion efficiencies. Cell S1, with the thinnest top cell, overproduces current with the Xenon-simulator compared to the multisource simulator measurement. Cells S2

and S3, on the other hand, undergenerate current with the Xenon, and the deviation between the current values increases with the thickness of the top cell. The discrepancies between the values are caused by the combination of the spectral mismatch of the Xenon-simulator and the GaInP subcell thicknesses. As mentioned in section 5.2.2, the Xenon-simulator overproduces illumination in the below 800 nm region and, conversely, underproduces illumination in the above 800 nm region. In the case of thin GaInP top cells (like in S1), the high UV content of the Xenon causes the GaInP top cell to overproduce current but, still, a large fraction of the short-wavelength light is passed to the underlying GaAs cell causing the 3J cell to be limited by GaInP. When the GaInP cell is thicker, the fraction of the short-wavelength light transmitted to the underlying GaAs cell decreases, and due to the low the spectral content of the Xenon at wavelengths above 800 nm, the 3J cell may become falsely limited by the GaAs cell (like in S2 and S3). This causes the current to be underestimated in the worst case by 36 % (see table 6.1). The deviations in the current also cause major differences in the efficiency values; from the table 6.1 we see that with thick top cell the cell efficiency is underestimated by 8 percentage points. Based on these observations it's justified to say that the Xenon-simulator by itself is not sufficient for definitive LIV characterization of MJSCs.

When examining the table 6.1 we can see that the highest V_{oc} values were demonstrated by the cell S3 with the multisource simulator. The cell S1, on the other hand, demonstrated the lowest V_{oc}. The difference in V_{oc} values between the samples S2 and S3 can be explained with the higher E_g of the GaInNAsSb subcell in S3. As stated in section 3.2 the V_{oc} of cell decreases with lower E_g. The E_g of the bottom cells in S1 and S2 were identical but still, the V_{oc} of S1 was smaller compared to S2. This indicates that the recombination losses for S1 are higher than for S2 most probably in the dilute nitride subcell. If we compare the V_{oc} values of the 3J cells under different spectra, we see that the V_{oc}'s are higher under AM0 illumination. The slightly higher V_{oc} values are caused by the increased current generation at AM0 as could be expected from equation 3.3.

From the table 6.1 we may also see that there is variation in the FFs of the 3J cells. The highest FF was observed for S2, and for the cells S1 and S3 the values were nearly identical. If we take a look on the figure 6.1 we can see that the shape of the LIV curves of S3 are different between multisource and Xenon-simulator measurements. From the Oriel measurements a significantly higher FF, 0.877, was observed. This

indicates that the cell S3 has sustained some damage between the measurements which has increased the shunt resistance component and, consequently, lowered the FF.

With the multisource simulator, the best efficiencies, 26.7 % and 28.1 % at AM0 and AM1.5D, respectively, were demonstrated by the cell S3. The conversion efficiency is lower in the cells S1 and S2 mainly due to the reduced current generation by the GaInP top cells. The efficiency of S1 is further hindered by the low V_{oc}. The conversion efficiencies of S3, on the other hand, are reduced by the low FF that is probably caused by damage to the cell. If we neglect the changes in FF caused by improved current-matching, and assume that the FF of the cell S3 would have been as high as it was in Xenon-simulator measurements, efficiencies of 29.5 % and 30.9 % could have been realistically expected at AM0 and AM1.5D, respectively.

The current balancing between the junctions of the 3J cells can also be studied with the multisource simulator. For these measurements the system was initially calibrated normally, after which the intensity of the spectral bands were individually adjusted, and the J_{sc} values were determined with different intensities. Similar current balancing measurements of multijunction solar cells have been previously published, but in these measurements the additional light biasing of subcells has been realized with additional narrow band light sources [36, 37, 101]. The J_{sc} data points were then plotted as function of relative illumination power of the bands. The illumination intensity of the short-wavelength band was measured with a photodetector attached to the Xenon-simulator that outputs a voltage directly proportional to the illumination intensity. For the middle band the power was read from the display of the lamp power source. For the long-wavelength band, the intensity could not be easily determined and, therefore, its intensity could only be increased in the end of the testing sequences. The stage temperature was always set to 25℃ during these tests. The current balancing tests for the cells were conducted only at AM1.5D illumination as the power source of the Xenon-simulator broke before the AM0 current balancing measurements.

First, the current balancing of the GaInP subcells was studied. This was done by adjusting the intensity of the short-wavelength band (Xenon) while maintaining the other bands at normal AM1.5D calibration. The J_{sc} values were measured with many different intensities and plotted as function of the illumination intensity of the short-wavelength band. If the cell under testing is current limited by the top

cell, a linear increase in the J_{sc} could be observed when the intensity of the short-wavelength band is increased, until a sufficient intensity is reached and the top cell is not anymore limiting the current. In an ideal case the current density would not be further increased but, in reality, some light is transmitted through the top cell to the lower cells, and current density is still increased. For this reason, the plots were observed for changes in the slopes. At the point where the slope changes, current matching between the top cell and the limiting cell has been established. But due to the transmission of light, the current of the limiting cell can not be read from that point, as the limiting current also changes when the illumination intensity is adjusted. The spectrum of the Xenon was determined not to change significantly when the intensity is adjusted and, therefore, the change in J_{sc} values can be fitted with linear fits. By linear fitting the two regions with different slopes, the current of the limiting cell can be read from the point where the extrapolated linear fit intercepts with the normal calibration line. The obtained plots are presented in figure 6.3.

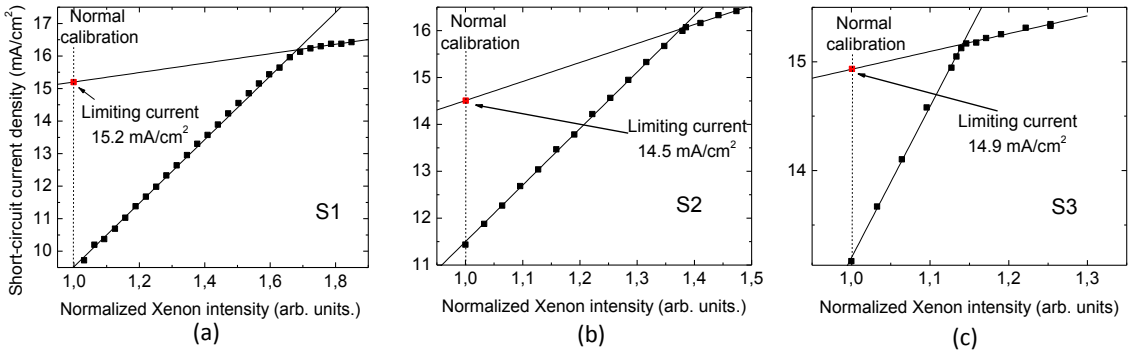

Figure 6.3. *The J_{sc} values of (a) S1, (b) S2, and (c) S3 as function of short-wavelength band intensity. The other bands were kept at normal AM1.5D calibration.*

From the figure 6.3 we can see that the J_{sc} values are increased with the intensity of the short-wavelength band until at some point the slopes change. This means that at the normal calibration the 3J cells are current-limited by the GaInP cells. From the linear fits we can estimate the J_{sc}'s of the cells that start to limit the performance after the top cell. To test whether the limiting current corresponds to the current of the GaAs subcell or the GaInNAsSb subcell, the intensity of the short-wavelength band was adjusted such that the GaInP junction wasn't limiting the current, and then the long-wavelength band was significantly increased. If the 3J cell would be limited by the GaInNAsSb subcell, a significant increase in the 3J cell current would be observed, but no increase in the currents could be observed.

This implies that the limiting currents presented in figure 6.3 correspond to the currents of the GaAs subcells.

Next the currents of the GaInNAsSb subcells were investigated. For this the intensity of the short-wavelength band was first set such that the intensity was roughly doubled compared to the normal calibration. By this it was ensured that the GaInP top cell would not become the limiting subcell at any point. It should be noted that the current of the GaAs cell is also increased as the short-wavelength intensity is adjusted due to the transmission of the top cell. The intensity of the middle spectral band was then altered, and the J_{sc} values were measured. The values were plotted as function of the middle band illumination intensity, and the plots were observed again for changes in the slopes. The spectrum of the middle band halogen was determined not to change significantly when the power is adjusted in the power region where the current balancing analysis is done and, therefore, the change in J_{sc} values can be fitted with linear fits. The J_{sc} of the GaInNAsSb subcells can be approximated from the linear fits with respect to to the normal calibration line. In figure 6.4 the plots acquired with the above method are illustrated.

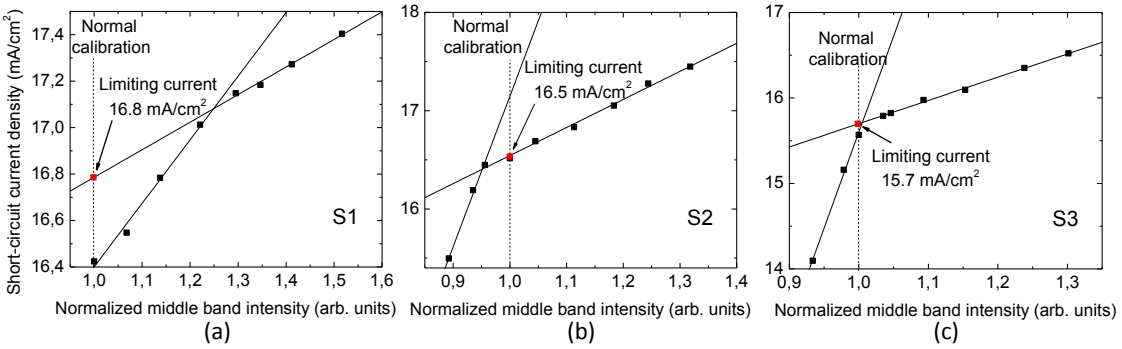

Figure 6.4. *The J_{sc} values of (a) S1, (b) S2, and (c) S3 as function of middle band intensity. The short-wavelength band was set to high intensity whereas the long-wavelength band was kept at normal AM1.5D calibration.*

The increased short-wavelength illumination of the top cell causes the current of GaAs subcell to become arbitrary as some of the short-wavelength light is passed to the middle cell. Consequently, the change in slope can be found on either side of the normal calibration line. For S1 and S3 the slope change can be observed on the higher intensity side compared to the normal middle band calibration line and, therefore, the current of the bottom cell can be determined similarly as earlier. Conversely, from the figure 6.4(b) we see that for S2 the slope changes on the

lower intensity side. In this case the GaAs cell current has been increased such that the bottom cell limits the operation at the normal middle band calibration. When the middle band intensity is decreased sufficiently the GaAs cell begins to limit the current which can be observed as a sudden change in the slope. Therefore, by assuming that the increased Xenon intensity does not affect the bottom cell, the current of the bottom cell can be read from the measured current at the normal middle band calibration. The short-circuit current densities of individual subcells of the 3J samples are compiled in table 6.2. The measurement error for the J_{sc} values is estimated from 95 % confidence intervals of the linear fits.

Table 6.2. *Short-circuit current densities of the subcells in 3J samples under AM1.5D illumination.*

Cell	$J_{sc,GaInP}$ mA/cm^2	$J_{sc,GaAs}$ mA/cm^2	$J_{sc,GaInNAsSb}$ mA/cm^2
S1	9.44	15.2 ± 0.6	16.8 ± 0.1
S2	11.5	14.5 ± 0.7	16.5 ± 0.1
S3	13.2	14.9 ± 0.1	15.7 ± 0.1

From the table 6.2 we see that the subcells of S3 are the closest to being current-matched at AM1.5D. The current balances of all the 3J cells show similar trends; the cells are current-limited by the GaInP top cells, while the GaAs subcells produce the second highest currents, and the GaInNAsSb bottom cells generate the highest currents. As observed earlier, the short-circuit current densities of GaInP subcells are higher the thicker the GaInP top cell is. The effect of top cell thickness can also be seen on the J_{sc} values of the GaAs junctions for samples S1 and S2; the current of GaAs subcell is reduced as the GaInP thickness is increased. This is a direct consequence of the transmissions because as the GaInP cell is fabricated thin a larger fraction of short-wavelength illumination is passed to the middle cell. The current of GaAs junction in sample S3 does not fit to this trend as it produces a higher current than S2 even though the GaInP subcell is significantly thicker in S3. This could be explained with increased luminescent coupling between GaInP and GaAs subcells as the top cell is thicker in S3 [37], or with a higher IQE of the GaAs middle cell in S3. The GaInNAsSb bottom cells in S1 and S2 generate nearly identical currents which is logical as the E_g values of these cells are similar. The bottom cell of S3, on the other hand, generates a lower current which can be

explained with the higher E_g of GaInNAsSb in S3 (see table 5.1). By improving the current-matching between the GaInP and GaAs subcells the one-sun efficiency of the cells at AM1.5D could be increased; for S3 approximately a 2.5 percentage point increase in the conversion efficiency could be achieved if the top and middle cells were matched at 14.5 mA/cm^2. The improvements in current-matching could be realized by fabricating thicker GaInP subcells and by increasing the spectral response of the GaInP subcell.

Temperature dependent characterization

The effect of temperature on the performance of the 3J cells was investigated by measuring the LIV curves of the cells at different stage temperatures with the multisource setup. The temperature dependent LIV measurements were performed in temperature range of 5–90℃ with intervals of 5℃ at AM0 and AM1.5D spectra. For these measurements the multisource simulator was first calibrated at 25℃ with the procedure described in section 5.2.2. During the measurements the stage temperature was always kept within ±1℃ from the target temperature. In figure 6.5 exemplary LIV curves measured from sample S3 at different temperatures are presented.

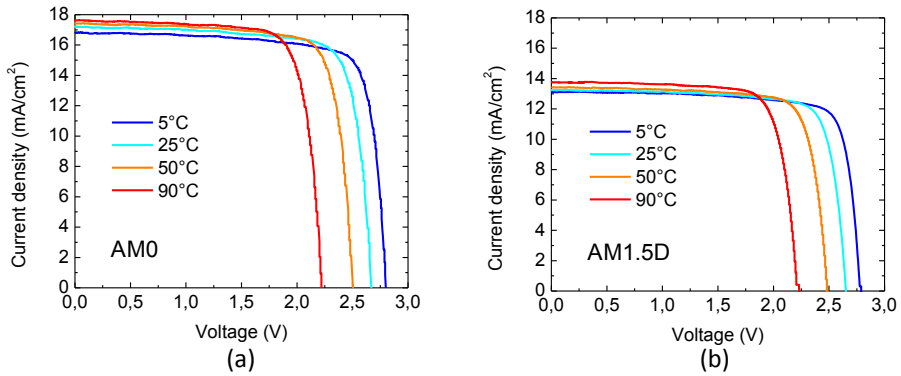

Figure 6.5. *LIV curves measured from sample S3 at different stage temperatures at (a) AM0 and (b) AM1.5D illuminations.*

From the curves in figure 6.5 we may clearly see the effect of increasing temperature on the cell operation, as the current slightly increases and the voltage drops. As mentioned in the chapter 3, increase in the current is caused by the red-shift of the absorption edges of the junctions. The drop in the voltage is caused by the increased dark saturation current which is a result of increased intrinsic carrier concentrations

at higher temperatures. The same effects can be also clearly observed in the LIV data measured from the other two 3J cells. From the temperature dependent LIV curves the values for J_{sc}, V_{oc}, FF, and η were extracted. These values were plotted as function of temperature from which the temperature coefficients (TC) for these parameters could be determined with linear regression analysis.

Temperature dependencies under AM0 illumination

First, the temperature dependencies under AM0 spectrum are discussed. The measured temperature dependencies of the performance parameters for the 3J cells at AM0 are illustrated in figure 6.6. The power source of the Xenon-simulator broke during the temperature dependent AM0 measurements of cell S1 and, therefore, data for S1 could be only obtained up to 35℃.

The J_{sc} values are observed to increase with temperature. As mentioned, the increase in current is caused by the temperature induced shifting of the E_g in the cell materials. The temperature induced changes in J_{sc} values are observed closely linear over the whole temperature range, with the exception of cell S3 for which a sudden change in the J_{sc} slope can be observed at around 20℃. The change in the slope can be explained with a crossover in the current balance between the GaInP and GaAs subcells. Under AM1.5D illumination at 25℃ the cell S3 was analyzed to be current-limited by the GaInP top cell (see table 6.2), but that the GaInP and GaAs subcells in S3 were closest to being current-matched. Now, because the short-wavelength content is greater in the AM0 spectrum compared to AM1.5D spectrum, the current mismatch between the GaInP and GaAs subcells of S3 is, supposedly, narrowed at AM0. Still, at temperatures above 20℃ the GaInP limits the 3J current. The TC of E_g for GaAs is larger than for GaInP [100], which causes the absorption band of the GaAs subcell to be narrowed when temperature is lowered, leading to a decrease in the J_{sc} of GaAs. Around 20℃ the absorption edges have moved such that the currents of the subcells are closely matched, but when the temperature is lowered below 20℃ the GaAs junction begins to limit the current. This current crossover is not observed for samples S1 and S2 due to the GaInP top cell thicknesses of these samples. In S1 and S2 the GaInP top cells are thinner and, therefore, more short-wavelength light is transmitted to the GaAs cell, which increases the current of GaAs. Owing to the higher GaAs subcell

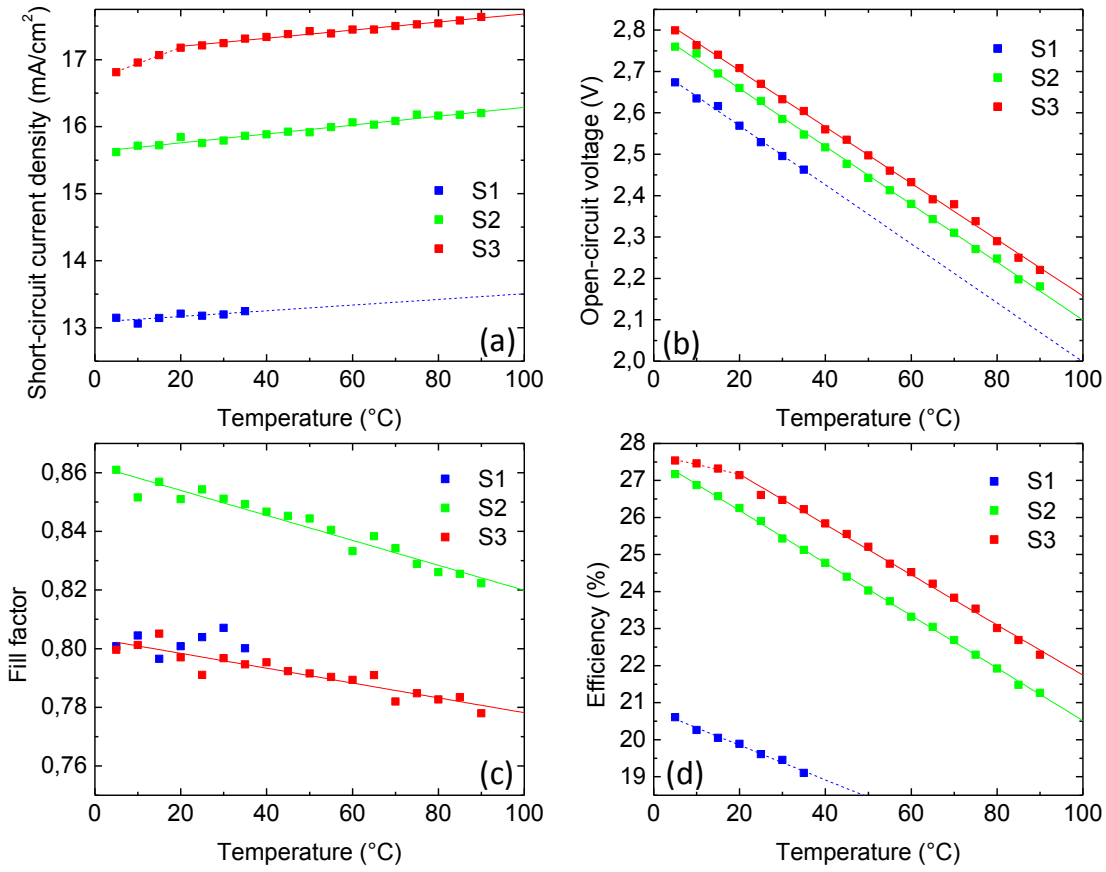

Figure 6.6. *The temperature dependencies of (a) J_{sc}, (b) V_{oc}, (c) FF and, (d) η for the 3J cells under AM0 illumination. The data for S1 is incomplete due to equipment failure.*

current, the cell operation of S1 and S2 is limited by the GaInP cell over the entire observed temperature range, and a close to linear increase in J_{sc} is observed.

The TCs for J_{sc} were obtained from the slopes of the linear regression fits for the data. The linear regressions yielded TCs ranging 4.2–6.6 µA/cm^2/℃ in the GaInP limited regions. The lowest TC was determined for S1, but the number of temperature data points was insufficient for good linear regression analysis which renders this result inaccurate. On the other hand, a relatively high J_{sc} slope of 24 µA/cm^2/℃ was determined for S3 at below 20℃. Even though the temperature dependence of E_g is more rapid for GaAs, and a steeper slope for J_{sc} is expected at GaAs limited region, the attained TC is abnormal. The dominating reason is supposedly in the non-ideal shape of the AM0 spectrum, especially in the spectral band of the GaAs subcell. The combination of filters and illumination sources used

for AM0 configuration are suspected to cause a dip in the photon density in the vicinity of the GaInP absorption edge which could cause a radical imbalance between the relative amounts of photons gained by GaAs from the blue-shift of the absorption edge of GaInP and photons lost by GaAs due to the blue-shift of GaAs E_g. This could be seen as a high temperature dependency of J_{sc} when the cell operation is limited by GaAs. It should be noted that the TCs for J_{sc} acquired with simulator measurements can not be taken as absolute values as the changes in the cell currents are highly affected by the shape of illumination spectrum [111], and always a certain mismatch between the reference and simulated spectra is present. In future, when the multisource simulator is again operational, the above hypothesis could be tested by measuring the temperature dependent LIV characteristics of a single junction GaAs cell with illumination from the multisource system.

The V_{oc} values of the 3J cells drop rapidly with temperature, as can be seen from figure 6.6(b). As the temperature is increased the dark saturation currents of the subcells increase which causes the open-circuit voltages of the subcells to decrease. Because the voltages in MJSCs are cumulative, the slopes for V_{oc} in the MJSC devices are approximately also the sum of the slopes for the individual subcells. This can be observed as relatively high temperature slopes of V_{oc} in MJSCs. From the figure 6.6(b) we can see that V_{oc} values follow linearity extremely well in the observed temperature range. The slopes for V_{oc} between the 3J samples are closely identical; the TCs for V_{oc} were determined to be between -6.8 mV/℃ and -7.1 mV/℃.

A temperature induced reduction also in the FF values can be observed. From the figure 6.6(c) we see that the FF value of S2, which has the highest FF of the 3J cells, is reduced more rapidly than for the other two cells. Also relatively large fluctuations can be observed between the FF values measured at different temperatures. This is probably caused by the measurement inaccuracies of the system, and the limited amount of data points in LIV curve from which the P_{mp} is determined. Still, the overall temperature trends of FF follow linear fits quite well. TCs of -4.3 $\times 10^{-4}$ ℃$^{-1}$ and -2.5 $\times 10^{-4}$ ℃$^{-1}$ were obtained for S2 and S3, respectively. For the cell S1 the linear fitting of FF values was not performed due to the limited number of data points available. Still we can see that, unlike for cells S2 and S3, the FF value of S1 remains nearly constant at the observed temperature interval.

The conversion efficiency is directly proportional to J_{sc}, V_{oc} and FF (see 3.5) and, therefore, the temperature dependency of η is proportional to the temperature dependencies of these parameters. Even though the J_{sc} has a positive temperature slope, it is dominated by the negative slopes of the V_{oc} and FF, causing the temperature slope for efficiency to be negative. Because the temperature dependent values for these parameters follow a linear fit well at this temperature range, a close to linear temperature dependency could also be expected for η. From the figure 6.6(d) we can see that this holds true very well with the exception of S3, for which a change in the slope can be observed at around 20℃. The change in the slope is a direct consequence of the current crossover between the GaInP and GaAs subcells as it was analyzed to cause a more rapid decrease in the J_{sc} at low temperatures. In addition, due to the current crossover between the subcells in S3, the conversion efficiency of S2 is projected to surpass the efficiency of S3 at temperatures below -2℃.

The TCs for J_{sc}, V_{oc}, FF, and η of 3J cells at AM0, and the standard errors of the linear regressions are summarized in table 6.3.

Table 6.3. *Temperature coefficients for the performance parameters of the 3J cells under AM0 illumination and the standard errors for the linear regression fits.*

Cell	Temperature range		$\frac{dJ_{sc}}{dT}$ (μA/cm²/℃)	$\frac{dV_{oc}}{dT}$ (mV/℃)	$\frac{dFF}{dT}$ (10^{-4}/℃)	$\frac{d\eta}{dT}$ (abs.-%/℃)
S1	5–35℃		4.2*	−7.1	n.a.	−0.047
		Std. error	1.54	0.23	n.a.	0.0021
S2	5–90℃		6.6	−7.0	−4.3	−0.071
		Std. error	0.32	0.06	0.25	0.0005
S3	5–20℃		24	−6.8	−2.5	−0.027
		Std. error	1.18	0.06	0.25	0.0032
	20–90℃		6.0	−6.8	−2.5	−0.068
		Std. error	0.26	0.06	0.25	0.0012

*Accuracy affected by the limited number of available data points.

By looking at the standard error values presented in table 6.3 we may see that linear regressions generally offered very good fits to the measured data, and accurate estimations for the TCs could be determined. The measured AM0 TCs are also in reasonably good agreement with values reported for other MJSCs at AM0. Unfortunately, AM0 TCs for 3J cells employing dilute nitride subcells are practically non-existent and, therefore, the results are compared to AM0 coefficients reported for other III–V MJSC devices.

The measured $\frac{\mathrm{dJ_{sc}}}{\mathrm{dT}}$ values are very reasonable in the regions where GaInP limits the 3J currents; for GaInP a TC of 8.8 µA/cm^2/℃ has been reported [99]. Also, the measured coefficients fall in the range measured from other III–V 3J cells as TCs of 5 µA/cm^2/℃ [99] and 11.7 µA/cm^2/℃ [98] have been reported for commercial GaInP/GaAs/Ge and GaInP/InGaAs/Ge 3J cells, respectively. But as noted, the temperature dependency for J_{sc} is largely dependent on the spectrum of the simulator, and for that reason no definitive conclusion are possible

The measured TCs for V_{oc} are nearly identical for all the samples; values close to -7 mV/℃ are measured from each cell. The values are about 1 mV/℃ larger than values reported for GaInP/GaAs/Ge and GaInP/InGaAs/Ge 3J cells at AM0 [98, 99].

The TCs for FF are negative but also relatively small, only order of 10^{-4} ℃$^{-1}$. Similar TCs have been suggested in literature for GaAs and GaInP/GaAs cells [79, 97], and a higher fill factor TC of -4.3×10^{-4} ℃$^{-1}$ has been reported for an GaInP/InGaAs/Ge 3J cell at AM0 [22]. For S1 no significant drop in the FF value could be observed in the narrow temperature range, which might suggest that the $\frac{\mathrm{dFF}}{\mathrm{dT}}$ of S1 could be smaller than for S2 and S3.

The AM0 TCs for the conversion efficiency were found between -0.027 and -0.071 abs.-%/℃. The smallest coefficient was measured at below 20℃ temperatures for S3; at these temperatures the slope of the J_{sc} is more steep due to cell being probably limited by GaAs, causing the η to decline slower with temperature. When the GaInP limits the current, the TC for S3 was found to be -0.068 abs.-%/℃. For S1 a TC of -0.047 abs.-%/℃ was determined which is smaller than the coefficients measured from S2 and S3, that were found to be close to -0.07 abs.-%/℃. The smaller efficiency slope of S1 could be explained with a smaller TC for the FF, as implied by the the figure 6.6. Nevertheless, the

measured TC values are close to -0.057 abs.-%/℃ reported for GaInP/InGaAs/Ge 3J cell [22].

Temperature dependencies under AM1.5D illumination

Similar temperature dependent LIV characterizations were carried out for the cells also at AM1.5D (1000W/m^2) conditions. The temperature dependent AM1.5D measurements were performed also in the temperature range of 5–90℃. The temperature dependencies of the performance parameters at AM1.5D (1000W/m^2) for the 3J samples are presented in figure 6.7.

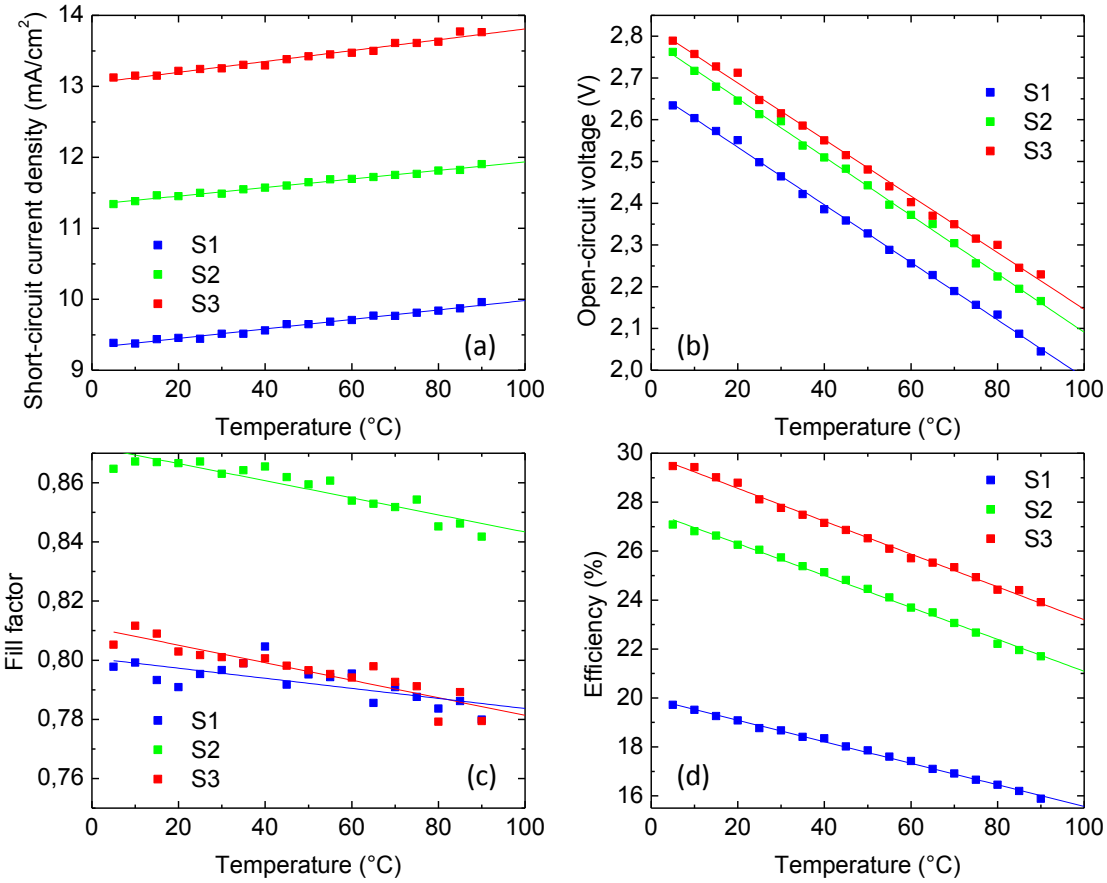

Figure 6.7. *The temperature dependencies of (a) J_{sc}, (b) V_{oc}, (c) FF and, (d) η for the 3J cells under AM1.5D (1000 $\frac{W}{m^2}$) illumination.*

From the figure 6.7 we see that same trends for the temperature dependencies can also be observed at AM1.5D as were seen with the AM0 spectrum. In addition, we can clearly notice that at AM1.5D no changes in the slopes can be observed as was

seen for sample S3 at AM0. Again, the temperature dependent data follows linearity generally well, and good fits could be obtained with linear regressions.

The J_{sc} values are again found to increase with temperature. This time the changes are close to linear over the whole temperature range, as seen from figure 6.7(a), and TCs for J_{sc} ranging 6.0–7.7 µA/cm^2/℃ were determined. Because all the 3J cells were determined to be current-limited by the top cells at AM1.5D at 25℃ (see 6.1), the fact that no changes in the J_{sc} slopes can be observed implies that the cells are limited by the top cells over the whole temperature range with AM1.5D.

The V_{oc} are again observed to decrease linearly with temperature, as shown by figure 6.7(b). For the AM1.5D conditions the linear regression fits for V_{oc} are nearly ideal, and TCs close to -7 mV/℃ were determined for all the cells.

From the figure 6.7(c) the negative temperature dependencies of FFs can again be observed. As it was seen in the case of AM0, the FF values also at AM1.5D vary quite significantly between different temperatures. This, on the other hand, directly results in relatively poor linear regression fits. Nevertheless, the TCs obtained for FF from S2 and S3 are very close to each other, but for the S1 around 44 % smaller TC is observed. The smaller FF temperature coefficient of S1 with AM1.5D is consistent with the observation made from the incomplete data of S1 at AM0 (see table 6.3).

The conversion efficiencies of the cells are significantly reduced with temperature as was also seen with AM0 spectrum. For AM1.5D spectrum the changes in the values of η follow linear behavior throughout the whole temperature range. The TCs are determined to be between -0.047 and -0.067 abs.-%/℃. The slopes for S2 and S3 are very similar, but for S1 a substantially smaller TC was determined; the same observation was made from the AM0 results. Now that complete temperature dependent data for FF is available, it can be said with greater confidence that for S1 the smaller TC for η is mainly caused by the smaller temperature slope for FF.

In table 6.4 the TCs measured for J_{sc}, V_{oc}, FF, and η from the 3J cells at AM1.5D are summarized with the standard errors of the linear regressions.

First, by looking at the standard error values obtained with the linear regressions of the data, given in table 6.4, we can see that relatively good fits were obtained as very small error values can be observed. Only for the FF values the linear regressions produced worse fits, which can be seen as relatively high error values. Still, the

Table 6.4. *Temperature coefficients for the performance parameters of the 3J cells under AM1.5D (1000 W/m^2).*

Cell	Temperature range		$\frac{dJ_{sc}}{dT}$ (µA/cm^2/℃)	$\frac{dV_{oc}}{dT}$ (mV/℃)	$\frac{dFF}{dT}$ (10^{-4}/℃)	$\frac{d\eta}{dT}$ (abs.-%/℃)
S1	5–90℃		6.7	−6.9	−1.7	−0.044
		Std. error	0.22	0.06	0.40	0.0006
S2	5–90℃		6.0	−7.0	−3.0	−0.065
		Std. error	0.18	0.07	0.32	0.0010
S3	5–90℃		7.7	−6.8	−2.9	−0.067
		Std. error	0.31	0.10	0.28	0.0012

temperature dependent trends of FFs could be evaluated, and the values measured from different samples are in relatively good agreement.

When we compare the TCs given in table 6.4 to the corresponding AM0 values given in table 6.3 we see that the values obtained under different spectra are very similar. Especially, the TCs for V_{oc} and η are found to be almost identical with both spectra.

The $\frac{dJ_{sc}}{dT}$ values for S1 and S2 are notably higher with AM1.5D than with AM0 but, conversely, for sample S2 a slightly lower coefficient was measured at AM1.5D. But as said, the TCs for J_{sc} is highly affected by illumination spectrum and, for that reason, decisive conclusions cannot be made based on these values. Still, the obtained coefficients are very close to values reported for other 3J cells; at AM1.5D (900 W/m^2) illumination a TC of 6.6 µA/cm^2/℃ for GaInP/InGaAs/GaInNAs 3J, and TCs of 6.6 and 7.9 µA/cm^2/℃ for two different GaInP/InGaAs/Ge 3J cells have been proposed [15].

As said earlier, the $\frac{dV_{oc}}{dT}$ values measured from the 3J cells at AM1.5D were found to be nearly identical with the values measured at AM0; the largest deviation between coefficients measured with different spectra was 0.1 mV/℃. With AM1.5D spectrum the deviation between the coefficients of different cells is very small as all the coefficient values can be found within -6.9 ± 0.1 mV/℃. The

obtained TCs also correlate well with values reported in literature; for GaInP/InGaAs/Ge cells coefficients of -6.79 mV/℃ (at AM1.5D, 1000 W/m^2) [96] and -6.2 mV/℃ (at AM1.5G, 1000 W/m^2) [76] have been published. For GaInP/GaAs/GaInNAsSb 3J a coefficient of -7.5 mV/℃ at AM1.5D (900 W/m^2) has been previously reported [6].

The $\frac{\mathrm{dFF}}{\mathrm{dT}}$ values of the 3J cells at AM1.5D were determined to be between $-1.7 \times 10^{-4}\,℃^{-1}$ and $-3.0 \times 10^{-4}\,℃^{-1}$. The coefficient for S1 was found to be significantly smaller than for S2 and S3, as it was already speculated based on the AM0 results. The values of $\frac{\mathrm{dFF}}{\mathrm{dT}}$ for S2 and S3 are nearly identical at AM1.5D, but comparing the values with AM0 results we notice that smaller coefficient for S2, and a slightly higher coefficient for S3 was observed at AM1.5D. Still, the TC values are of the same magnitude with both spectra. On the other hand, all the values are found to be somewhat smaller than the $-6 \times 10^{-4}\,℃^{-1}$ reported for GaInP/InGaAs/Ge 3J at AM1.5G (1000 W/m^2) [76].

Similar drops in the conversion efficiencies were observed for the cells at AM1.5D as were observed at AM0. But a notable difference at AM1.5D is that changes in the $\frac{\mathrm{d}\eta}{\mathrm{dT}}$ can not be observed for S3, as there is no current crossover between the subcells of S3. Good linear regression fits could be made for the temperature dependent data, and the $\frac{\mathrm{d}\eta}{\mathrm{dT}}$ values were determined to be between -0.044 and -0.067 abs.-%/℃. The measured coefficients are very close to values measured at AM0, but a slight decrease can be observed in the AM1.5D coefficients. The measured TCs for η are smaller than -0.073 abs.-%/℃ and -0.09 abs.-%/℃ reported for GaInP/InGaAs/Ge at AM1.5G (1000 W/m^2) [76], and for GaInP/GaAs/GaInNAsSb at AM1.5D (900 W/m^2) [6], respectively.

6.2 Quantum efficiency analysis

In this section the 3J cell performance is analyzed based on the EQE data. Here the EQE characteristics of the best performing 3J cell, S3, are considered. The subcell EQEs from the sample S3 have been measured at two temperatures and the EQE curves are presented in figure 6.8.

The data shown in figure 6.8 indicates that all the subcell EQEs are at very high level as the EQEs of GaInP, GaAs, and GaInNAsSb peak at 0.90, 0.89, and 0.93, respectively. The effect of temperature on the material band gaps can be clearly

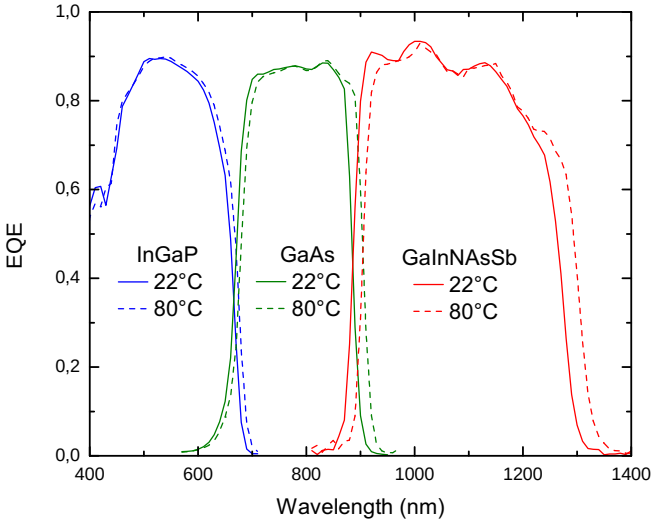

Figure 6.8. *The EQE curves from subcells of S3 measured at 22°C and 80°C. (EQE data courtesy of Dr. Arto Aho)*

seen from the EQE curves; the absorption edges of the subcells are red-shifted with increased temperature. The amount of red-shift is largest for the GaInNAsSb, and for GaInP the smallest shift is be observed. The overall shape of the EQE curves are observed not to change significantly with temperature. From the figure 6.8 we can also see the effect of temperature on the effective absorption bands of the subcells. As the absorption edges of GaInP and GaAs shift towards longer wavelengths, the short-wavelength absorptions of GaAs and GaInNAsSb are reduced, respectively, but at the same time the absorption edges of GaAs and GaInNAsSb red-shift causing increase in the photon absorption at longer wavelengths. Because the TCs of E_g are different for different subcells [100], the widths of the absorption bands change with temperature, which can have a notable impact on the photocurrents. From the EQE data presented in figure 6.8, the short-circuit currents of subcells at AM0 and AM1.5D (1000 W/m^2) reference spectra were estimated by equation 5.3. The calculated J_{sc} values are summarized in table 6.5 along with the AM1.5D values obtained from the multiband simulator measurements.

As can be seen from the table 6.5, the calculated and measured J_{sc} values for the GaInP subcell are in extremely good agreement, as same J_{sc} values were obtained with both methods. For GaInNAsSb subcell J_{sc} values show a relatively good correlation as a 4 % difference between the measured and calculated J_{sc} values is

Table 6.5. *J_{sc} values for subcells of S3 calculated from the EQE data and the ASTM E490–00 AM0 and ASTM G173–3 AM1.5D (1000 W/m^2) reference spectra along with J_{sc} values obtained from the multiband measurements at AM1.5D (1000 W/m^2).*

Subcell	Temperature	$J_{sc,EQE}$ AM0 (mA/cm^2)	$J_{sc,EQE}$ AM1.5D (mA/cm^2)	$J_{sc,LIV}$ AM1.5D, 25 ℃ (mA/cm^2)	$\frac{\Delta J_{sc(LIV-EQE)}}{J_{sc,EQE}}$ AM1.5D
GaInP	22℃	17.0	13.2	13.2	0.0 %
	80℃	17.3	13.6		
GaAs	22℃	14.3	13.2	14.9	12.9 %
	80℃	14.8	13.6		
GaInNAsSb	22℃	18.5	15.1	15.7	4.0 %
	80℃	18.4	15.1		

observed. For GaAs subcell, on the other hand, a 12.9 % deviation between the calculated and measured J_{sc} values was determined. The EQE data suggests that S3 would be clearly current-limited by the GaAs cell at AM0 which, on the other hand, is in direct conflict with the multiband LIV results. This suggests that the performance of the EQE measurement for GaAs junction has been limited, which has led to underestimation of the GaAs EQE.

From the J_{sc} values calculated from EQEs we can see that the currents of GaInP and GaAs subcells are increased with temperature, but for GaInNAsSb the currents remain nearly constant. For the top and the middle cells the net amount of photogeneration is increased when the absorption edges are shifted, but for GaInNAsSb the gain in photons from the red-shift of its absorption edge is nearly balanced by the amount of photons lost to the middle cell as the absorption edge of GaAs red-shifts, causing the net change in the photogeneration to be very small.

Because the sample S3 was found to be current-limited by the GaInP top cell at normal and elevated temperatures with the multiband LIV measurements, and the difference between measured and calculated J_{sc} values for GaInP is small, the TC for J_{sc} of S3 can be estimated from the EQE data of the GaInP subcell. This yields to TCs of around 6.8 and 6.9 µA/cm^2/℃ at AM0 and AM1.5D, respectively.

The coefficient values obtained from the EQE deviate from the values determined from the LIV measurements (see tables 6.3 and 6.4). The differences compared to coefficient values obtained from the LIV measurements are 13 % and -10 % at AM0 and AM1.5D, respectively. This might be caused by unideal simulator spectra near the band edge of GaInP. Still, the values are of the same magnitude which increases the trustworthiness of the multisource simulator system used extensively for this thesis.

7. CONCLUSIONS

In this thesis high-efficiency triple-junction III–V semiconductor solar cells for space and terrestrial applications were studied. The investigated multijunction cells employed GaInP, GaAs and GaInNAsSb subcells, and the structures were monolithically grown with plasma-assisted molecular beam epitaxy at ORC. The main emphasis of this thesis was on the characterization of the GaInP/GaAs/GaInNAsSb 3J cells. The effects of illumination spectra and temperature on the cell performance were investigated. Three 3J cells with different top cell thicknesses were chosen for the study.

The majority of the solar cell characterization for this thesis was done with current-voltage measurements, and for these a custom solar simulator setup with three illumination bands was built around an existing Xenon-simulator by adding two additional halogen lamps, and for each light source a proper combination of filters for AM0 and AM1.5D conditions were selected. With this system the spectral bands could be adjusted separately to achieve better spectral matching, but it also enabled the testing of current-matching between the 3J subcells. The system was calibrated with EQE calibrated single-junction solar cells. The AM1.5D calibration was checked with a new OAI simulator for which a less than 2 % error in the spectrum calibration was measured with and a Fraunhofer ISE calibrated cell. Then a set of single-junction GaInNAsSb cells were measured with the OAI and multisource simulators, and the results were found to be within 1 % from each other.

In the room temperature LIV measurements the 3J cell with the thickest GaInP cell performed best, demonstrating conversion efficiencies of 27 % and 28 % at AM0 and AM1.5D, respectively. Unfortunately, when the multisource and Xenon-simulator data were compared it was found that the cell had sustained some damage. If the cell would had been in pristine condition, conversion efficiency as high as 31 % at AM1.5D could have been realistically expected. In addition, the currents under the Xenon-simulator deviated significantly from values measured under the multisource

simulator; largest deviation in the currents was found to be 36 % which translates into difference of 8 percentage points in efficiency. In the current-balancing tests all the cells were determined to be current-limited by the GaInP top cells at room temperature. The dilute nitride subcells were found to overgenerate current in all the 3J cells. Based on calculations, the conversion efficiency of the best cell could be further boosted by a 2.5 percentage points at AM1.5D with better current-matching.

The temperature dependencies of the performance parameters were investigated in temperature range of 5–90℃ at AM0 and AM1.5D. The J_{sc} values showed increase with temperature, but the V_{oc} and FF values, on the other hand, declined as function of temperature. The temperature dependency of η was also determined to be negative. Temperature coefficients for the performance parameters were obtained with linear regression analysis. The obtained temperature coefficients showed good correlation when compared to temperature coefficient values reported for other III–V multijunction cells in literature.

The EQE curves measured at 22℃ and 80℃ from the 3J with the thickest top cell were also analyzed. From the EQE curves the temperature induced band gap narrowing was clearly observed. J_{sc} values of subcells at both temperatures were calculated from the EQE data. Good correlation between the calculated and the measured J_{sc} values at AM1.5D were found for the GaInP and GaInNAsSb subcells, but for the GaAs junction the calculated value was significantly smaller than the measured value which was analyzed to be caused by a limited performance of the EQE measurement for the GaAs junction. The J_{sc} temperature coefficients of the 3J cell was estimated from the EQE data of GaInP subcell; the calculated coefficients were of the same magnitude as the temperature coefficients extracted from the multisource LIV measurements.

The multisource simulator proved to be an accurate and stable tool for the characterization of MJSCs. Still, the system could be further developed in future. First, the maximum cell size supported by the system could be increased by replacing the long wavelength halogen with a similar halogen light source used for the middle band illumination. Secondly, the definition of the spectral bands could be increased with more suitable filter combinations. Thirdly, the system could be expanded with additional light sources. In principle the system could be expanded to eight spectral bands to support future development of MJSCs with up to eight junctions.

REFERENCES

[1] S. Adachi, "Electronic Energy-Band Structure," in: Physical Properties of III–V Semiconductor Compounds, Wiley-VCH Verlag GmbH & Co. KGaA, 2005, pp. 75–117.

[2] A. Aho, V.-M. Korpijärvi, R. Isoaho, P. Malinen, A. Tukiainen, M. Honkanen, and M. Guina, "Determination of composition and energy gaps of GaInNAsSb layers grown by MBE," *Journal of Crystal Growth*, vol. 438, 2016, pp. 49–54.

[3] A. Aho, A. Tukiainen, V. Polojärvi, and M. Guina, "Performance assessment of multijunction solar cells incorporating GaInNAsSb," *Nanoscale Research Letters*, vol. 9, 2014, pp. 1–7.

[4] A. Aho, A. Tukiainen, V. Polojärvi, J. Salmi, and M. Guina, "High current generation in dilute nitride solar cells grown by molecular beam epitaxy," *SPIE Conference Proceedings*, vol. 8620, SPIE, 2013, pp. 1–6.

[5] A. Aho, "Dilute Nitride Multijunction Solar Cells Grown by Molecular Beam Epitaxy," Dissertation, Tampere University of Technology. Publication 1343, 2015, 80 p.

[6] A. Aho, R. Isoaho, A. Tukiainen, V. Polojärvi, T. Aho, M. Raappana, and M. Guina, "Temperature coefficients for GaInP/GaAs/GaInNAsSb solar cells," *AIP Conference Proceedings*, vol. 1679, 2015, pp. 1–5.

[7] A. Aho, V. Polojärvi, V.-M. Korpijärvi, J. Salmi, A. Tukiainen, P. Laukkanen, and M. Guina, "Composition dependent growth dynamics in molecular beam epitaxy of GaInNAs solar cells," *Solar Energy Materials and Solar Cells*, vol. 124, 2014, pp. 150–158.

[8] A. Aho, J. Tommila, A. Tukiainen, V. Polojärvi, T. Niemi, and M. Guina, "Moth eye antireflection coated GaInP/GaAs/GaInNAs solar cell," *CPV-10 Proceedings, 10th International Conference on Concentrator Photovoltaic Systems, April 7-9, 2014, Albuquerque, NM, USA, AIP Conference Proceedings*, American Institute of Physics, 2014, pp. 33–36.

[9] A. Aho, A. Tukiainen, V. Polojärvi, J. Salmi, and M. Guina, "MBE Growth of High Current Dilute III–V-N Single and Triple Junction Solar Cells,"

Proceedings of the 27th European Photovoltaic Solar Energy Conference and Exhibition, EU PVSEC 2012, 24-28 September, 2012, Frankfurt, Germany, WIP Wirtschaft und Infrastruktur, 2012, pp. 290–292.

[10] T. Al Zoubi, "Molecular Beam Epitaxial Growth of III–V Semiconductor Nanostructures on Silicon Substrates," Dissertation, University of Kassel, 2013, 150 p.

[11] ASTM E490-00a, "Standard Solar Constant and Zero Air Mass Solar Spectral Irradiance Tables," West Conshohocken, PA: ASTM International, 2000.

[12] ASTM G173-03, "Standard Tables for Reference Solar Spectral Irradiances: Direct Normal and Hemispherical on 37°Tilted Surface," West Conshohocken, PA: ASTM International, 2003.

[13] S. Bailey and R. Raffaelle, "Space Solar Cells and Arrays," in: Handbook of Photovoltaic Science and Engineering, John Wiley & Sons, Ltd, 2005, pp. 413–448.

[14] A. E. Becquerel, "Recherches sur les effets de la radiation chimique de la lumiere solaire au moyen des courants electriques," *Comptes Rendus de L'Academie des Sciences*, vol. 9, 1839, pp. 145–149.

[15] A. Braun, E. A. Katz, and J. M. Gordon, "Basic aspects of the temperature coefficients of concentrator solar cell performance parameters," *Progress in Photovoltaics: Research and Applications*, vol. 21, no. 5, 2013, pp. 1087–1094.

[16] M. Brozel, "Gallium Arsenide," in: Springer Handbook of Electronic and Photonic Materials, Boston, MA: Springer US, 2007, pp. 499–536.

[17] H. Carrére, A. Arnoult, A. Ricard, X. Marie, T. Amand, and E. Bedel-Pereira, "Nitrogen-plasma study for plasma-assisted MBE growth of 1.3 µm laser diodes," *Solid-State Electronics*, vol. 47, no. 3, 2003, pp. 419–423.

[18] L. Castañer and S. Silvestre, "Modelling Photovoltaic Systems Using PSpice," Wiley-VCH Verlag GmbH & Co. KGaA, 2003, 376 p.

[19] D. M. Chapin, C. S. Fuller, and G. L. Pearson, "A New Silicon p-n Junction Photocell for Converting Solar Radiation into Electrical Power," *Journal of Applied Physics*, vol. 25, no. 5, 1954, pp. 676–677.

[20] K. Y. Cheng, "Molecular beam epitaxy technology of III–V compound semiconductors for optoelectronic applications," *Proceedings of the IEEE*, vol. 85, no. 11, 1997, pp. 1694–1714.

[21] A. Y. Cho and J. R. Arthur, "Molecular beam epitaxy," *Progress in Solid State Chemistry*, vol. 10, 1975, pp. 157–191.

[22] B. Cho, J. Davis, L. Hise, A. Korostyshevsky, G. Smith, A. V. Ley, P. Sharps, T. Varghese, and M. Stan, "Qualification testing of the ZTJ GaInP2/GaInAs/Ge solar cell to the AIAA S-111 standard," *Photovoltaic Specialists Conference (PVSC), 2009 34th IEEE*, 2009, pp. 001 009–001 014.

[23] K. L. Chopra and S. R. Das, "Thin Film Solar Cells," New York: Springer Science & Business Media, 1983, 607 p.

[24] H. Cotal and R. Sherif, "Temperature Dependence of the IV Parameters from Triple Junction GaInP/InGaAs/Ge Concentrator Solar Cells," *2006 IEEE 4th World Conference on Photovoltaic Energy Conference*, vol. 1, 2006, pp. 845–848.

[25] M. del Mar Sanz and I. Tanarro, "Chapter 2 - Plasma basic concepts and Nitrogen containing plasmas, 1st ed.," in: Nitrides and Dilute Nitrides: Growth, Physics and Devices, Transworld Research Network, 2007, pp. 15–46.

[26] D. Derkacs, D. T. Bilir, and V. A. Sabnis, "Luminescent Coupling in GaAs/GaInNAsSb Multijunction Solar Cells," *IEEE Journal of Photovoltaics*, vol. 3, no. 1, 2013, pp. 520–527.

[27] F. Dimroth, M. Grave, P. Beutel, U. Fiedeler, C. Karcher, T. N. D. Tibbits, E. Oliva, G. Siefer, M. Schachtner, A. Wekkeli, A. W. Bett, R. Krause, M. Piccin, N. Blanc, C. Drazek, E. Guiot, B. Ghyselen, T. Salvetat, A. Tauzin, T. Signamarcheix, A. Dobrich, T. Hannappel, and K. Schwarzburg, "Wafer bonded four-junction GaInP/GaAs//GaInAsP/GaInAs concentrator solar cells with 44.7% efficiency," *Progress in Photovoltaics: Research and Applications*, vol. 22, no. 3, 2014, pp. 277–282.

[28] M. Dumitrescu, M. Wolf, K. Schulz, Y. Wei, G. Adolfsson, J. Gustavsson, J. Bengtsson, M. Sadeghi, S. Wang, A. Larsson, J. Lim, E. Larkins, P. Melanen, P. Uusimaa, and M. Pessa, "10 Gb/s Uncooled Dilute-Nitride Optical Transmitters Operating at 1.3 µm," *Optical Fiber Communication*

Conference and National Fiber Optic Engineers Conference, Optical Society of America, 2009, pp. 1–3.

[29] K. Emery, "Measurement and Characterization of Solar Cells and Modules," in: Handbook of Photovoltaic Science and Engineering, John Wiley & Sons, Ltd, 2005, pp. 701–752.

[30] A. Fahrenbruch and R. Bube, "Fundamentals Of Solar Cells: Photovoltaic Solar Energy Conversion," New York, USA: Academic Press, 1983, 580 p.

[31] N. Fatemi, J. Lyons, and M. Eskenazi, "Qualification and production of Emcore ZTJ solar panels for space missions," *Photovoltaic Specialists Conference (PVSC), 2013 IEEE 39th*, 2013, pp. 2793–2796.

[32] S. Franchi, "Chapter 1 - Molecular beam epitaxy: fundamentals, historical background and future prospects," in: Molecular Beam Epitaxy, Oxford: Elsevier, 2013, pp. 1–46.

[33] Fraunhofer ISE, "Press release," 2014, [WWW, Accessed 29.3.2016]. Available: https://www.ise.fraunhofer.de/en/press-and-media/press-releases/press-releases-2014/new-world-record-for-solar-cell-efficiency-at-46-percent

[34] Fraunhofer ISE, "Photovoltaics Report," 2016, [WWW, accessed 29.3.2015]. Available: https://www.ise.fraunhofer.de/de/downloads/pdf-files/aktuelles/photovoltaics-report-in-englischer-sprache.pdf

[35] D. J. Friedman, "Modelling of tandem cell temperature coefficients," *Photovoltaic Specialists Conference, 1996., Conference Record of the Twenty Fifth IEEE*, 1996, pp. 89–92.

[36] D. J. Friedman, J. F. Geisz, and M. A. Steiner, "Analysis of Multijunction Solar Cell Current-Voltage Characteristics in the Presence of Luminescent Coupling," *IEEE Journal of Photovoltaics*, vol. 3, no. 4, 2013, pp. 1429–1436.

[37] D. J. Friedman, J. F. Geisz, and M. A. Steiner, "Effect of Luminescent Coupling on the Optimal Design of Multijunction Solar Cells," *IEEE Journal of Photovoltaics*, vol. 4, no. 3, 2014, pp. 986–990.

[38] J. L. Gray, "The Physics of the Solar Cell," in: Handbook of Photovoltaic Science and Engineering, John Wiley & Sons, Ltd, 2005, pp. 61–112.

[39] M. Green, "Photovoltaics: coming of age," *Photovoltaic Specialists Conference, 1990., Conference Record of the Twenty First IEEE*, 1990, pp. 1–8.

[40] M. A. Green, K. Emery, Y. Hishikawa, W. Warta, and E. D. Dunlop, "Solar cell efficiency tables (version 47)," *Progress in Photovoltaics: Research and Applications*, vol. 24, no. 1, 2016, pp. 3–11.

[41] M. Grundmann, "The Physics of Semiconductors: An Introduction Including Nanophysics and Applications," 2nd ed., Springer Berlin Heidelberg, 2010, 864 p.

[42] M. Guden and J. Piprek, "Material parameters of quaternary III–V semiconductors for multilayer mirrors at 1.55 µm wavelength," *Modelling and Simulation in Materials Science and Engineering*, vol. 4, no. 4, 1996, pp. 349–357.

[43] C. A. Gueymard, "Recent Developments in Spectral Solar Radiation Standards and Modelling," *Solar Spectrum, Newsletter of the American Solar Energy Society's Resource Assessment Division*, vol. 16, no. 1, 2003, pp. 4–8.

[44] M. Guina and S. H. Wang, "Chapter 9 - MBE of dilute-nitride optoelectronic devices," in: Molecular Beam Epitaxy, Oxford: Elsevier, 2013, pp. 171–187.

[45] J. S. Harris, H. Yuen, S. Bank, M. Wistey, V. Lordi, T. Gugov, H. Bae, and L. Goddard, "Chapter 1 - MBE Growth and Characterization of Long Wavelength Dilute Nitride III–V Alloys," in: Dilute Nitride Semiconductors, Amsterdam: Elsevier, 2005, pp. 1–92.

[46] J. S. Harris, R. Kudrawiec, H. B. Yuen, S. R. Bank, H. P. Bae, M. A. Wistey, D. Jackrel, E. R. Pickett, T. Sarmiento, L. L. Goddard, V. Lordi, and T. Gugov, "Development of GaInNAsSb alloys: Growth, band structure, optical properties and applications," *physica status solidi (b)*, vol. 244, no. 8, 2007, pp. 2707–2729.

[47] M. A. Herman, W. Richter, and H. Sitter, "Epitaxy: Physical Principles and Technical Implementation," Springer Berlin Heidelberg, 2013, 525 p.

[48] M. A. Herman and H. Sitter, "Molecular Beam Epitaxy: Fundamentals and Current Status," Springer Berlin Heidelberg, 1996, 453 p.

[49] L. C. Hirst and N. J. Ekins-Daukes, "Fundamental losses in solar cells," *Progress in Photovoltaics: Research and Applications*, vol. 19, no. 3, 2011, pp. 286–293.

[50] M. Hugues, B. Damilano, J. M. Chauveau, J. Y. Duboz, and J. Massies, "Blue-shift mechanisms in annealed (Ga,In)(N,As)/GaAs quantum wells," *Phys.Rev.B*, vol. 75, no. 4, 2007, pp. 1–6.

[51] International Energy Agency, "A Snapshot of Global PV (1992-2014), IEA PVPS T1-26:2015," 2015, [WWW, accessed 29.3.2016]. Available: http://www.iea-pvps.org/fileadmin/dam/public/report/technical/PVPS_report_-_A_Snapshot_of_Global_PV_-_1992-2014.pdf

[52] R. Isoaho, "Antimonia ja typpeä sisältävien yhdistepuolijohdeaurinkokennojen kvanttihyötysuhteen lämpötilariippuvuuden määrittäminen," 2014, 35 p.

[53] D. B. Jackrel, S. R. Bank, H. B. Yuen, M. A. Wistey, J. S. Harris, A. J. Ptak, S. W. Johnston, D. J. Friedman, and S. R. Kurtz, "Dilute nitride GaInNAs and GaInNAsSb solar cells by molecular beam epitaxy," *Journal of Applied Physics*, vol. 101, no. 11, 2007, pp. 1–8.

[54] M. Kaltenbrunner, M. S. White, E. D. Głowacki, T. Sekitani, T. Someya, N. S. Sariciftci, and S. Bauer, "Ultrathin and lightweight organic solar cells with high flexibility," *Nature Communications*, vol. 3, 2012, pp. 1–7.

[55] G. S. Kinsey, P. Hebert, K. E. Barbour, D. D. Krut, H. L. Cotal, and R. A. Sherif, "Concentrator multijunction solar cell characteristics under variable intensity and temperature," *Progress in Photovoltaics: Research and Applications*, vol. 16, no. 6, 2008, pp. 503–508.

[56] V. Kirchner, H. Heinke, U. Birkle, S. Einfeldt, D. Hommel, H. Selke, and P. L. Ryder, "Ion-induced crystal damage during plasma-assisted MBE growth of GaN layers," *Phys.Rev.B*, vol. 58, no. 23, 1998, pp. 15 749–15 755.

[57] A. Köhler and H. Bässler, "The Electronic Structure of Organic Semiconductors," in: Electronic Processes in Organic Semiconductors, Wiley-VCH Verlag GmbH & Co. KGaA, 2015, pp. 1–86.

[58] M. Kondow, K. Uomi, A. Niwa, T. Kitatani, S. Watahiki, and Y. Yazawa, "GaInNAs: A Novel Material for Long-Wavelength-Range Laser Diodes

with Excellent High-Temperature Performance," *Japanese Journal of Applied Physics*, vol. 35, no. 2S, 1996, pp. 1273–1275.

[59] G. Kopp and J. L. Lean, "A new, lower value of total solar irradiance: Evidence and climate significance," *Geophysical Research Letters*, vol. 38, no. 1, 2011, pp. 1–7.

[60] V. M. Korpijärvi, "Growth of short-wavelength dilute nitride semiconductor disk lasers by molecular beam epitaxy," MSc Thesis. Tampere: Tampere University of Technology, 2010, 110 p.

[61] V. M. Korpijärvi, E. L. Kantola, T. Leinonen, R. Isoaho, and M. Guina, "Monolithic GaInNAsSb/GaAs VECSEL Operating at 1550 nm," *IEEE Journal of Selected Topics in Quantum Electronics*, vol. 21, no. 6, 2015, pp. 480–484.

[62] V.-M. Korpijärvi, "High-Power Dilute Nitride Lasers Grown by Molecular Beam Epitaxy," Dissertation, Tampere University of Technology. Publication 1346, 2015, 88 p.

[63] R. A. Kubiak, S. M. Newstead, and P. Sullivan, "Chapter 1 - The Technology and Design of Molecular Beam Epitaxy Systems," in: Molecular Beam Epitaxy, Park Ridge, NJ: William Andrew Publishing, 1995, pp. 1–113.

[64] E. C. Larkins and J. S. H. Jr., "Chapter 2 - Molecular Beam Epitaxy of High-Quality GaAs and AIGaAs," in: Molecular Beam Epitaxy, Park Ridge, NJ: William Andrew Publishing, 1995, pp. 114–274.

[65] J.-J. Liu, W.-J. Ho, J.-K. Syu, Y.-Y. Lee, C.-F. Lin, and H.-P. Shiao, "Performance improvement of a triple-junction GaAs-based solar cell using a SiO 2-nanopillars/SiO2 /TiO 2 graded-index antireflection coating," *International Journal of Nanotechnology*, vol. 11, no. 1-234, 2014, pp. 311–321.

[66] L. Liu, N. Chen, Y. Bai, M. Cui, H. Zhang, F. Gao, Z. Yin, and X. Zhang, "Quantum efficiency and temperature coefficients of GaInP/GaAs dual-junction solar cell," *Science in China Series E: Technological Sciences*, vol. 52, no. 5, 2009, pp. 1176–1180.

[67] S. H. Liu, E. J. Simburger, J. Matsumoto, A. Garcia, J. Ross, and J. Nocerino, "Evaluation of thin-film solar cell temperature coefficients for

space applications," *Progress in Photovoltaics: Research and Applications*, vol. 13, no. 2, 2005, pp. 149–156.

[68] X. Liu, M. E. Pistol, L. Samuelson, S. Schwetlick, and W. Seifert, "Nitrogen pair luminescence in GaAs," *Applied Physics Letters*, vol. 56, no. 15, 1990, pp. 1451–1453.

[69] V. Lordi, "Band-edge optical properties of GaInNAs(Sb) and the relation to atomic structure," Dissertation, Stanford University, 2004, 215 p.

[70] T. Markvart and L. Castañer, "IIa-1 - Principles of solar cell operation," in: Solar Cells: Materials, Manufacture and Operation, Oxford: Elsevier Science, 2005, pp. 5–27.

[71] J. W. Matthews and A. E. Blakeslee, "Defects in epitaxial multilayers: I. Misfit dislocations," *Journal of Crystal Growth*, vol. 27, 1974, pp. 118–125.

[72] D. A. Murdick, X. W. Zhou, and H. N. G. Wadley, "Low-temperature atomic assembly of stoichiometric gallium arsenide from equiatomic vapor," *Journal of Crystal Growth*, vol. 286, no. 1, 2006, pp. 197–204.

[73] H. P. Myers, "Introductory Solid State Physics," 2nd ed., Boca Raton: CRC Press, 1997, 536 p.

[74] Newport Corporation, "Curve normalization," [WWW, Accessed: 29.4.2016]. Available: http://www.newport.com/Curve-Normalization/412214/1033/content.aspx

[75] Newport Corporation, "Introduction to solar radiation," [WWW, Accessed: 19.3.2016]. Available: http://www.newport.com/Introduction-to-Solar-Radiation/411919/1033/content.aspx

[76] K. Nishioka, T. Takamoto, T. Agui, M. Kaneiwa, Y. Uraoka, and T. Fuyuki, "Annual output estimation of concentrator photovoltaic systems using high-efficiency InGaP/InGaAs/Ge triple-junction solar cells based on experimental solar cell's characteristics and field-test meteorological data," *Solar Energy Materials and Solar Cells*, vol. 90, no. 1, 2006, pp. 57–67.

[77] NREL, "Best research-cell efficiencies," 2016, [WWW, accessed 22.8.2016]. Available: http://www.nrel.gov/ncpv/images/efficiency_chart.jpg

[78] K. P. O'Donnell and X. Chen, "Temperature dependence of semiconductor band gaps," *Applied Physics Letters*, vol. 58, no. 25, 1991, pp. 2924–2926.

[79] J. M. Olson, D. J. Friedman, and S. Kurtz, "High-Efficiency III–V Multijunction Solar Cells," in: Handbook of Photovoltaic Science and Engineering, John Wiley & Sons, Ltd, 2005, pp. 359–411.

[80] V. Ottesen, "MBE.png," [WWW, accessed 26.3.2016]. Available: https://en.wikipedia.org/wiki/Molecular_beam_epitaxy#/media/File:MBE.png

[81] R. Pelzel, "A Comparison of MOVPE and MBE Growth Technologies for III-V Epitaxial Structures," *CS MANTECH Conference, May 13th - 16th, 2013, New Orleans, Louisiana, USA*, 2013.

[82] K. Ploog, "Semiconductor Interfaces: Formation and Properties," in: Formation of Semiconductor Interfaces During Molecular Beam Epitaxy, Berlin, Heidelberg: Springer Berlin Heidelberg, 1987, pp. 10–42.

[83] V. Polojärvi, "Novel III–V Heterostructures for High Efficiency Solar Cells: Studies of Electrical and optical properties," Dissertation, Tampere University of Technology. Publication 1383, 2016, 98 p.

[84] V. V. Preobrazhenskii, D. I. Lubyshev, K. Regiński, and J. Muszalski, "The effect of the MBE growth rate on the surface phase diagram for GaAs (001)," *Thin Solid Films*, vol. 267, no. 1-2, 1995, pp. 51–53.

[85] A. J. Ptak, D. J. Friedman, S. Kurtz, and R. C. Reedy, "Low-acceptor-concentration GaInNAs grown by molecular-beam epitaxy for high-current p-i-n solar cell applications," *Journal of Applied Physics*, vol. 98, no. 9, 2005, pp. 1–5.

[86] PV Education.org, "Standard Solar Spectra," [WWW, Accessed: 19.3.2016]. Available: http://www.pveducation.org/pvcdrom/appendices/standard-solar-spectra

[87] M. Raappana, "Wet etching of dilute nitride and antimonide semiconductors for solar cells," MSc Thesis. Tampere: Tampere University of Technology, 2015, 75 p. + 6 appendix.

[88] G. Ramírez-Flores, H. Navarro-Contreras, A. Lastras-Martínez, R. C. Powell, and J. E. Greene, "Temperature-dependent optical band gap of the metastable

zinc-blende structure β-GaN," *Phys.Rev.B*, vol. 50, no. 12, 1994, pp. 8433–8438.

[89] M. Razeghi, "Technology of Quantum Devices," Springer US, 2009, 560 p.

[90] V. Sabnis, H. Yuen, and M. Wiemer, "High-efficiency multijunction solar cells employing dilute nitrides," *AIP Conference Proceedings*, vol. 1477, no. 1, 2012, pp. 14–19.

[91] C. T. Sah, R. N. Noyce, and W. Shockley, "Carrier Generation and Recombination in P-N Junctions and P-N Junction Characteristics," *Proceedings of the IRE*, vol. 45, no. 9, 1957, pp. 1228–1243.

[92] H. Sakaki, "Chapter 5 - Molecular Beam Epitaxy," in: III–V Semiconductor Materials and Devices, Netherlands: North-Holland, 1989, vol. 7, pp. 217–330.

[93] W. Shan, W. Walukiewicz, J. W. Ager, E. E. Haller, J. F. Geisz, D. J. Friedman, J. M. Olson, and S. R. Kurtz, "Band Anticrossing in GaInNAs Alloys," *Phys.Rev.Lett.*, vol. 82, no. 6, 1999, pp. 1221–1224.

[94] W. Shockley and W. T. Read, "Statistics of the Recombinations of Holes and Electrons," *Phys.Rev.*, vol. 87, no. 5, 1952, pp. 835–842.

[95] G. Siefer and A. W. Bett, "Calibration of III–V Concentrator Cells and Modules," *Photovoltaic Energy Conversion, Conference Record of the 2006 IEEE 4th World Conference on*, vol. 1, 2006, pp. 745–748.

[96] G. Siefer and A. W. Bett, "Analysis of temperature coefficients for III–V multi-junction concentrator cells," *Progress in Photovoltaics: Research and Applications*, vol. 22, no. 5, 2014, pp. 515–524.

[97] P. Singh and N. M. Ravindra, "Temperature dependence of solar cell performance - an analysis," *Solar Energy Materials and Solar Cells*, vol. 101, 2012, pp. 36–45.

[98] SolAero Technologies, "ZTJ Space Solar Cell Datasheet," [WWW, Accessed: 11.5.2016]. Available: http://solaerotech.com/wp-content/uploads/2015/03/ZTJ-Datasheet.pdf

[99] Spectrolab, "28.3% Ultra Triple Junction (UTJ) Solar Cells Datasheet," [WWW, Accessed: 11.5.2016]. Available: http://www.spectrolab.com/DataSheets/TNJCell/utj3.pdf

[100] M. A. Steiner, J. F. Geisz, D. J. Friedman, W. J. Olavarria, A. Duda, and T. E. Moriarty, "Temperature-dependent measurements of an inverted metamorphic multijunction (IMM) solar cell," *Photovoltaic Specialists Conference (PVSC), 2011 37th IEEE*, 2011, pp. 002 527–002 532.

[101] M. A. Steiner, J. F. Geisz, T. E. Moriarty, R. M. France, W. E. McMahon, J. M. Olson, S. R. Kurtz, and D. J. Friedman, "Measuring IV curves and subcell photocurrents in the presence of luminescent coupling," *Photovoltaic Specialists Conference (PVSC), Volume 2, 2012 IEEE 38th*, 2012, pp. 1–11.

[102] M. A. Steiner and J. F. Geisz, "Non-linear luminescent coupling in series-connected multijunction solar cells," *Applied Physics Letters*, vol. 100, no. 25, 2012.

[103] B. G. Streetman and S. Banerjee, "Solid state electronic devices," 5th ed., Upper Saddle River, New Jersey: Prentice Hall, Inc., 2000, 558 p.

[104] W. H. Strehlow and E. L. Cook, "Compilation of Energy Band Gaps in Elemental and Binary Compound Semiconductors and Insulators," *Journal of Physical and Chemical Reference Data*, vol. 2, no. 1, 1973, pp. 163–200.

[105] O. Svelto, "Principles of Lasers," 5th ed., Boston, MA: Springer US, 2010, 620 p.

[106] S. P. Tobin, S. M. Vernon, M. M. Sanfacon, and A. Mastrovito, "Enhanced light absorption in GaAs solar cells with internal Bragg reflectors," *Photovoltaic Specialists Conference, 1991., Conference Record of the Twenty Second IEEE*, 1991, pp. 147–152.

[107] A. Tukiainen, A. Aho, G. Gori, V. Polojärvi, M. Casale, E. Greco, R. Isoaho, T. Aho, M. Raappana, R. Campesato, and M. Guina, "High-efficiency GaInP/GaAs/GaInNAs solar cells grown by combined MBE-MOCVD technique," *Progress in Photovoltaics: Research and Applications*, vol. 24, no. 7, 2016, pp. 914–919.

[108] U.S. Energy Information Administration, "International Energy Outlook 2016," 2016, [WWW, accessed 11.6.2016]. Available: http://www.eia.gov/forecasts/ieo/

[109] Y. P. Varshni, "Temperature dependence of the energy gap in semiconductors," *Physica*, vol. 34, no. 1, 1967, pp. 149–154.

[110] L. Vegard, "Die Konstitution der Mischkristalle und die Raumfüllung der Atome," *Zeitschrift für Physik*, vol. 5, no. 1, 1921, pp. 17–26.

[111] G. F. Virshup, B. C. Chung, M. L. Ristow, M. S. Kuryla, and D. Brinker, "Temperature coefficients of multijunction solar cells," *Photovoltaic Specialists Conference, 1990., Conference Record of the Twenty First IEEE*, 1990, pp. 336–338.

[112] A. D. Vos, "Detailed balance limit of the efficiency of tandem solar cells," *Journal of Physics D: Applied Physics*, vol. 13, no. 5, 1980, pp. 839 – 846.

[113] I. Vurgaftman, J. R. Meyer, and L. R. Ram-Mohan, "Band parameters for III–V compound semiconductors and their alloys," *Journal of Applied Physics*, vol. 89, no. 11, 2001, pp. 5815–5875.

[114] A. W. Walker, J. F. Wheeldon, O. Theriault, M. D. Yandt, and K. Hinzer, "Temperature dependent external quantum efficiency simulations and experimental measurement of lattice matched quantum dot enhanced multi-junction solar cells," *Photovoltaic Specialists Conference (PVSC), 2011 37th IEEE*, 2011, pp. 000 564–000 569.

[115] M. Weyers, M. Sato, and H. Ando, "Red Shift of Photoluminescence and Absorption in Dilute GaAsN Alloy Layers," *Japanese Journal of Applied Physics*, vol. 31, no. 7A, 1992, pp. 853–855.

[116] D. R. Williams, "Sun fact sheet," [WWW, Accessed: 19.3.2016]. Available: http://nssdc.gsfc.nasa.gov/planetary/factsheet/sunfact.html

[117] C. W. Wilmsen, L. A. Coldren, and H. Temkin, "Vertical-Cavity Surface-Emitting Lasers: Design, Fabrication, Characterization, and Applications," Cambridge University Press, 2001, 474 p.

[118] M. A. Wistey, "Growth Of 1.5 µm GaInNAsSb Vertical Cavity Surface Emitting Lasers by Molecular Beam Epitaxy," 2006, 237 p.

[119] S. Wolf and R. N. Tauber, "Silicon Processing for the VLSI Era: Process technology," Lattice Press, 2000, 890 p.

[120] D. N. Wright, E. S. Marstein, and A. Holt, "Double layer anti-reflective coatings for silicon solar cells," *Photovoltaic Specialists Conference, 2005. Conference Record of the Thirty-first IEEE*, 2005, pp. 1237–1240.

[121] T. Yang, X. Wang, W. Liu, Y. Shi, and F. Yang, "Double-layer anti-reflection coating containing a nanoporous anodic aluminum oxide layer for GaAs solar cells," *Optics Express*, vol. 21, no. 15, 2013, pp. 18 207–18 215.

[122] X. Yang, M. J. Jurkovic, J. B. Heroux, and W. I. Wang, "Molecular beam epitaxial growth of InGaAsN:Sb/GaAs quantum wells for long-wavelength semiconductor lasers," *Applied Physics Letters*, vol. 75, no. 2, 1999, pp. 178–180.

[123] H. B. Yuen, S. R. Bank, H. Bae, M. A. Wistey, and J. S. Harris, "The role of antimony on properties of widely varying GaInNAsSb compositions," *Journal of Applied Physics*, vol. 99, no. 9, 2006, pp. 1–8.